Growth and Studies of II-VI Binary and Ternary Compounds: Nanostructures and Thin Films

A thesis submitted
By

LALHRIATZUALA

In partial fulfillment of the requirement for the award of the degree of
Doctor of Philosophy

Department of Physics
Indian Institute of Technology Guwahati
Guwahati - 781039, Assam, India

December 2015

DECLARATION

The work contained in this thesis entitled "**Growth and Studies of II-VI Binary and Ternary Compounds: Nanostructures and Thin Films**" has been carried out by me under the supervision of Dr. Pratima Agarwal, Professor, Department of Physics, Indian Institute of Technology Guwahati, Guwahati, Assam, India. This thesis does not contain any material previously submitted for the award of any degree or diploma.

Date:

Lalhriatzuala
Department of Physics
Indian Institute of Technology Guwahati
Guwahati-781039, Assam, India


भारतीय प्रौद्योगिकी संस्थान गुवाहाटी
Indian Institute of Technology Guwahati

भारतीय प्रौद्योगिकी संस्थान गुवाहाटी
Indian Institute of Technology Guwahati
North Guwahati, Guwahati
PIN- 781 039, Assam State, INDIA
Phone: +91 361 2583000 Extn 2702, 2582702
Fax: +91 361 2690 762 (Institute), 2582749 (Department)

Dr. Pratima Agarwal
Professor
Department of Physics
E-mail:pratima@iitg.ernet.in

Dated: Dec 03, 2015

CERTIFICATE

This is certified that the work contained in this thesis entitled **“Growth and Studies of II-VI Binary and Ternary Compounds: Nanostructures and thin films”** submitted by Mr. Lalhriatzuala, a Ph.D. student in the Department of Physics, Indian Institute of Technology Guwahati, Guwahati, Assam, India, for the award of the degree of Doctor of Philosophy, has been carried out under my supervision. This work has not been submitted elsewhere for the award of any degree or diploma.

(Dr. Pratima Agarwal)

Dedicated

to

My Parents

"My son, hear the instruction of thy father, and forsake not the law of thy mother" – Proverbs 1:8

Acknowledgements

I would first like to thank God for His blessings and for enabling me to persevere through what I perceived, at times, to be impossible. I must also express my deepest gratitude to my thesis supervisor, Prof. Pratima Agarwal, for her continued support and guidance throughout my Ph. D. study. She taught me a lot on how to approach research problems, how to analyse and understand the results from a physicist's perspective. I am very thankful to her for giving me opportunity to work under her supervision and will remain ever grateful to her.

I am grateful to my doctoral committee members, Prof. A. Srinivasan (Chairman), Prof. P. S. Robi and Dr. D. Pamu for reviewing my research work regularly and for sharing their advice to enrich my research and dissertation. I extend my sincere gratitude to Prof. P. Poulose, department head, all the faculty members and staff of Physics Department for their support. I am also thankful to Mr. Chandan Borgohain, Dr. K. Senapati, Mr. M. Borah and Mr. K. Singh from Central Instrument Facility, IIT Guwahati for their help in using CIF facilities.

I am thankful to Vice Chancellor, Mizoram University and Principal, Pachhunga University College, Aizawl for allowing me to take study leave and enabling me to pursue the Ph. D. work. I owe a lot to all my colleagues in the Physics Department, Pachhunga University College for all the support and encouragements to complete my thesis work.

I am sincerely thankful to all my lab mates, Dr. Anto Pradeep, Dr. Himanshu S. Jha, Mr. Mukesh Singh, Mr. Ramakrisha Madaka, Ms. Asha Yadav, Mr. Venkanna Kanneboina, Mr. Suman Sarkar, Mr. Pilik Basumatary and Ms. Sukanya Buragohain for their company and help throughout my thesis work. I am thankful for having met colleagues and friends in the department and outside. Many friends have helped me throughout the work. Their support and encouragement helped me overcome setbacks. I greatly value their friendship and I deeply appreciate them.

I am fortunate to have wonderful friends, who have been constant encouragement throughout my thesis work. I thank my brothers and sister, and all my friends for their never-ending prayers, love and support.

My parents' love and many sacrifices afforded me this opportunity. I have no words to acknowledge them. Thank you...

Lalhriatzuala
IIT Guwahati, India, December 2015

Preface

II-VI compound semiconductors have been the subject of extensive research both in fundamental studies and for potential applications in devices. The broad range of band gaps and lattice constants available from these materials, and the unique fundamental phenomena they exhibit, make them attractive for a wide range of applications such as infrared lasers and detectors, blue green lasers and light emitting diodes (LEDs), nonlinear optical materials, magneto-optical devices, radiation detectors, photovoltaic devices, etc.

CdSe and ZnSe are among II-VI compounds, which are of interest to scientific researchers over the past several decades due to their promising properties for potential applications in thin film solar cells, optical coatings, light emitting diodes, sensors, etc. These compounds have properties such as (a) direct band gap ($CdSe \sim 1.68\,eV$ and $ZnSe \sim 2.7\,eV$ at room temperature), (b) high absorption coefficient, and (c) high thermal stability, which are suitable for most optoelectronic applications. In addition, they can be easily synthesized in the form of nanostructures and thin films using most of the low cost preparation techniques available today. Both CdSe and ZnSe nanostructures have an interior structure and bonding identical to that of their respective bulk materials. However, in nanocrystals, the reduced dimensions result in an increase in specific surface area and bandgap widening due to quantum confinement effect. Because of these, nanomaterials not only have enhanced photosensitivity but also open the door for material engineers to alter the properties of these materials by controlling the dimensions of the nanomaterials. These properties that come with nanodimensional effect make these compounds attractive candidate for various optoelectronic applications with possibly enhanced efficiency in comparision to their bulk counterparts.

Another interesting feature of II-VI compounds is the ease to form ternary and quaternary alloys, which offers huge advantage due to the fact that the structural, optical and electrical properties are easily altered with compositional changes. A number of devices based on applications of II-VI ternary alloy semiconductors are currently in use. Among II-VI ternary alloy semiconductors, ZnS_xSe_{1-x} and CdS_xSe_{1-x} are the prime attention of current researchers mostly due to their ideal tunable range of bandgap in the visible spectrum and the dual phonon mode properties. By controlling their composition optical bandgap of ZnS_xSe_{1-x} and CdS_xSe_{1-x} compounds can be tuned between ~ 2.7 - 3.68 eV and ~ 1.68 - 2.42 eV respectively. The compositional change is also accompanied by corresponding changes in structural properties, which is also essential in material designing to achieve most suitable material for heterojunction devices.

ZnS_xSe_{1-x} and CdS_xSe_{1-x} are among few mixed crystal systems exhibiting two-mode behavior of the phonons. In these alloys, vibrational characteristic of both end binary compounds appear in the first order Raman spectra. Theoretical calculations have also shown that these compounds would have interesting phonon vibrations such as local mode and gap mode when the composition of either one of the anion is reduced to a small fraction.

Spin orbit (SO) coupling is a very important phenomenon, which affect the band structure in some of the II-VI compound semiconductors. This effect splits the valence band at the zone center into Γ_7^v and Γ_8^v resulting in two direct optical transitions ($\Gamma_8^v \rightarrow \Gamma_6^c$) and ($\Gamma_7^v \rightarrow \Gamma_6^c$) between valence and conduction bands. The extent of this splitting depends on the size of the anion constituting the compounds. Since, ZnS_xSe_{1-x} and CdS_xSe_{1-x} consist of sulfur (small size anion) and selenium (larger anion); the alloys are expected to exhibit SO splitting of the valence band depending on the composition.

In this thesis work, we prepare CdSe and ZnSe nanostructures by solvothermal process. Ternary alloy thin films, CdS_xSe_{1-x} and ZnS_xSe_{1-x} are prepared by thermal evaporation of solvothermally synthesized composite powders, viz., CdS-CdSe and ZnS-ZnSe. These samples are characterized by using X-ray diffraction (XRD), transmission electron microscopy (TEM), scanning electron microscopy (SEM), field emission scanning electron microscopy (FESEM) and energy dispersive X-ray analysis (EDAX). Thermal stability study of these materials is carried out by performing thermogravimetric analysis (TGA) measurement. Optical properties are investigated using UV-Vis-NIR spectroscopy and photoluminescence spectroscopy. Phonon modes in the materials are studied using room temperature Raman spectroscopy.

The thesis is organized into six chapters. Chapter 1, which is the introduction, gives the overall perspective of both the binary compound (CdSe and ZnSe) nanocrystals and ternary alloy (CdS_xSe_{1-x} and ZnS_xSe_{1-x}) films material properties, growth technique, applications in devices, the motivation of the present work and an outline of the work contained in the present thesis. Chapter 2 gives a description of the details of sample preparation and different characterization techniques used for analysis of structural, optical and thermal properties of the materials in the present work. Chapter 3 contains studies on the structural, optical and thermal properties of CdSe and ZnSe nanocrystals. In this chapter, evolution of structural and morphology with solvothermal reaction time and the corresponding changes in the physical properties are discussed. Chapter 4 presents systematic studies on the growth, the structural and optical properties of CdS_xSe_{1-x} ternary alloy thin films deposited by thermal evaporation of solvothermally synthesized CdS-CdSe composite powders. Chapter 5 also presents similar studies on ZnS_xSe_{1-x} ternary alloy thin films prepared by the same deposition process as in Chapter 4. Finally, Chapter 6 summarizes the results and presents the future scope of the work.

LIST OF ABBREVIATIONS AND SYMBOLS

NC	Nanocrystal
CdS	Cadmium Sulfide
ZnS	Zinc Sulfide
CdSe	Cadmium Selenide
ZnSe	Zinc Selenide
CdS_xSe_{1-x}	Cadmium Sulpho-Selenide
ZnS_xSe_{1-x}	Zinc Sulpho-Selenide
XRD	X-ray diffraction
SEM	Scanning Electron Microscopy
EDAX	Energy Dispersive X-ray Spectroscopy
FESEM	Field Emission Scanning Electron Microscopy
TEM	Transmission Electron Microscopy
HRTEM	High Resolution Transmission Electron Microscopy
IFFT	Inverse Fast Fourier Transform
UV-Vis-NIR	Ultraviolet-visible-near infrared
PL	Photoluminescence
TGA	Thermogravimetric Analysis
DTA	Differential Thermal Analysis
DTG	Derivative Thermogravimetry
LED	Light Emitting Diode
FWHM	Full width at half maximum
SO	Spin orbit
TO	Transverse optic
LO	Longitudinal optic
LA	Longitudinal Acoustic
TA	Transverse Acoustic
ZE	Zone Edge

SP	Surface Phonon
a.u.	arbitrary unit
E_g	Bandgap
h	Planck’s constant
θ	Bragg’s angle
α	Absorption Coefficient
ε	Strain
μ	Micron
Å	Angstrom
D	Average Crystallite Size
k	Boltzmann constant
β	FWHM
λ	Wavelength
CuK_α	Copper K_α radiation
P_e	Equilibrium Vapour Pressure
δ	Dislocation Density
E_a	Activation Energy
$h\nu$	Photon Energy
ε_0	Static dielectric constant
ε_∞	High frequency dielectric constant
K	Kelvin
^oC	Degree Celsius
T	Temperature
eV	Electron Volt

CONTENTS

LIST OF FIGURES

LIST OF TABLES

Chapter 1

Introduction

II-VI semiconductors are in the forefront of materials being studied for their potential applications in blue and green light emitting devices (LEDs), solar cells, optical coatings, etc. These semiconductors are formed by the combination of IIB metal (e.g., Zn, Cd, or Hg, in periods 3, 4, and 5 respectively) with a group VIA cation (usually O, S, Se and Te). These materials exhibit various electrical and optical properties similar to the commonly known group IV elemental semiconductors. The electrical conductivity of these materials lies between metal conductors and dielectrics as in the case of their counterparts in group IV elements of the periodic table. However, due to possibilities of forming large number of different compounds, the band gap and other properties of these materials can be extended over a wide range [1]. While some of the compounds are having a very narrow band gap and behaving almost like metals, other materials with wide bandgap are having properties close to dielectrics. Since many optoelectronic devices are now mostly designed using thin film technology, II-VI compound thin films have also been developed with the help of various preparation processes such as atomic layer epitaxy [2, 3], metalorganic chemical vapour deposition (CVD) [4, 5], plasma enhanced CVD [6], rf magnetron sputtering [7], pulse laser deposition [8], chemical spray [9], etc., with properties that are dependent on the preparation conditions. Nowadays, researchers are also exploring nanoparticle based devices of these compounds, which for certain applications are giving better performance. By designing the size and shape through various nanoparticle synthesis processes, properties of II-VI nanostructure compounds are engineered to optimize device performances and to enhance its viability in many optoelectronic applications [10, 11]. Another interesting feature of II-VI compounds is the ease to form ternary and quaternary alloys, which offers huge advantage due to the fact that the structural, optical and electrical properties are easily altered with compositional changes [12-16]. In this introductory chapter, we will discuss the material properties, potential applications, methods of preparation of some of the II-VI binary and ternary semiconductors, which are investigated in the present work. The chapter will be concluded with motivations behind the present work and the outline of the thesis.

1.1 II-VI binary compound semiconductors: CdSe and ZnSe

1.1.1 Structure of CdSe and ZnSe binary compounds

In these compounds each atom of a given element is surrounded tetrahedrally by four atoms of the other constituent element. The bonds in these compounds much resemble those of the Group IV elements, where the atoms undergo sp3 hybridization resulting in equivalent four covalent bonding between each atom and its four neighbouring atoms. The atoms also undergo sp3 hybridization but the difference in the electronegativities of the participating atoms from different groups in the periodic table causes the actual bond type to differ from pure covalent bonding. In these semiconductors, the “charge clouds” of the covalent bonds is distorted from true covalent symmetry to give a greater mean electron density in the neighbourhood of the more electronegative atoms. Because of this, the bonds in these compounds lie between ionic and covalent type. Here, the ionic character has the effect of binding the valence electrons rather tightly to the lattice atoms, which results in larger bandgap than those of the covalent semiconductors of comparable atomic weights.

As a consequence of the sp3 hybridization, CdSe and ZnSe crystallize in such a manner that each atom of one element is located at the center of a regular tetrahedron, the apices of which are occupied by atoms of other elements. Two possible structures can be formed from such tetrahedron.

(i) The sphalerite or zinc blende (cubic) type

The sphalerite structure as shown in figure 1.1 (a) is made up of two interpenetrating FCC sublattice, in which the sublattice are made up of each of the two individual atom types. If the red spheres in figure 1.1(a) are atoms of Group VI element, the green spheres will be atoms of the corresponding Group II element. The space group is $F\bar{4}3m(T_d\ )$. The coordination is 4 for atoms of both elements

(ii) The wurtzite (hexagonal) type

Similar to zinc blende structure, wurtzite structure shown in figure 1.1 (b) is made up of two HCP sublattices, in which each of the two individual atom types forms the sublattice. Its space group is $P6_3mc$ (C_{6v}^4). The coordination number in this case is also 4 for atoms of both elements.

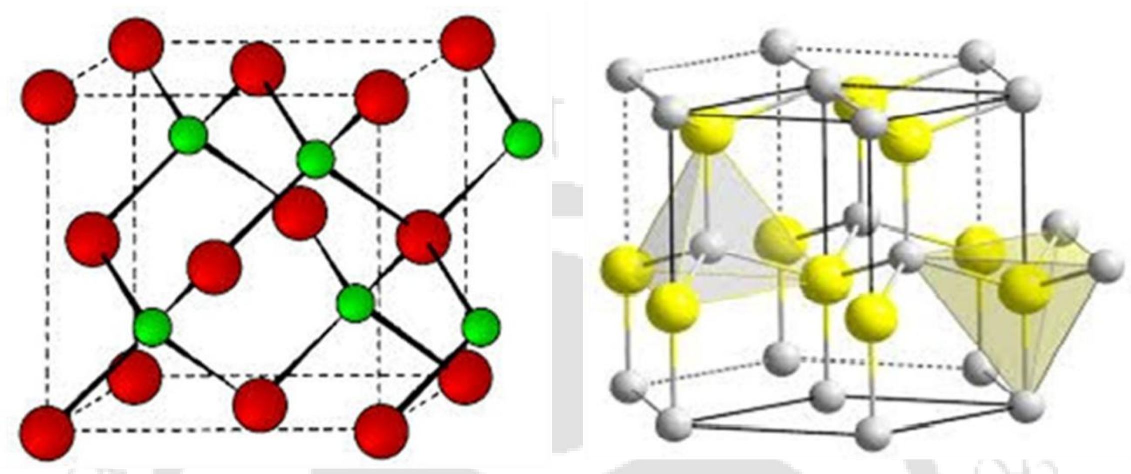

(a) (b)

Figure 1.1: (a) Zinc blende structure showing two interpenetrating FCC lattice [17], (b) Wurtzite structure showing two interpenetrating HCP lattice.

Table 1.1: Structural parameters of CdSe and ZnSe binary compounds [1].

Compounds	Structure	Lattice parameter (Å)		Cation – anion distance (Å)	Phillips's ionicity f_i	Bohr radius (nm)
		a	c			
CdSe	Zinc blende	6.077		2.63	0.699	5.6
	Wurtzite	4.299	7.010	2.63	0.699	
ZnSe	Zinc blende	5.618		2.45	0.630	3.8
	Wurtzite	3.974	6.506	2.45		

Table 1.1 shows the structural parameters of both CdSe and ZnSe [1]. The values shown in the table are the reported values for bulk material of the compounds. The structural form and the parameters largely determine other properties as discussed in the next section.

1.1.2 Properties of CdSe and ZnSe binary compounds

CdSe and ZnSe are among II-VI wide band gap semiconductors, which possess intrinsic n-type conductivity [18-20]. Table 1.2 shows some of the reported semiconducting properties of the two binary compounds investigated in this thesis work. The values given in the table corresponds to the properties of bulk substance of these compounds. Most optical properties of semiconductors are related to the nature of their electronic band structures. Their electronic band structures are in turn related to the type of crystallographic structure, the particular atoms, and their bonding. In II-VI compounds, the outermost s orbitals from the group II element and p orbitals from the group VI element are understood to form the bottom of the conduction band and upper valence bands states respectively [21, 22]. The upper valence band states are constructed out of appropriate linear combinations of products of p_x, p_y, p_z hydrogen like orbitals with spin functions. In the absence of both spin-orbit and crystalline field effects, these states are degenerate. The crystalline field partially removes this degeneracy, separating p_z from the p_x and p_y orbitals. This then put p_z band below the p_x, p_y band in the valence band structure. Both in CdSe and ZnSe compounds and other selenide and telluride II-VI semiconductors [1, 22-24], p_x and p_y bands are further split by spin-orbit coupling as shown in figure 1.2. This property influences the optical properties of the resulting material.

Table 1.2: Semiconducting properties of bulk CdSe and ZnSe binary compounds [1, 25].

Compounds		Band gap (eV)	Mobility ($cm^2V^{-1}s^{-1}$)	Dielectric constant $\varepsilon_o/\varepsilon_\infty$	Refracti-ve index	SO splitoff energy (eV)
CdSe (n-type)	Zinc blende	1.68	650	9.6/6.2		0.41
	Wurtzite	1.75		9.5/6.2	2.5	0.41
ZnSe (n-type)	Zinc blende	2.67	200	9.2/5.8	2.5	0.42

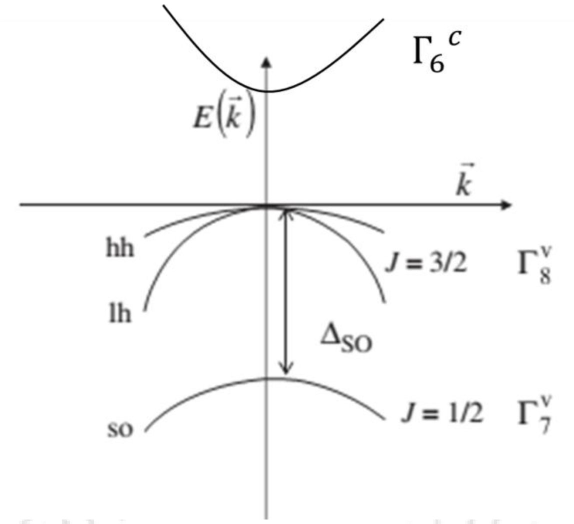

Figure 1.2: Representative figure of the band structure of II-VI compounds showing SO splitting in the valence band; hh – heavy hole band, lh – light hole band, SO – split off band, Δ_{SO}- spin orbit splitting energy.

The reported SO split off energy for bulk CdSe and ZnSe are given in the table, reported value in thin films, however, varies from 0.17 to 0.4 eV [1, 23]. Table 1.3 shows the melting point, elastic stiffness constants and zone center phonon modes of bulk CdSe and ZnSe compounds. These properties enable these two compounds to be suitable for many optoelectronic applications, where high thermal stability and rigidity is required.

Table 1.3: Thermal, elastic and vibrational properties of bulk CdSe and ZnSe binary compounds [1].

Compounds		Melting point (K)	Elastic stiffness constants (10^{11} dyne/cm^2)			Zone center phonon frequency (cm^{-1})	
			C_{11}	C_{12}	C_{44}	TO	LO
CdSe	Zinc blende	1512	6.67	4.63	2.23	169	211
	Wurtzite	1512	7.41	4.52	1.34	166 (A1), 172 (E1)	211 (A1), 210 (E1)
ZnSe	Zinc blende	1793	8.57	5.07	4.05	205	250

In nanostructured material, the reduced dimensions result in interesting size and morphology dependent physical properties. Some of the main features of the nanomaterial properties are summarized as follows.

(i) **Quantum confinement effect:** When dimension of a material is reduced to such an extent that it is comparable with the bulk exciton Bohr radius of the material, the following regime of quantum confinement occurs, which modifies the electronic band structure and raises the energy bandgap [26, 27].

(a) Weak confinement regime: The radius of a crystallite is greater than the bulk exciton Bohr radius. The dominant energy is the Coulomb term and exciton energy states are shifted to higher energies by confinement.

(b) Moderate confinement regime: This regime occurs when crystallite radius $R \approx a_B$, bulk exciton Bohr radius and $a_h < R < a_c$, where, a_h and a_c are the hole and electron Bohr radii, respectively.

(c) Strong confinement regime: In this regime, the size of a particle is less than a_B. In this region, the band structure is very sensitive to size of the particle and the bandgap value is significantly altered.

Due to the quantum confinement effect, the optical properties vis., absorbance, refractive index, photoluminescence, etc., of CdSe and ZnSe nanoparticles are significantly different from the bulk values given in table 1.2.

(ii) **Phonon confinement:** When dimension of a material is reduced, at certain point the $q = 0$ selection rule of infinite periodicity in the case of Raman scattering is no longer valid. As a result, the phonons away from the zone center also take part in the scattering. This confinement along with the increased strain in nanostructured materials, compressive and tensile strains, results in shifting and broadening of a Raman peak [28-30].

(iii) **Reduced thermal stability:** Thermal stability is another important aspect in material designing, when dealing with nanoparticles. Both CdSe and ZnSe in bulk form are known to have high thermal stability with a melting point of about 1512 and 1793 K respectively [1]. However, in nanomaterials, the reduced dimension results in increase in specific surface area, which causes an increase in the sample's heat absorption ability. This factor along with increase in dislocations, cracks, and other discontinuities in the crystal structure results in increase in the number of active sites on the surface favourable for nucleation (decomposition reaction) [31-33], which reduces thermal stability.

1.1.3 Applications of CdSe and ZnSe binary compounds

II-VI compounds were one of the earliest semiconductors used in industry. These were extensively used in cathode-ray tube displays [34]. Owing to their direct bandgap nature, these have high probability of radiative recombination of non-equilibrium carriers. This results in strong emission in the visible region due to their large bandgaps. On the other hand, carrier mobilities are small and so are the diffusion lengths of minority carriers, typically 0.1 μm for holes and 0.5 μm for electrons [34]. Nevertheless, they have been found useful in photodetectors [35-41], solar cells [42-46], light emitting devices [47-50], sensors [51-53], etc. CdSe with a bandgap that divides the solar spectrum into the thermal part with radiation energy less than the bandgap and the optical part with radiation energy larger than the bandgap also finds applications in solar coatings [54].

1.1.4 Methods of preparation of CdSe and ZnSe nanostructure

Preparation and characterization of II-VI nanoscale semiconductor compounds have attracted much attention from as early as the later part of 1980s. First attempt to synthesize the ZnSe quantum dots was made in 1986 by Chestnoy et al. [55]. They obtained ZnSe quantum dots with zinc blende structure, which were stable only at cryogenic temperatures. CdSe nanocrystals on the other hand were first reported by M. L. Steigerwald and his co-workers at AT& T Bell laboratories in 1987 [56], in which they developed the method using organometallic reagents in inverse micellar solution and chemical modification of the surface. The early reports on nanocrystals of these compounds have lots of issues related to the high toxicity of the precursors, stability at room temperature, etc. Later, through the development of chemical routes and other techniques these issues were addressed. At present, researchers focus mainly on control of dimension and morphology of these nanocrystals and the corresponding properties by adjusting the synthesis parameters. Among various nanoparticle synthesis routes that are now widely used today, solvothermal method has been proven to be the most convenient route to fabricate CdSe and ZnSe nanostructures due to easy control of phase, size and morphology [57]. In the solvothermal process, various solvents such as a mixture of de-ionzed water and chemical solutions such as diethylamine [58], ethylendiamine [59], triethylenetetramine (TETA) [60], ammonia solution [61], oleic acid [62], etc., are used.

By adjusting composition of the mixed solution, CdSe and ZnSe nanostructures such as microspheres [57], nanorods [61], hollow nanospheres [62], nanoneedles [63], nanoflowers [64], etc., are now being synthesized using solvothermal method.

1.2 II-VI ternary alloy semiconductors: CdS_xSe_{1-x} and ZnS_xSe_{1-x}

ZnS_xSe_{1-x} and CdS_xSe_{1-x} are one of the most technologically relevant II-VI ternary alloy semiconductors due to the possibility of controlling structural, optical and electrical properties over a wide range. By controlling the fraction of sulfur (x) in the alloy, properties of these compounds can be tuned between the respective properties of the two end binary compounds. In the case of ZnS_xSe_{1-x}, the end binary compounds ZnSe and ZnS possess wide direct bandgap of 2.67 and 3.68eV respectively, which are suitable for many optoelectronic applications including solar cell [42, 46, 65, 66], blue-green laser diodes [67-69], photodetectors [39, 41, 70], etc. It is possible to design new ternary alloy materials by alloying ZnSe and ZnS with desired composition that can have optical bandgap between 2.67 and 3.68 eV. Similarly, by controlling CdS_xSe_{1-x} compositions one can also design new materials having bandgap between 1.68 and 2.42 eV (bulk bandgap values of CdSe and CdS respectively) [25]. In designing heterojunction devices, lattice matching between the layers is essential for optimum performance of the device. This can also be achieved in the alloying process by tuning the structural property with compositional variation.

Spin orbit (SO) coupling is a very important phenomenon, which affect the band structure in some of the II-VI compound semiconductors. This effect splits the valence band at the zone center into Γ_7^v and Γ_8^v resulting in two direct optical transitions ($\Gamma_8^v \rightarrow \Gamma_6^c$) and ($\Gamma_7^v \rightarrow \Gamma_6^c$) between valence and conduction bands. The extent of this splitting depends on the size of the anion constituting the compounds [71, 72]. As given in table 1.2, the selenide compounds have significantly large SO split-off energy of about 0.4 eV. Sulfide and oxide compounds of cadmium and zinc, on the other hand, do not show observable SO split-off energy [1]. Since, ZnS_xSe_{1-x} and CdS_xSe_{1-x} consist of sulfur (small size anion) and selenium (larger anion); the alloys are expected to exhibit SO splitting of the valence band, which could be reflected in the transmission spectra. The extent of the splitting is also expected to vary with compositional variation.

Another interesting feature of these ternary compounds is the two-mode behavior of the phonons, where vibrational characteristic of both end binary compounds appear in the first order Raman spectra. Theoretical calculations have also shown that these compounds would have interesting phonon vibrations such as local mode and gap mode when the composition of either one of the anion is reduced to a small fraction [73].

Preparation of ternary alloy ZnS_xSe_{1-x} was first reported by Larachet et. al. [74], in 1957 where they used the method of dry ball milling of phosphor-grade zinc chalcogenides (zinc sulphide and zinc selenide) and subsequent crystallization by heating. Results on measurements of diffuse reflection as a function of wavelength showed a linear relationship between energy band gap and composition without any bowing. Cutter et al. [75], in 1967 reported the first successful vapour phase growth of homogeneous ZnS_xSe_{1-x} ternary alloy. The resulting alloy, however, has mixed phase with random stacking faults for larger fraction of sulfur. The vapour phase growth of CdS_xSe_{1-x} was first reported in 1965 by S. Asano and N. Yamashita [76]. The prepared films had nearly constant hexagonality of about 80 % and the band gap was observed to decrease with CdSe proportion. With the advancement in thin film technology, a number of preparation routes involving vapour phase as well as liquid phase growth, which results in uniform thin films with homogeneous composition and crystal phase, have been reported over the past two decades. Investigations on the properties of these ternary alloys prepared using laser ablation [12], chemical bath deposition [13], pyrolitic spray deposition [15], close-spaced sublimation [77], metal organic vapour phase epitaxy (MOVPE) [14], etc., have all shown good tunable structural and optical properties. Most of the results reported in recent papers show the composition dependent band gap with bowing parameter of 0.45 to 0.68 eV for ZnS_xSe_{1-x} and of about 0.54 eV for CdS_xSe_{1-x} [25].

1.3 Motivations

As discussed in the previous sections, the II-VI binary compounds and ternary alloys possess interesting physical properties that are suitable for applications in various optoelectronic devices. These properties invite the interest of scientific community to investigate these materials for applied sciences as well as for contributing basic scientific knowledge in the subject that concerns with the material property. However, from thorough literature survey on the nanostructured binary ZnSe and CdSe compounds, and ternary ZnS_xSe_{1-x} and CdS_xSe_{1-x} alloys, the following points were observed which motivated the present work.

1) Although there are some published research papers dealing with CdSe and ZnSe nanoparticle synthesis, there are very few reports that deal with the study of the influence of reaction time on the nanocrystals. In any solvothermal reaction leading to nanoparticle synthesis, it is important to understand how the properties of the nanocrystals evolve with reaction time.
2) Thermal stability is another important property, which needs to be addressed in designing nanoparticle based optoelectronic devices. It will be interesting to find out the thermal stability of the nanocrystals synthesized for different reaction time and also to understand the kinetics of the thermal decomposition. To our knowledge there are no reports on the study of thermal decomposition kinetics of CdSe and ZnSe nanocrystals.
3) ZnS_xSe_{1-x} and CdS_xSe_{1-x} ternary alloy thin films are understood to show composition dependent properties. There are some reports on the preparation and study of these films implemented using various deposition techniques mentioned in the previous section. However, to our knowledge, there is no systematic investigation into the optical properties in order to understand the SO coupling effect in these ternary systems.
4) Dual phonon mode behaviour in CdS_xSe_{1-x} and ZnS_xSe_{1-x} alloys is one of the most interesting features of these alloys. Investigation on the phonon modes behaviour would add further understanding of these alloys.

In view of the above mentioned points, the following objectives and work plans were proposed for the thesis.

1) To synthesis CdSe and ZnSe nanomaterials using solvothermal method for different reaction time.
2) To investigate the structural and optical properties and thermal stability of the synthesized materials using various characterization techniques.
3) To synthesis ZnS-ZnSe and CdS-CdSe composite powders by using solvothermal technique and to deposit ZnS_xSe_{1-x} and CdS_xSe_{1-x} thin films using thermal evaporation of the composite powders.

4) To investigate the changes in structural and optical properties of the ternary alloy films with compositional changes.
5) To study the dual phonon mode and SO splitting effect in these alloys and understand the interesting physics.

1.4 Contents of thesis chapters

The present thesis consists of six (06) chapters. Chapter 1 is the Introduction chapter. Following this introductory chapter is Chapter 2, which gives a description of the details of sample preparation and different characterization techniques used for analysis of structural, optical and thermal properties of the materials in the present work.

Chapter 3 contains studies on the structural, optical and thermal properties of CdSe and ZnSe nanocrystals. In this chapter, evolution of structural and morphology with solvothermal reaction time and the corresponding changes in the physical properties are discussed. Thermal stability studies to understand the kinetics of thermal decomposition are also presented in this chapter.

Chapter 4 presents systematic studies on the growth, structural and optical properties of CdS_xSe_{1-x} ternary alloy thin films as deposited by thermal evaporation of solvothermally synthesized CdS-CdSe composite powders. Studies on dependence of SO splitting energy and dual phonon mode vibration on the composition of the alloys are also presented.

Chapter 5 presents systematic studies on the growth, structural and optical properties of ZnS_xSe_{1-x} ternary alloy thin films as deposited by thermal evaporation of solvothermally synthesized ZnS-ZnSe composite powders. This chapter also contains studies on SO splitting energy and dual phonon mode behavior of the ternary alloys.

Chapter 6 is the final chapter of the thesis, which summarizes the contents of each chapter and gives the final conclusion based on the work reported in this thesis. The thesis work is concluded with the scope for future work from the present investigation.

1.5 References

[1] S. Adachi, Handbook on Physical Properties of Semiconductors, Kluwer Academic Publishers, New York, 2004.

[2] C.T. Hsu, Epitaxial growth of II-VI compound semiconductors by atomic layer epitaxy, Thin Solid Films, 335 (1998) 284-291.

[3] H. Sitter, W. Faschinger, Atomic-Layer Epitaxy of II-VI Compound Semiconductors, Festkor-Adv Solid St, 30 (1990) 219-237.

[4] B. Cockayne, P.J. Wright, Metalorganic Chemical Vapor-Deposition of Wide Band-Gap II-VI Compounds, Journal of Crystal Growth, 68 (1984) 223-230.

[5] P.J. Wright, B. Cockayne, The organometallic chemical vapour deposition of ZnS and ZnSe at atmospheric pressure, Journal of Crystal Growth, 59 (1982) 148-154.

[6] B.S. Li, Y.C. Liu, D.Z. Shen, J.Y. Zhang, Y.M. Lu, X.W. Fan, Effects of RF power on properties of ZnO thin films grown on Si (0 0 1) substrate by plasma enhanced chemical vapor deposition, Journal of Crystal Growth, 249 (2003) 179-185.

[7] P.F. Yang, H.C. Wen, S.R. Jian, Y.S. Lai, S. Wu, R.S. Chen, Characteristics of ZnO thin films prepared by radio frequency magnetron sputtering, Microelectronics Reliability, 48 (2008) 389-394.

[8] B. Kotlyarchuk, V. Savchuk, M. Oszwaldowski, Preparation of undoped and indium doped ZnO thin films by pulsed laser deposition method, Cryst Res Technol, 40 (2005) 1118-1123.

[9] M.L. Olvera, A. Maldonado, R. Asomoza, S. Tirado-Guerra, Characteristics of transparent and conductive undoped ZnO thin films obtained by chemical spray using zinc pentanedionate, Thin Solid Films, 411 (2002) 198-202.

[10] Y. Duan, S. Yao, C. Dai, X. Liu, G. Xu, Characterization of ZnSe microspheres synthesized under different hydrothermal conditions, Transactions of Nonferrous Metals Society of China, 24 (2014) 2588-2597.

[11] G.S. Paul, P. Agarwal, Evolution of nanostructure with reaction time for ZnS synthesized by solvothermal process, Physica Status Solidi (c), 7 (2010) 909-912.

[12] S. Pagliara, L. Sangaletti, L.E. Depero, V. Capozzi, G. Perna, Effect of disorder on the Raman scattering of CdS_xSe_{1-x} films deposited by laser ablation, Solid State Communications, 116 (2000) 115-119.

[13] R.S. Mane, C.D. Lokhande, Studies on chemically deposited cadmium sulphoselenide (CdSSe) films, Thin Solid Films, 304 (1997) 56-60.

[14] A.L. Gurskii, E.V. Lutsenko, G.P. Yablonskii, V.I. Kozlovsky, A.B. Krysa, J. Söllner, M. Scholl, H. Hamadeh, M. Heuken, Photo- and cathodoluminescence of ZnSSe quantum well heterostructures grown by MOVPE, Journal of Crystal Growth, 159 (1996) 518-522.

[15] K.T.R. Reddy, Y.V. Subbaiah, T.B.S. Reddy, D.B. Johnston, I. Forbes, R.W. Miles, Pyrolytic spray deposition of ZnS_xSe_{1-x} layers for photovoltaic applications, Thin Solid Films, 431 (2003) 340-343.

[16] R. Rujkorakarn, A.J. Nelson, Optical properties of $ZnS_{1-x}Se_x$ alloys fabricated by plasma-induced isoelectronic substitution, Journal of Applied Physics, 87 (2000) 8557-8560.

[17] A.R. Barron, C. Smith, Crystal Structure, in, OpenStax-CNX, 2010, pp. 12.

[18] D. Kurbatov, V. Kosyak, A. Opanasyuk, V. Melnik, Native point defects in ZnS films, Physica B: Condensed Matter, 404 (2009) 5002-5005.

[19] A. Garcia, J.E. Northrup, Compensation of P-Type Doping in Znse - the Role of Impurity-Native Defect Complexes, Phys Rev Lett, 74 (1995) 1131-1134.

[20] D.B. Laks, C.G. Van De Walle, G.F. Neumark, S.T. Pantelides, Role of Native Defects in Wide-Band-Gap Semiconductors, Phys Rev Lett, 66 (1991) 648-651.

[21] F.L. Pedrotti, D.C. Reynolds, Spin-Orbit Splitting in CdS: Se Single Crystals, Physical Review, 127 (1962) 1584-1586.

[22] B. Pejova, The higher excited electronic states and spin-orbit splitting of the valence band in three-dimensional assemblies of close-packed ZnSe and CdSe quantum dots in thin film form, J Solid State Chem, 181 (2008) 1961-1969.

[23] S. Velumani, X. Mathew, P.J. Sebastian, S.K. Narayandass, D. Mangalaraj, Structural and optical properties of hot wall deposited CdSe thin films, Solar Energy Materials and Solar Cells, 76 (2003) 347-358.

[24] U. Pal, D. Samanta, S. Ghorai, A.K. Chaudhuri, Optical constants of vacuum-evaporated polycrystalline cadmium selenide thin films, Journal of Applied Physics, 74 (1993) 6368-6374.

[25] M.O. Manasreh, Optoelectronic Properties of Semiconductors and Superlattices, Taylor & Francis Inc., New York, 2002.

[26] S. Suresh, Semiconductor Nanomaterials, Methods and Applications: A Review, Nanoscience and Nanotechnology, 3 (2013) 62-74.

[27] E.O. Chukwuocha, M.C. Onyeaju, T.S.T. Harry, Theoretical Studies on the Effect of Confinement on Quantum Dots Using the Brus Equation, World Journal of Condensed Matter Physics, 2 (2012) 96-100.

[28] H.Z. An, Q. Zhao, W.M. Du, Raman spectra of ZnSe nanoparticles synthesized by thermal evaporation method, Chinese Physics, 13 (2004) 1753-1757.

[29] A. Tanaka, S. Onari, T. Arai, One phonon Raman scattering of CdS microcrystals embedded in a germanium dioxide glass matrix, Journal of the Physical Society of Japan, 61 (1992) 4222-4228.

[30] I.H. Campbell, P.M. Fauchet, The effects of microcrystal size and shape on the one phonon Raman spectra of crystalline semiconductors, Solid State Communications, 58 (1986) 739-741.

[31] M. Fathollahi, S.M. Pourmortazavi, S.G. Hosseini, Particle Size Effects on Thermal Decomposition of Energetic Material, Journal of Energetic Materials, 26 (2007) 52-69.

[32] R. Liu, T. Zhang, L. Yang, Z. Zhou, Effect of particle size on thermal decomposition of alkali metal picrates, Thermochimica Acta, 583 (2014) 78-85.

[33] M.R. Sovizi, S.S. Hajimirsadeghi, B. Naderizadeh, Effect of particle size on thermal decomposition of nitrocellulose, Journal of Hazardous Materials, 168 (2009) 1134-1139.

[34] S. Bhunia, D.N. Bose, Crystal Growth and Applications of II-VI Compounds, PINSA-A, 64 (1997) 211 - 223.

[35] D.C. Oertel, M.G. Bawendi, A.C. Arango, V. Bulovic, Photodetectors based on treated CdSe quantum-dot films, Applied Physics Letters, 87 (2005) 213505

[36] X. Wang, W. Song, B. Liu, G. Chen, D. Chen, C. Zhou, G. Shen, High-Performance Organic-Inorganic Hybrid Photodetectors Based on P3HT:CdSe Nanowire Heterojunctions on Rigid and Flexible Substrates, Adv Funct Mater, 23 (2013) 1202-1209.

[37] Y. Jiang, W.J. Zhang, J.S. Jie, X.M. Meng, X. Fan, S.T. Lee, Photoresponse properties of CdSe single-nanoribbon photodetectors, Adv Funct Mater, 17 (2007) 1795-1800.

[38] A.I. Nusir, J. Aguilar, Z. Bever, M.O. Manasreh, Uncooled photodetectors based on CdSe nanocrystals with an interdigital metallization, Applied Physics Letters, 104 (2014) 051124.

[39] S. Li, Q. Su, H. Zhao, Photoresponse properties of p-type ZnSe nanowire photodetectors, Micro and Nano Letters, 8 (2013) 496-499.

[40] T.K. Lin, S.J. Chang, Y.K. Su, Y.Z. Chiou, C.K. Wang, C.M. Chang, B.R. Huang, ZnSe homoepitaxial MSM photodetectors with transparent ITO contact electrodes, Ieee T Electron Dev, 52 (2005) 121-123.

[41] F. Vigue, E. Tournie, J.P. Faurie, ZnSe-based Schottky barrier photodetectors, Electron Lett, 36 (2000) 352-354.

[42] Z. Ning, H. Tian, C. Yuan, Y. Fu, H. Qin, L. Sun, H. Agren, Solar cells sensitized with type-II ZnSe-CdS core/shell colloidal quantum dots, Chemical Communications, 47 (2011) 1536-1538.

[43] J. Ni, Z. Wu, X. Lin, J. Zheng, S. Li, J. Li, J. Kang, Band engineering of type-II ZnO/ZnSe heterostructures for solar cell applications, J Mater Res, 27 (2012) 730-733.

[44] D. Cheng, H. Hao, M. Zhang, W. Shi, M. Lu, Improving Si solar cell performance using Mn:ZnSe quantum dot-doped PLMA thin film, Nanoscale Res Lett, 8 (2013) 291.

[45] S. Kim, J. Lee, W. Han, J. Lee, Electrochemical deposition of CdSe/CdTe multilayer nanorods for hybrid solar cell, Thin Solid Films, 518 (2010) 7222-7224.

[46] J. Xu, X. Yang, Q.D. Yang, T.L. Wong, S.T. Lee, W.J. Zhang, C.S. Lee, Arrays of CdSe sensitized ZnO/ZnSe nanocables for efficient solar cells with high open-circuit voltage, J Mater Chem, 22 (2012) 13374-13379.

[47] H.S. Chen, H. Cheng-Kuo, H.-Y. Hong, InGaN-CdSe-ZnSe quantum dots white LEDs, Ieee Photonic Tech L, 18 (2006) 193-195.

[48] W. Chung, H.J. Yu, S.H. Park, B.H. Chun, S.H. Kim, YAG and CdSe/ZnSe nanoparticles hybrid phosphor for white LED with high color rendering index, Materials Chemistry and Physics, 126 (2011) 162-166.

[49] K. Han, S. Yoon, W.J. Chung, CdS and CdSe Quantum Dot-Embedded Silicate Glasses for LED Color Converter, Int J Appl Glass Sci, 6 (2015) 103-108.

[50] S.W. Lee, J.S. Kim, J.S. Lee, H.M. Jeong, S.A. Gopalan, S.W. Kang, B.H. Kang, S.H. Lee, D.H. Kwon, Enhancement of CdSe/ZnS quantum dot-based LED by core-shell modification, J Korean Phys Soc, 66 (2015) 82-86.

[51] Y.O. Barmenkov, C. Sifuentes, A.N. Starodumov, CdS and CdSe semiconductor nanocrystal doped glasses and their application in fiber-optic sensors, Revista Mexicana De Fisica, 46 (2000) 64-66.

[52] D.D. Wu, Z. Chen, G.B. Huang, X.G. Liu, ZnSe quantum dots based fluorescence sensors for Cu^{2+} ions, Sensors and Actuators A: Physical, 205 (2014) 72-78.

[53] J. Capon, J. Debaets, I. Derycke, H. Desmet, J. Doutreloigne, A. Vancalster, J. Vanfleteren, CdSe-Based Thin-Film Integrated Optical Sensors, Sensors and Actuators A: Physical, 32 (1992) 437-441.

[54] P.J. Sebastian, V. Sivaramakrishnan, CdSe thin films as solar control coatings, Solar Energy Materials and Solar Cells, 27 (1992) 321-326.

[55] N. Chestnoy, R. Hull, L.E. Brus, Higher Excited Electronic States in Clusters of Znse, Cdse, and Zns - Spin-Orbit, Vibronic, and Relaxation Phenomena, J Chem Phys, 85 (1986) 2237-2242.

[56] M.L. Steigerwald, A.P. Alivisatos, J.M. Gibson, T.D. Harris, R. Kortan, A.J. Muller, A.M. Thayer, T.M. Duncan, D.C. Douglass, L.E. Brus, Surface Derivatization and Isolation of Semiconductor Cluster Molecules, J Am Chem Soc, 110 (1988) 3046-3050.

[57] J. Yang, C. Zang, G. Wang, G. Xu, X. Cheng, Synthesis of CdSe microspheres via solvothermal process in a mixed solution, Journal of Alloys and Compounds, 495 (2010) 158-161.

[58] H. Wang, Z. Guo, F. Du, Solvothermal synthesis of CdSe nanorods via DEA solution, Materials Chemistry and Physics, 98 (2006) 422-424.

[59] D. Xu, Z.P. Liu, J.B. Liang, Y.T. Qian, Solvothermal synthesis of CdS nanowires in a mixed solvent of ethylenediamine and dodecanethiol, J Phys Chem B, 109 (2005) 14344-14349.

[60] J. Yang, G. Wang, H. Liu, J. Park, X. Cheng, Controlled synthesis and characterization of ZnSe nanostructures via a solvothermal approach in a mixed solution, Materials Chemistry and Physics, 115 (2009) 204-208.

[61] G. Ramalingam, N. Melikechi, P.D. Christy, S. Selvakumar, P. Sagayaraj, Structural and optical property studies of CdSe crystalline nanorods synthesized by a solvothermal method, Journal of Crystal Growth, 311 (2009) 3138-3142.

[62] T. Wang, J. Wang, Y. Zhu, F. Xue, J. Cao, Y. Qian, Solvothermal synthesis and characterization of CdSe nanocrystals with controllable phase and morphology, Journal of Physics and Chemistry of Solids, 71 (2010) 940-945.

[63] J.H. Cheng, H.Y. Chao, Y.H. Chang, C.H. Hsu, C.L. Cheng, T.T. Chen, Y.F. Chen, M.W. Chu, Growth and characterization of CdSe nanoneedles and other one-dimensional CdSe nanostructures, Physica E: Low-dimensional Systems and Nanostructures, 40 (2008) 2000-2003.

[64] W.T. Yao, S.H. Yu, S.J. Liu, J.P. Chen, X.M. Liu, F.Q. Li, Architectural control syntheses of CdS and CdSe nanoflowers, branched nanowires, and nanotrees via a solvothermal approach in a mixed solution and their photocatalytic property, J Phys Chem B, 110 (2006) 11704-11710.

[65] S.M. Reda, S.A. El-Sherbieny, Dye-sensitized nanocrystalline CdS and ZnS solar cells with different organic dyes, J Mater Res, 25 (2010) 522-528.

[66] A. Goudarzi, G.M. Aval, R. Sahraei, H. Ahmadpoor, Ammonia-free chemical bath deposition of nanocrystalline ZnS thin film buffer layer for solar cells, Thin Solid Films, 516 (2008) 4953-4957.

[67] C. Boney, Z. Yu, W.H. Rowland, W.C. Hughes, J.W. Cook, J.F. Schetzina, G. Cantwell, W.C. Harsch, II-VI blue/green laser diodes on ZnSe substrates, J Vac Sci Technol B, 14 (1996) 2259-2262.

[68] D. Hommel, T. Behr, E. Kurtz, B. Jobst, K. Schull, A. Jakobs, J. Nurnberger, S. Einfeldt, M. Behringer, G. Landwehr, On the growth and doping of blue-green emitting ZnSe laser diodes, Journal of Crystal Growth, 159 (1996) 566-572.

[69] S. Itoh, S. Tomiya, R. Imoto, A. Ishibashi, Heterointerface control of ZnSe based II-VI laser diodes, Appl Surf Sci, 117 (1997) 719-724.

[70] L. Wang, M. Lu, P. Lv, J.S. Jie, T.X. Yan, Y.Q. Yu, C.Y. Wu, Y. Zhang, C. Xie, P. Jiang, Z. Wang, Z.Z. Hu, High-Performance Blue-Light Photodetectors Based on Single-Crystal ZnSe Nanoribbons with Controlled Gallium Doping, Sci Adv Mater, 4 (2012) 332-336.

[71] J.R. Chelikowsky, M.L. Cohen, Nonlocal pseudopotential calculations for the electronic structure of eleven diamond and zinc-blende semiconductors, Physical Review B, 14 (1976) 556-582.

[72] J.P. Walter, M.L. Cohen, Y. Petroff, M. Balkanski, Calculated and Measured Reflectivity of ZnTe and ZnSe, Physical Review B, 1 (1970) 2661-2667.

[73] I.F. Chang, S.S. Mitra, Application of a modified random-element-isodisplacement model to long-wavelength optic phonons of mixed crystals, Physical Review, 172 (1968) 924-933.

[74] S. Larach, R.E. Shrader, C.F. Stocker, Anomalous Variation of Band Gap with Composition in Zinc Sulfo- and Seleno-Tellurides, Physical Review, 108 (1957) 587-589.

[75] J.R. Cutter, G.J. Russell, J. Woods, Growth and Defect Structure of Single-Crystals of Zinc Selenide and Zinc Sulfo-Selenide, Journal of Crystal Growth, 32 (1976) 179-188.

[76] S. Asano, N. Yamashita, Photoconduction du Sulfo-Séléniure de Cadmium en Couche Evaporée, Japanese Journal of Applied Physics, 4 (1965) 839.

[77] S. Armstrong, P.K. Datta, R.W. Miles, Properties of zinc sulfur selenide deposited using a close-spaced sublimation method, Thin Solid Films, 403–404 (2002) 126-129.

Chapter 2

Experimental Details

In the course of the thesis work, several experimental techniques have been used for processing and characterizing the powder and thin film samples. This chapter describes the details of synthesis, preparation and characterization techniques used to study semiconductor nanocrystals and thin films.

2.1 Sample Preparations

2.1.1 Synthesis of nanostructured semiconductors

Nanotructured semiconducting materials are mostly prepared by various wet chemical routes like solvothermal [1-3], hydrothermal [4, 5], sonochemical method [6-9], reverse micelle process [10-12], sol-gel processing [13-15], etc. There are also physical processes like evaporation-condensation [16-19] and laser ablation [20-22] approaches. The nanoparticles prepared from these physical approaches have better uniformity in particle size and lower impurity in comparison to the wet chemical routes. However, these methods involve high vacuum and high temperature that require high cost bulky equipment. Because of this wet chemical routes are preferred as they are more cost effective. Among the wet chemical routes, solvothermal process is one of the most efficient in terms of size and morphology control of the nanoparticles. It is, therefore, chosen for synthesis of CdSe and ZnSe nanostructured binary compounds and CdS-CdSe and ZnS-ZnSe composite powders in this thesis work. Details of the synthesis process are given below.

2.1.1.1 Description of solvothermal process

A solvothermal process is a process in which a chemical reaction takes place in a closed system in the presence of a solvent, where the temperature of the system is kept higher than that of the boiling point of the solvent. It is a slight modification of the hydrothermal route, where the chemical reaction leading to formation of nanoparticles is conducted in a stainless steel autoclave. The only difference between the two processes is the use of the precursor solution other than water in solvothermal synthesis.

At the beginning of the 1990s, after the oxides era and the beginning of non-oxide ceramics and in particular the synthesis of nitrides, for example, chemical synthesis route involving non-aqueous solvents were developed out of necessity [23]. Demazeau and coworkers [24] were the first to propose the word “solvothermal” as a generic appellation including all solvents. Since, then the solvothermal reactions involving various solvents have been developed and are mainly used for preparing micro or nanoparticles with different morphology. These reactions are mainly characterized by different chemical parameters (nature of the reagents and of the solvent) and thermodynamical parameters (in particular temperature, pressure and reaction time).

a) Chemical Parameters

Two different parameters can be taken into account: the nature of the reagents and the nature of the solvent. The chemical composition of the reagents must be appropriate to that of the target materials. In addition, concentration of the reagents seems to play a role on control of the shape of nanocrystallites. Wang et al. [25], achieved control of the crystallite shape with concentration of the reagents in solvothermal preparation of CdSe and CdTe nanocrystals. Recently, V. Zarghami et al. [26], have also reported similar result on CdSe nanocrystals in which the morphology changes from nanorods to spherical nanoparticles with an increase in the amount of precursors. Thus, the interactions between reagents and solvent play important role in the solvothermal reaction.

The selection of solvent plays a key role through the control of the reaction mechanism leading to the target material. For example, Li et al. [27], in their preparation of Cu_7Te_4 using $CdCl_2$. H_2O and tellurium as reagents, observed that while the use of ethylenediamine $\{C_2H_4(NH_2)_2\}$ results in chemical reaction between the two reagents leading to the formation of the target compound, the use of diethylamine ($C_4H_{11}N$), on the other hand, didn’t result in any chemical reaction. Besides controlling the reaction, liganding property of the solvents is also known to play very important role in determining the shape of the nanocrystals. H. Wang et al. [28], in their study on the effect of ligands on CdSe nanoparticle growth, have shown that the morphology changes from spherical to rod-shape when diethanolamine ($C_4H_{11}NO_2$) is used instead of ethonolamine (C_2H_7NO) or triethanolamine ($C_6H_{15}NO_3$) as a solvent.

b) Thermodynamical Parameters

In solvothermal process, thermodynamic parameters are temperature, pressure and reaction time. The solvothermal reactions are mainly performed in mild temperature conditions ($T < 400\ ^oC$). The main impact of temperature in solvothermal processes is to differentiate two different domains where the physico-chemical properties of the solvent are modified; the subcritical and the supercritical domains [23, 29]. It can be adjusted to:

(i) stabilize a specific structural form of the final material, such as in the case of the solvothermal synthesis of hybrid vanadium oxyfluorides [30].

(ii) optimize the size and shape of nanoparticles by increasing the temperature or reaction time. For example, the size and the crystallinity of the resulting CdS nanorods are improved [31].

In most solvothermal reactions, pressure is autogeneous and closely dependent on the percentage of filling for the reaction vessel and on temperature. Due to this, the role of pressure in solvothermal processes has not yet been extensively investigated. However, pressure can play a role on the density of the reaction medium and consequently the average distance between chemical species, which determines the chemical reactivity. For example, in the preparation of Fe_3O_4 [32, 33], pressure was observed to determine the crystal growth by controlling the concentration of solvated species in the reaction medium.

In this thesis work, solvothermal reaction is performed in 110 mL capacity autoclave, which is a teflon-lined stainless steel closed cylindrical chamber. Appropriate amount of cation salt is first dissolved in 10 mL of de-ionized water and then mixed with 8 mL of ammonia solution ($NH_3 . H_2O$) under constant stirring. Anion salt is also similarly mixed with 10 mL of hydrazine hydrate ($N_2H_4 . H_2O$). The two solutions are poured in the autoclave, which is then filled with deionized water up to 80% of its volume. After 10 minutes of stirring, the closed chamber is placed inside a muffle furnace at a preset temperature of 180 ^oC for different reaction time. The reaction is performed for the given reaction time, after which precipitate obtained in the autoclave is filtered off and washed several time in distilled water and ethanol. The final product is then dried at room temperature for several hours to get the nanopowders. All chemicals used in the synthesis are of analytical grade and are used without any further purification.

2.1.1.2 Synthesis of CdSe nanorods

In this synthesis, cadmium acetate [$(CH_3COO)_2$ Cd: $2H_2O$] and sodium selenite [Na_2SeO_3] are respectively used as cation and anion precursor salts. The amount of cation and anion salts used in the synthesis is chosen so as to maintain their molar ratio at 1:1 [0.005 mol each]. To study the evolution of nanostructure with time, samples are prepared for three different reaction time, viz., 1, 3 and 5h respectively while keeping all other solvothermal chemical and thermodynamical parameters fixed.

In this solvothermal reaction, ammonia in the solvent acts as liganding agent for cadmium ions [34]. The mixing of cadmium salt with ammonia and deionized water results in the formation of cadmium complex, $[Cd(NH_3)_4]^{2+}$, which prevents uncontrolled release of Cd^{2+} ions in the solution. Hydrazine hydrate helps in generating Se^{2-} ions from sodium selenite by reducing Se to form Se^{2-} ions [35]. Ions are slowly generated such that the solubility product of CdSe exceeds the critical constant ($K_{sp}CdSe = 10^{-33}$) resulting in nucleation and growth of nanoparticles. In the process, concentration of reactants also gets depleted and unless sufficient Cd^{2+} and Se^{2-} ions are generated instantly, the nanocrystal growth will be inhibited. The controlled release of ions due to the presence of liganding agent and reducing agent, thus, results in evolution of size and morphology with reaction time. The possible reactions in the solvothermal solution can be formulated as follows.

Formation of ammonia complex,

$$Cd^{2+}(aq) + 2NH_3(aq) + 2H_2O <=> Cd(OH)_2(s) + 2NH_4^+(aq)$$

$$Cd(OH)_2(s) + 4NH_3(aq) <=> [Cd(NH_3)_4]^{2+}(aq) + 2OH^-(aq)$$

Reduction of sodium selenite,

$$Na_2SeO_3 \rightarrow 2Na^+ + SeO_3^{2-}$$

$$2SeO_3^{2-} \xrightarrow{Hydrazine\ hydrate} 2Se^{2-} + 3O_2$$

2.1.1.3 Synthesis of ZnSe nanocrystals

In this synthesis, zinc acetate [$(CH_3COO)_2$ Zn. $2H_2O$] and sodium selenite [Na_2SeO_3] are respectively used as cation and anion precursor salts. Similar to CdSe nanorods, ZnSe samples are also prepared at three different reaction times 1, 3 and 5h respectively while keeping all other solvothermal chemical and thermodynamical parameters fixed.

In the synthesis of ZnSe nanocrystals (NCs), the growth mechanism is similar to that is described for CdSe nanorods. Here, ammonia in the solvent serves the same purpose and act as liganding agent for zinc ions [34]. Hydrazine hydrate helps in generating Se^{2-} ions from sodium selenite [35]. Similar to CdSe nanorods, the critical core growth is also inhibited, which results in evolution of size and morphology with reaction time. The possible reactions in the solvothermal solution can be formulated as the following;

Formation of ammonia complex,

$$Zn^{2+}(aq) + 2NH_3(aq) + 2H_2O <=> Zn(OH)_2(s) + 2NH_4^+(aq)$$

$$Zn(OH)_2(s) + 4NH_3(aq) <=> [Zn(NH_3)_4]^{2+}(aq) + 2OH^-(aq)$$

Reduction of sodium selenite,

$$Na_2SeO_3 \rightarrow 2Na^+ + SeO_3^{2-}$$

$$2SeO_3^{2-} \xrightarrow{Hydrazine\ hydrate} 2Se^{2-} + 3O_2$$

2.1.1.4 Synthesis of CdS and ZnS powders

In the synthesis of these two sulfide compounds, cadmium acetate [$(CH_3COO)_2$ Cd: $2H_2O$] and zinc acetate [$(CH_3COO)_2$ Zn. $2H_2O$] are used as cadmium and zinc precursor respectively. Sodium sulfite (Na_2SO_3) is used as sulfur precursor. The solvent and all other solvothermal chemical and thermodynamical parameters are identical to the synthesis route for selenide compounds. The sulfide formation reaction along with the XRD, Raman and EDAX results for CdS and ZnS powders have been included as appendix I.

2.1.1.5 Synthesis of CdS-CdSe composite powders

CdS-CdSe composite powders are solvothermally synthesized using different molar ratio of the anion salts i.e., sodium selenite (Na_2SeO_3) and sodium sulfite (Na_2SO_3) so as to obtain composite powders with varying fraction of S and Se. Molar ratio of cationic salt to anionic salt is, however, maintained at 1:1 for all the synthesis. For the synthesis of each of the composite powders, cadmium acetate [$(CH_3COO)_2Cd.2H_2O$] is used as a precursor for cadmium. Composite powder samples are prepared from three different molar ratio of anion salts at 180 ^{o}C for 5h reaction time. Solution composition for the synthesis is given in appendix II.

2.1.1.6 Synthesis of ZnS-ZnSe composite powders

ZnS-ZnSe composite powders are similarly prepared by solvothermally process using different molar ratio of the anion salts i.e., sodium selenite (Na_2SeO_3) and sodium sulfite (Na_2SO_3). Molar ratio of cationic salt to anionic salt is also maintained at 1:1 for all the synthesis. Zinc acetate [$(CH_3COO)_2$ Zn. $2H_2O$] is used as a precursor for zinc ion. Samples are prepared from three different molar ratio of anion salts at 180 ^{o}C for 5h reaction time. Solution composition for the synthesis is given in appendix II.

2.1.2 Thin film preparation

Thin films of II-VI semiconducting compounds, both binary and ternary alloys can be prepared through most of the thin film deposition techniques including sol gel [36], thermal evaporation [37], e-beam evaporation [38, 39], sputtering [40, 41], atomic layer deposition [42, 43], electrodeposition [44, 45], molecular beam epitaxy [46, 47], spray pyrolysis [48, 49], chemical bath deposition [50, 51], etc. Each of the above methods has its own merits and demerits and we shall restrict our discussion only to the thermal evaporation technique, which we have employed in the present work.

2.1.2.1 Description of thermal evaporation technique

Thermal evaporation technique is one of the most widely used techniques for preparation of thin films. It consists mainly of vacuum chamber, vacuum pumps, filament and substrate holder. The physical stages of film formation consists of several steps, such as (i) sublimation of the material to be deposited to the vapour phase, (ii) transfer of vapors from the evaporant to the substrate, (iii) condensation of vapors upon arrival on the substrate and (iv) their arrangement or modifications of their binding on the substrate surface.

The evaporation rate and hence condensation have wide limits, depending upon the type of source and the material used. We have used molybdenum boat as the evaporation source. The characteristics of the films are influenced by rate of evaporation, pressure during deposition, thickness of the film, angle of evaporation, temperature of the substrate and residual atmosphere. All these parameters can be controlled in the thermal evaporation technique. Another advantage of this method is that evaporation yields a large area of films of more or less uniform thickness. The factors, which influence the nature and properties of evaporated films, are discussed below [52, 53].

(i) Effect of residual gases

Because of the collisions with ambient gas molecules, a fraction of the vapour, proportional to $\exp(-d/s)$, is scattered and hence randomized in direction within a distance ‘*d*’ during their transfer through the gas. Here ‘*s*’ is the mean free path between collisions, and is dependent on the pressure at fixed temperature. To ensure a straight line path for most of the evaporated atoms, a pressure of 10^{-4} Torr and source to substrate distance of 10 to 15 cm are necessary.

(ii) Effect of vapour beam intensity

The rate of evaporation and hence condensation can vary over wide limits depending upon the type of material and evaporation source being used. There exists a critical vapour beam density below that no condensation occurs and also a critical substrate temperature above that no film could be formed except at very high beam intensities.

(iii) Effect of substrate surface

The quality of the surface is the most important property of a substrate, since it is here where the film-substrate interaction occurs. The nature of the condensed film depends on the structure of the substrate, its temperature and cleanliness. Condensing atoms align according to the structure of the underlying surface, forming amorphous or polycrystalline layers on amorphous substrate and a single crystal substrate respectively in most cases. The adhesion of a film to the substrate is strongly dependent on the cleanliness and microscopic topography of the substrate surface [54]. Presence of contaminants on the substrate surface may increase or decrease the adhesion depending on whether absorption energy is increased or decreased.

(iv) Effect of evaporation rate

The evaporation of a material requires that it be heated to a sufficiently high temperature to produce the desired vapor pressure. The rate of evaporation of vapor atoms from a clean surface of unit area in vacuum is given by Langmuir-Dushman kinetic theory equation [52]

$$N_e = 3.513 \times 10^{22} P_e/(MT)^{1/2} \text{ [molecules cm}^{-2}\text{ s}^{-1}] \qquad \text{------------------ (2.1)}$$

where P_e is the equilibrium vapor pressure (in torr) of the evaporant under saturated-vapor conditions at a temperature T, and M is the molecular weight of the vapor species. The rate of deposition depends not only on the evaporation rate but also on the source geometry, its position relative to the substrate and condensation coefficient. An increase in the source temperature increases the kinetic energy of the incident vapor atoms, and grain size [55].

In addition to the factors discussed above, the choice of the material of evaporant (filament boat), and purity of the evaporating materials also determine the quality of the films prepared.

2.1.2.2 Preparation of CdS_xSe_{1-x} $(0 \leq x \leq 1)$thin films

CdS_xSe_{1-x} $(0 \leq x \leq 1)$ thin films are prepared on corning 1737 glass by thermal evaporation of solvothermally synthesized CdS-CdSe composite powders. It is performed using molybdenum boat in a vacuum chamber with a base pressure of about 10^{-5} mbar at a fixed substrate temperature of 200 ^{o}C on corning 1737 glass substrates. Source to substrate distance is fixed at 10 cm.

2.1.2.3 Preparation of ZnS_xSe_{1-x} $(0 \le x \le 1)$thin films

ZnS_xSe_{1-x} $(0 \le x \le 1)$ thin films are also prepared on corning 1737 glass by thermal evaporation of solvothermally synthesized ZnS-ZnSe composite powders. The thermal evaporation parameters and the substrate used for the deposition are identical to that in CdS_xSe_{1-x} $(0 \le x \le 1)$ thin films preparation.

2.2 Characterizations and models used

In the following section, we briefly review the various techniques used for characterizing the properties of the nanostructure compounds and the prepared thin films.

2.2.1 X-ray diffraction (XRD)

X-ray diffraction (XRD) is a non-destructive characterization technique based on the principle of diffraction (scattering) of x-ray radiation by the crystal planes. This technique is used to analyze a material for determination of:

- Microstructural nature of samples (amorphous or crystalline) and their phase identification (cubic, hexagonal etc.).
- Mean crystallite size and unit cell parameters
- Strain and dislocation density analysis
- Phase transitions, phase diagrams, defects etc.

In the present thesis, XRD measurements are performed using Seifert 3000 TT or Rigaku TTRAX-III diffractometer with CuK_α (λ= 1.5406 Å) radiation in 2θ range ~ 20-65° depending upon the availability of the instruments. XRD measurements of the powder and thin film samples are taken in powder and thin film mode respectively.

The mean crystallite size (*D*) are calculated using Scherrer's formula as follows

$$D = \frac{0.9\lambda}{\beta \cos\theta} \qquad \text{------------------- (2.2)}$$

where, λ is the wavelength of x-ray, β is the broadening (Full Width at Half Maximum (FWHM)) of the peak and θ is the Bragg's angle.

The dislocation density (δ) defined as the length of dislocation lines per unit volume, is estimated using the relation,

$$\delta = \frac{1}{D^2} \qquad \text{------------------- (2.3)}$$

It is a measure of the number density of defects in a crystal.

The lattice strain is determined using the relation,

$$\varepsilon = \frac{\beta \cos\theta}{4} \qquad \text{------------------- (2.4)}$$

2.2.2 Transmission electron microscopy

Transmission electron microscope (TEM, JEOL JEM 2100) has been used to study the microstructure of the powders. For TEM observation, the sample in the form of powder is dispersed in ethanol solvent followed by ultrasonication for at least 1h. A drop of the colloidal solution is placed on a carbon coated copper TEM grid (Mesh 400) and allowed to dry in a clean environment. The grid with the dried powder particles is used for the TEM observation. In the measurement, electron beams are accelerated with voltage of 200 kV and 100 μA current.

2.2.3 Scanning electron microscopy

Compositional analysis of the powders and thin films are done using energy dispersive X-ray spectroscopy (EDAX) attached to scanning electron microscope (SEM)**,** LEO 1430 VP. Morphology of the powders is also analyzed using the instrument.

The electrons are accelerated in a potential difference typically of the order of 10 – 20 keV and focused on a spot in the sample area, resulting in the transfer of energy to the spot. For analysis of the powder samples, very thin layer of the powder are spread on carbon coated tape and then gold coated to yield an electrically conducting surface for SEM and EDAX measurements. The analysis of thin film samples is however, performed by cutting a small piece of the sample along with the glass substrate and then mounting on the specimen stub using carbon tape. Conducting channel between the top surface of the sample and the metal specimen stub is made by putting a small strap of carbon tape and then coating with gold as in powder sample measurement.

2.2.4 Field emission scanning electron microscopy

Field emission scanning electron microscope (FESEM) is a type of electron microscope that images the sample surface by scanning it with a high energy beam of electrons in a raster scan pattern. Electron emitter from field emission gun is used. These types of electron emitters can produce up to 1000x the emission of a tungsten filament. However, they require much higher vacuum conditions. After the electrons beam exit the electron gun, they are then confined and focused into a small spot using metal apertures and magnetic lenses. Finally, detectors of each type of electrons are placed in the microscopes that collect signals to produce an image of the specimen. In this thesis work, the morphology of powder samples and thin film surface are obtained using Field emission Scanning Electron Microscope (FESEM), ΣIGMA ZEISS.

2.2.5 Raman spectroscopy

In material science, Raman spectroscopy is a very powerful tool to study the vibrational modes in the material for understanding the crystal structure, composition and many other fundamental properties. It is based on inelastic scattering of photons by a molecule or an atom, known as Raman Effect. The processes involve in the effect is shown in figure 2.1. Most of the molecules are initially in the ground state (labeled 0 in the figure) but because of thermal agitation some molecules will be in an excited state (labeled 1). When an incoming photon raises the molecule to an excited state, the molecule cannot remain in this virtual level, it must immediately fall back down to a lower level with the emission of a photon. If the molecule falls into the same level as it started from, there is no frequency shift in the emitted photon and the process is the well-known Rayleigh scattering. If, on the other hand, the molecule falls into a different level, the energy of the emitted photon differs from that of the incoming photon in order to conserve total energy. In this case, the emitted photon has a different frequency from that of the initial photon. The frequency can decrease or increase, depending on whether the molecule starts in the ground state or an excited state. The scattering in which the photon frequency decreases is known as Stokes scattering. Whereas the scattering process for which the photon frequency increases is called anti-Stokes scattering. Since the initial population of the excited states is usually very small, the anti-Stokes lines are much weaker than the Stokes lines and sometimes cannot be observed.

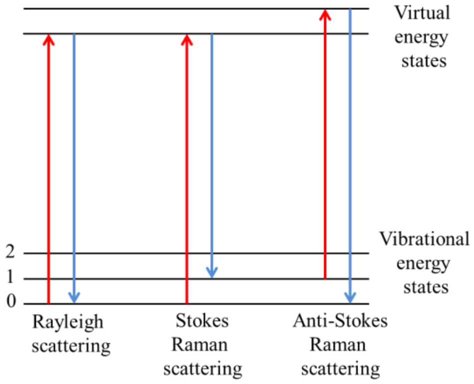

Figure 2.1: Energy level diagram showing transitions involve in Raman Effect.

In the present thesis work Horiba JY LabRam HR800 micro-Raman system is used for recording Raman scattering spectra in backscattering geometry and only Stoke shifted photons are recorded. The monochromatic argon laser excitation source with either 488 or 514.53 nm is used to record the spectra. The resolution and the recorded spectral range of Raman shifts are 1 and 100-700 cm^{-1} respectively. While recording the Raman shifts, the excitation laser radiations are tightly focused on the surface of the sample to a spot size of $\leq 1\mu m$. These studies are performed on the powder samples and thin films deposited on corning 1737 glass.

2.2.6 Photoluminescence spectroscopy

Photoluminescence (PL) spectroscopy is a contactless, nondestructive method to probe the electronic structure of materials. The intensity and spectral content of the emitted photoluminescence is a direct measure of various important material properties, including bandgap, impurity levels and defects and recombination mechanisms. It is the phenomenon in which a substance absorbs photon energy and re-emits a fraction of it as visible or near-visible radiation. It is one of many forms of luminescence (light emission) and is distinguished by photoexcitation (excitation by photons). Quantum mechanically, this can be described as an excitation to a higher energy state by absorption of energy from light and then a return to a lower energy state accompanied by the emission of a photon. When a semiconductor is excited with a light source that provides photons with energy larger than the bandgap energy, the excited electron and hole will not remain in their excited states for very long; instead, they will relax very rapidly (10^{-13} s) to the lowest energy states within their respective bands by emitting phonons. When the electron (hole) finally arrives at the bottom (top) of the conduction (valence) band, the electron-hole pair recombines radiatively with the emission of a photon (luminescence), or non-radiatively by transferring the electron's energy to impurities or defects in the material or dangling bonds at the surface. In the present work, PL measurements on powder samples are carried out using either Aminco Bowman Series 2 Luminescence Spectrophotometer or Horiba JY LabRam HR800 micro-Raman system. For PL measurements using Aminco Bowman Series 2 Luminescence Spectrophotometer, powders are ultrasonically dispersed in ethanol for 3h and then placed in a quartz cuvette. However, for measurements where Raman instrument is used, the powder samples are pressed on a glass slab to have uniform flat sample surface and then placed on the sample holder in the Raman instrument.

2.2.7 UV-Vis-NIR Spectroscopy

Transmittance spectrum of thin film samples are recorded using Shimadzu UV 3101PC spectrophotometer in the range 250-2500 nm. The recorded spectrum indicates the fraction of light transmitted by the films and the absorption due to electronic transitions from the ground state to an excited state. Interference fringes are observed in medium to transparent absorbing range due to multiple reflections from different layers of the film. Using Swanepoel's method [56], thickness and optical constants including refractive index, absorption coefficient (α), etc of the films are deduced from the interference fringes.

For a semiconductor material, the absorption coefficient, α, due to interband transition near the bandgap is described by the Tauc's relation [57].

$$\alpha h\nu = C(h\nu - E_g)^p \qquad \text{------------------- (2.5)}$$

where $h\nu$ is the energy of incident light photon, E_g is energy bandgap and C is a constant independent of ν. The values of exponent p are 1/2 and 2 for a direct gap and an indirect gap transition respectively. Using equation (2.5), the optical band gap E_g of the films are calculated from $(\alpha h\nu)^{1/2}$ vs $h\nu$ plot.

Absorbance spectra of powder samples are recorded in both transmission mode and reflection mode. While the transmission mode is recorded using Shimadzu UV 3101PC spectrophotometer, Perkin Elmer Lambda 900 UV/VIS/NIR Spectrometer with Integrating Sphere is used to record the spectra in reflection mode. In the transmission mode measurement, the powder samples are uniformly dispersed in ethanol solution and the transmission is measured using the instrument by keeping the solution in a quartz cuvette. In the reflection mode measurement, the powder samples are kept in a sample holder and the measurement is performed on it with the help of integrating sphere.

2.2.8 Thermogravimetric analysis (TGA)

Thermal stability studies are carried out by thermogravimetric analysis (TGA, Hitachi, STA 7200). It is a technique which measures the mass change of a sample as a function of temperature in the scanning mode or as a function of time in the isothermal mode. Both thermal events that do not bring about mass change, such as melting, crystallization, and glass transition as well as those that accompany mass change, such as decomposition, sublimation, reduction, desorption, adsorption and vaporization, can be measured by TGA. In this thesis work, thermal stability of the nanostructured compound semiconductors, CdSe and ZnSe are studied by TGA instrument under inert atmosphere of N_2 in the temperature range of room temperature to 800 ^{o}C with heating rate of 10 ^{o}C/min.

Kinetic parameters of thermal decomposition can be measured by different kinetic models like Ozawa method [58], Kissinger method [59], Coats-Redfern model [60], Freeman-Carrol method [61], etc. Among these methods, Coats-Redfern model and Freeman-Carrol methods are simple and requires only one heating rate whereas other methods require at least four heating rates. Out of the two methods that require only one heating rate, Coats-Redfern model is chosen for kinetic analysis of our samples as most of the thermodynamic parameters like activation energy, Arrhenius parameter, entropy change, enthalpy change and Gibbs free energy can be deduced.

In thermal decomposition, the rate of disappearance of the original substance is described by the reaction kinetic equation,

$$\frac{d\alpha}{dt} = Ae^{-(E/RT)}(1-\alpha)^{n} \qquad \text{------------------- (2.6)}$$

where α is the fraction of the original substance decomposed at time t, n is the order of reaction, A is the preexponential factor and E is the activation energy of the reaction. In nonisothermal mode, for a linear heating rate $\beta = \frac{dT}{dt}$ the following Coats-Redfern equation can be obtained by integrating and rearranging the above reaction kinetic equation.

$$\boldsymbol{Ln\left[\frac{g(\alpha)}{T^2}\right] = Ln\left[\frac{AR}{\beta E}\left(1-\frac{2RT}{E}\right)\right] - \frac{E}{RT}} \qquad \text{------------------- (2.7)}$$

where $\boldsymbol{g(\alpha)}$ is the kinetic model function.

In this thesis work, all TGA data are analyzed using the nine mechanistic equations (Table 2.1) proposed by Satava [62]. Results of the analysis are used to derive the best fit curves with the highest correlation coefficients. We observe that the best fits are obtained for geometrical contraction models, (contracting sphere and contracting cylinder). This model assumes that nucleation occurs rapidly on the surface of the crystal and the rate of degradation is controlled by the resulting reaction interface progressing towards the center of the crystal [63].

The slope of the plot of $Ln\left[\frac{g(\alpha)}{T^2}\right]$ against $1/T$ is a straight line, from which the thermal activation energy (E) is calculated. The pre-exponential factor, Arrhenius parameter (A) is also calculated from intercept of curve on Y-axis which is equal to $Ln\left[\frac{AR}{\beta E}\right]$. The kinetic parameters such as the entropy of activation (ΔS), the enthalpy of activation (ΔH) and the free energy of activation (ΔG) are calculated using the following equations [64]

$$\Delta S\ (J/Kmole) = 2.303R\left(log\frac{Ah}{k_B T_p}\right) \qquad \text{------------------- (2.8)}$$

$$\Delta H\ (kJ/mole) = E - RT_p \qquad \text{------------------- (2.9)}$$

$$\Delta G\ (kJ/mole) = \Delta H - T_p\Delta S \qquad \text{----------------- (2.10)}$$

where h is the Planck's constants and T_p is the peak temperature of DTG.

Table 2.1: Nine mechanistic equations as proposed by Satava.

Model	Equation
1-D diffusion	$\alpha^2 = kt$
2-D diffusion, cylindrical symmetry	$[(1-\alpha)\ln(1-\alpha)] + \alpha = kt$
3-D diffusion, Jander equation	$\left[1-(1-\alpha)^{1/3}\right]^2 = kt$
3-D diffusion, Ginstling-Brounshtein	$1-\left(\frac{2}{3}\right)\alpha-(1-\alpha)^{2/3} = kt$
First order random nucleation	$-\ln(1-\alpha) = kt$
Random nucleation, Avrami-Erofeyev I	$[-\ln(1-\alpha)]^{1/2} = kt$
Random nucleation, Avrami-Erofeyev II	$[-\ln(1-\alpha)]^{1/3} = kt$
Geometrical contraction, contracting cylinder	$1-(1-\alpha)^{1/2} = kt$
Geometrical contraction, contracting sphere	$1-(1-\alpha)^{1/3} = kt$

.

2.3 References

[1] G.S. Paul, P. Agarwal, Evolution of nanostructure with reaction time for ZnS synthesized by solvothermal process, Physica Status Solidi (c), 7 (2010) 909-912.

[2] H. Wang, Z. Guo, F. Du, Solvothermal synthesis of CdSe nanorods via DEA solution, Materials Chemistry and Physics, 98 (2006) 422-424.

[3] D. Xu, Z.P. Liu, J.B. Liang, Y.T. Qian, Solvothermal synthesis of CdS nanowires in a mixed solvent of ethylenediamine and dodecanethiol, J Phys Chem B, 109 (2005) 14344-14349.

[4] Y. Duan, S. Yao, C. Dai, X. Liu, G. Xu, Characterization of ZnSe microspheres synthesized under different hydrothermal conditions, Transactions of Nonferrous Metals Society of China, 24 (2014) 2588-2597.

[5] X. Liu, P. Peng, J. Ma, W. Zheng, Preparation of novel CdSe microstructure by modified hydrothermal method, Materials Letters, 63 (2009) 673-675.

[6] J.J. Zhu, Y. Koltypin, A. Gedanken, General sonochemical method far the preparation of nanophasic selenides: Synthesis of ZnSe nanoparticles, Chem Mater, 12 (2000) 73-78.

[7] J.J. Zhu, S. Xu, H. Wang, J.M. Zhu, H.Y. Chen, Sonochemical synthesis of CdSe hollow spherical assemblies via an in-situ template route, Adv Mater, 15 (2003) 156 - 159.

[8] W.K. Ho, J.C. Yu, Sonochemical synthesis and visible light photocatalytic behavior of CdSe and CdSe/TiO2 nanoparticles, Journal of Molecular Catalysis A: Chemical, 247 (2006) 268-274.

[9] T.L. Wang, Y.C. Wang, Y.H. Chang, H.Y. Hsu, W.J. Chen, Sonochemical synthesis and shape change of colloidal CdSe nanocrystals by high-intensity ultrasound, J Nanosci Nanotechno, 11 (2011) 167-173.

[10] L.F. Xi, Y.M. Lam, Y.P. Xu, L.J. Li, Synthesis and characterization of one-dimensional CdSe by a novel reverse micelle assisted hydrothermal method, J Colloid Interf Sci, 320 (2008) 491-500.

[11] X.H. Yang, Q.S. Wu, L. Li, Y.P. Ding, G.X. Zhang, Controlled synthesis of the semiconductor CdS quasi-nanospheres, nanoshuttles, nanowires and nanotubes by the reverse micelle systems with different surfactants, Colloid Surface A, 264 (2005) 172-178.

[12] J. Zhang, L.D. Sun, C.S. Liao, C.H. Yan, Size control and photoluminescence enhancement of CdS nanoparticles prepared via reverse micelle method, Solid State Communications, 124 (2002) 45-48.

[13] I.U. Arachchige, S.L. Brock, Sol-gel assembly of CdSe nanoparticles to form porous aerogel networks, J Am Chem Soc, 128 (2006) 7964-7971.

[14] H.Q. Jiang, X. Yao, J. Che, M.Q. Wang, F.T. Kong, Preparation of ZnSe quantum dots embedded in SiO_2 thin films by sol-gel process, Ceram Int, 30 (2004) 1685-1689.

[15] D.L. Ou, A.B. Seddon, Structural studies of sol-gel processed, amine functionalised ormosils doped with phenyl-capped CdSe quantum dots, Phys Chem Glasses, 39 (1998) 154-166.

[16] K. Deppert, K. Nielsch, M.H. Magnusson, F.E. Kruis, H. Fissan, Feasibility study of nanoparticle synthesis from powders of compounds with incongruent sublimation behavior by the evaporation/condensation method, Nanostruct Mater, 10 (1998) 565-573.

[17] H. Forster, C. Wolfrum, W. Peukert, Experimental study of metal nanoparticle synthesis by an arc evaporation/condensation process, J Nanopart Res, 14 (2012) 926.

[18] Y. Singh, J.R.N. Javier, S.H. Ehrman, M.H. Magnusson, K. Deppert, Approaches to increasing yield in evaporation/condensation nanoparticle generation, J Aerosol Sci, 33 (2002) 1309-1325.

[19] H. Pan, G.C. Xing, Z.H. Ni, W. Ji, Y.P. Feng, Z. Tang, D.H.C. Chua, J. Lin, Z.X. Shen, Stimulated emission of CdS nanowires grown by thermal evaporation, Applied Physics Letters, 91 (2007) 193105.

[20] P.V. Kazakevich, P.S. Yares'ko, V.S. Kazakevich, D.A. Kamynina, Gold nanoparticle production by laser ablation in liquid nitrogen medium followed by cryogenic medium substitution with ethanol, Bull. Lebedev Phys. Inst., 41 (2014) 269-274.

[21] K.H. Mohamed, M.G. Naseri, A.R. Sadrolhosseini, A. Dehzangi, A. Kamalianfar, E.B. Saion, R. Zamiri, H.A. Ahangar, B.Y. Majlis, Silver nanoparticle fabrication by laser ablation in polyvinyl alcohol solutions, Chinese Phys Lett, 31 (2014) 077803.

[22] A. Voloshko, J.P. Colombier, T.E. Itina, Comparison of laser ablation with spark discharge techniques used for nanoparticle production, Appl Surf Sci, 336 (2015) 143-149.

[23] G. Demazeau, Solvothermal and hydrothermal processes: the main physico-chemical factors involved and new trends, Res Chem Intermed, 37 (2011) 107-123.

[24] G. Demazeau, O. Martel, M. Devalette, E. Verdon, Particular compositions of rare earth oxides their preparation and their use., in: E. Patent (Ed.) European Patent, 1987.

[25] Q. Wang, D. Pan, S. Jiang, X. Ji, L. An, B. Jiang, A solvothermal route to size- and shape-controlled CdSe and CdTe nanocrystals, Journal of Crystal Growth, 286 (2006) 83-90.

[26] V. Zarghami, M.R. Mohammadi, D.J. Fray, Morphological manipulation of solvothermal prepared CdSe nanostructures by controlling the growth rate of nanocrystals as a kinetic parameter, J Electron Mater, 41 (2012) 3050-3055.

[27] B. Li, Y. Xie, J.X. Huang, H.L. Su, Y.T. Qian, A solvothermal route to nanocrystalline Cu_7Te_4 at low temperature, J Solid State Chem, 146 (1999) 47-50.

[28] H. Wang, Z. Guo, F. Du, Solvothermal synthesis of CdSe nanorods via DEA solution, Materials Chemistry and Physics, 98 (2006) 422-424.

[29] E. Kiran, J.F. Brennecke, Supercritical Fluid Engineering Science: Fundamentals and Applications (ACS Symp. Ser. 214, American Chem. Soc., Washington, DC, 1993), 1992.

[30] D.W. Aldous, N.F. Stephens, P. Lightfoot, The role of temperature in the solvothermal synthesis of hybrid vanadium oxyfluorides, Dalton Transactions, (2007) 4207.

[31] F.W.G. Li, Z.K. Zhang, Synthesis of high quality CdS nanorods by solvothermal process and their photoluminescence, J Nanopart Res, 7 (2005) 685-689.

[32] T. Dubois, G. Demazeau, Proceedings of the 4th International Symposium on Hydrothermal Reactions, Nancy, 31/08-03/09-1993, Institut Lorrain des Geosciences, Nancy, pp. 39–41., in: M. Cuney, M. Cathelineau (Eds.).

[33] D. Gérard, Impact of high pressures in solvothermal processes, Journal of Physics: Conference Series, 215 (2010) 012124.

[34] V.M. Bhuse, Chemical bath deposition of Hg doped CdSe thin films and their characterization, Materials Chemistry and Physics, 91 (2005) 60-66.

[35] J. Yang, G. Wang, H. Liu, J. Park, X. Gou, X. Cheng, Solvothermal synthesis and characterization of ZnSe nanoplates, Journal of Crystal Growth, 310 (2008) 3645-3648.

[36] H. Aydin, H.M. El-Nasser, C. Aydin, A.A. Al-Ghamdi, F. Yakuphanoglu, Synthesis and characterization of nanostructured undoped and Sn-doped ZnO thin films via sol–gel approach, Appl Surf Sci, 350 (2015) 109-114.

[37] F. Iacomi, M. Purica, E. Budianu, P. Prepelita, D. Macovei, Structural studies on some doped CdS thin films deposited by thermal evaporation, Thin Solid Films, 515 (2007) 6080-6084.

[38] R. Al Asmar, D. Zaouk, P. Bahouth, J. Podleki, A. Foucaran, Characterization of electron beam evaporated ZnO thin films and stacking ZnO fabricated by e-beam evaporation and rf magnetron sputtering for the realization of resonators, Microelectron Eng, 83 (2006) 393-398.

[39] I.S. Kim, E.K. Jeong, D.Y. Kim, M. Kumar, S.Y. Choi, Investigation of p-type behavior in Ag-doped ZnO thin films by e-beam evaporation, Appl Surf Sci, 255 (2009) 4011-4014.

[40] P.F. Yang, H.C. Wen, S.R. Jian, Y.S. Lai, S. Wu, R.S. Chen, Characteristics of ZnO thin films prepared by radio frequency magnetron sputtering, Microelectronics Reliability, 48 (2008) 389-394.

[41] M. Morales, N. Vivet, M. Levalois, J.F. Bardeau, Optimization of ZnSe-SiO_2 nanostructures deposited by radio-frequency magnetron sputtering: Correlations between plasma species and thin film composition, structural and microstructural properties, Thin Solid Films, 515 (2007) 5314-5323.

[42] R. Kudrawiec, J. Misiewicz, L. Wachnicki, E. Guziewicz, M. Godlewski, Contactless electroreflectance of ZnO layers grown by atomic layer deposition at low temperature, Semicond Sci Tech, 26 (2011) 075012.

[43] R. Solanki, J. Huo, J.L. Freeouf, B. Miner, Atomic layer deposition of ZnSe/CdSe superlattice nanowires, Applied Physics Letters, 81 (2002) 3864-3866.

[44] M.A. Islam, I.P. Herman, Electrodeposition of patterned CdSe nanocrystal films using thermally charged nanocrystals, Applied Physics Letters, 80 (2002) 3823-3825.

[45] R.K. Pandey, S.R. Kumar, A.J.N. Rooz, Photoelectrochemical and solar-cell studies of n-CdSe films grown by repeated electrodeposition cycles, Thin Solid Films, 200 (1991) 1-9.

[46] P. Boieriu, R. Sporken, Y. Xin, N.D. Browning, S. Sivananthan, Wurtzite CdS on CdTe grown by molecular beam epitaxy, J Electron Mater, 29 (2000) 718-722.

[47] C.T. Hsu, Epitaxial growth of II-VI compound semiconductors by atomic layer epitaxy, Thin Solid Films, 335 (1998) 284-291.

[48] T. Logu, K. Sankarasubramanian, P. Soundarrajan, K. Sethuraman, Hydrophilic CdSe thin films by low cost spray pyrolysis technique and annealing effects, Electron Mater Lett, 11 (2015) 206-212.

[49] Y.V. Meteleva, N.A. Radychev, G.F. Novikov, Properties of CdSe films produced via spray pyrolysis of $[Cd((NH_2)_2CSe)_2Cl_2]$, Inorg. Mater., 43 (2007) 455-465.

[50] P. Nemec, M. Simurda, I. Nemec, P. Formanek, Y. Nemcova, D. Sprinzl, F. Trojanek, P. Maly, Chemical bath deposition of CdSe and CdS nanocrystalline films: tailoring of morphology, optical properties and carrier dynamics, Physica Status Solidi (a), 205 (2008) 2324-2329.

[51] A. Goudarzi, G.M. Aval, R. Sahraei, H. Ahmadpoor, Ammonia-free chemical bath deposition of nanocrystalline ZnS thin film buffer layer for solar cells, Thin Solid Films, 516 (2008) 4953-4957.

[52] K.L. Chopra, Thin Film Phenomena, McGraw-Hill Book Company, New York, 1969.

[53] A. Goswami, Thin Film Fundamentals, New Age International Limited, New Delhi, 1996.

[54] J.C. Hsieh, C.J. Liu, Y.H. Ju, Response characteristics of lead phthalocyanine gas sensor: effects of film thickness and crystal morphology, Thin Solid Films, 322 (1998) 98-103.

[55] P.S. Vincett, W.A. Barlow, G.G. Roberts, Structure and properties of vacuum-deposited thin films: A new basic relationship, Journal of Applied Physics, 48 (1977) 3800-3806.

[56] R. Swanepoel, Determination of the thickness and optical constants of amorphous silicon, Journal of Physics E: Scientific Instruments, 16 (1983) 1214.

[57] J. Tauc, R. Grigorovici, A. Vancu, Optical properties and electronic structure of amorphous Germanium, Physica Status Solidi (b), 15 (1966) 627-637.

[58] T. Ozawa, A New Method of Analyzing Thermogravimetric Data, B Chem Soc Jpn, 38 (1965) 1881-1886.

[59] H.E. Kissinger, Reaction Kinetics in Differential Thermal Analysis, Analytical Chemistry, 29 (1957) 1702-1706.

[60] A.W. Coats, J.P. Redfern, Kinetic Parameters from Thermogravimetric Data, Nature, 201 (1964) 68-69.

[61] T. Hatakeyama, Z. Liu, Handbook of Thermal Analysis JOHN WILEY & SONS, Chichester, 1998.

[62] V. Šatava, Mechanism and kinetics from non-isothermal TG traces, Thermochimica Acta, 2 (1971) 423-428.

[63] A. Khawam, D.R. Flanagan, Solid-State Kinetic Models: Basics and Mathematical Fundamentals, The Journal of Physical Chemistry B, 110 (2006) 17315-17328.

[64] R. Liu, T. Zhang, L. Yang, Z. Zhou, Effect of particle size on thermal decomposition of alkali metal picrates, Thermochimica Acta, 583 (2014) 78-85.

Chapter 3

Synthesis and studies of II – VI nanostructured semiconductors: CdSe and ZnSe binary compounds

In this chapter, we report the solvothermal synthesis of CdSe nanorods and ZnSe nanocrystals using mixed solvent of hydrazine hydrate, ammonia solution and de-ionzed water. CdSe and ZnSe with direct bandgap of 1.68 and 2.7 eV [1] respectively in cubic phase, are important II-VI compound semiconductors with a large range of potential applications in solar cells [2-4], solar coatings [5], optical windows [6], LEDs [7-9], sensors [10, 11], etc. Like other nanostructured materials, nanodimensional CdSe and ZnSe also exhibits interesting size and morphology dependent physical properties, which are different from the bulk properties. Due to both higher surface-to-volume ratio and an increase in band gap energy as a result of quantum size effect, nanostructured material of these compounds possess enhanced photosensitivity, thus, making these materials strong candidates for photovoltaic cells [2, 3, 12], sensors [10, 13], etc. But, at the same time, thermal stability is another important aspect that needs to be considered when dealing with nanodimensional materials. CdSe and ZnSe in bulk form have high thermal stability with a melting point of about 1512 and 1793 K respectively [14]. However, in nanomaterials, the reduced dimensions results in increase in dislocation density, cracks, and other discontinuities in the crystal structure, which reduces thermal stability. For these reasons, synthesis of high quality CdSe and ZnSe nanocrystals with a control over their size and morphology is necessary. It is also necessary to investigate thermal stability of the nanostructures to understand their usability in devices. With these motivations, CdSe and ZnSe nanocrystals are prepared at fixed composition of the solvent, the precursors, temperature for different reaction time and evolution of nanostructure with the reaction time is studied. Thermal stability of the nanoparticles is also studied using thermogravimetric analysis (TGA) and the mechanism of thermal decomposition is reported.

3.1 Results and discussion

3.1.1 Studies on CdSe nanorods

3.1.1.1 Structural properties

Figure 3.1 shows XRD patterns of the CdSe nanorods. For convenience in discussion, the samples prepared at 1, 3 and 5 h reaction time are labelled as CdSe_1h, CdSe_3h, and CdSe_5h respectively. The spectra of all the samples show 9 (nine) characteristic peaks, which are all identified as peaks corresponding to planes of wurtzite phase of CdSe. It is observed that (002) plane is most prominent in all the samples and thus, indicates preferential growth along this direction. Lattice parameters ‘a’ and ‘c’ are calculated from all the diffraction peaks. The values as given in table 1 are comparable to the standard lattice parameters, i.e., 4.299 and 7.010 Å respectively [PDF # 772307]. Average crystallite size and lattice strains are calculated using Williamson Hall method [15], which employs an equation relating the crystallite size (*D*) and the lattice strain (ε) with full width at half maxima (FWHM), i.e., $\frac{\beta_{hkl} Cos\theta_{hkl}}{\lambda} = \frac{\kappa}{D} + \frac{4\varepsilon Sin\theta_{hkl}}{\lambda}$, where θ_{hkl} is the peak position corresponding to the (*hkl*) plane, β_{hkl} is the FWHM, κ is the shape factor, and λ is the wavelength of CuKα radiation used for the XRD. In this method, the average crystallite size and the lattice strain are respectively obtained from the Y-intercept and the slope of the $\frac{\beta_{hkl} Cos\theta_{hkl}}{\lambda}$ vs $\frac{Sin\theta_{hkl}}{\lambda}$ plot.

The Williamson Hall plots for the three samples are given in fig. 3.2 (a) - (c). The data points in these plots correspond to planes of only the prominent peaks in XRD. The deduced average crystallite size, dislocation density and lattice strain are given in table 3.1. The crystallite size increases with increase in reaction duration and is largest for CdSe_5h sample. The change in dislocation density also follows the size variation with smallest value for CdSe_5h. However, the lattice strain is lowest for CdSe_3h sample as shown in figure 3.2 (d).

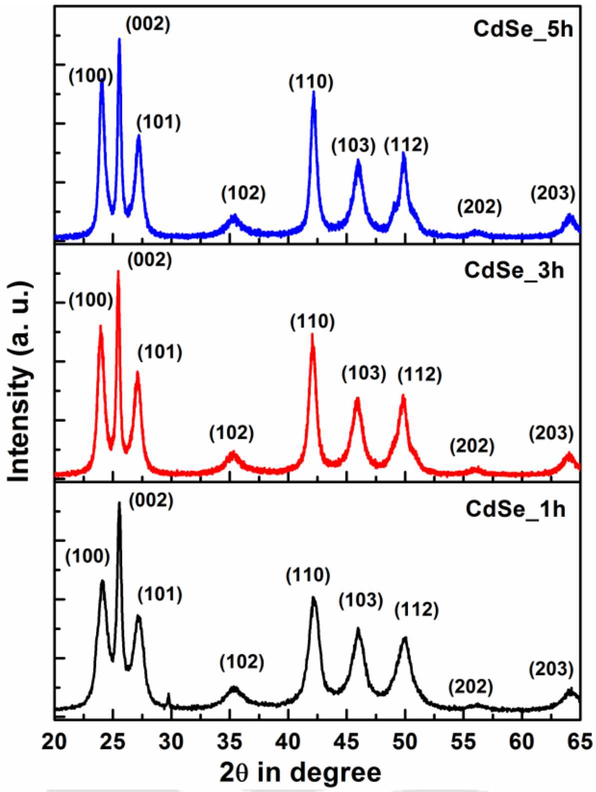

Figure 3.1: XRD patterns of CdSe nanorods.

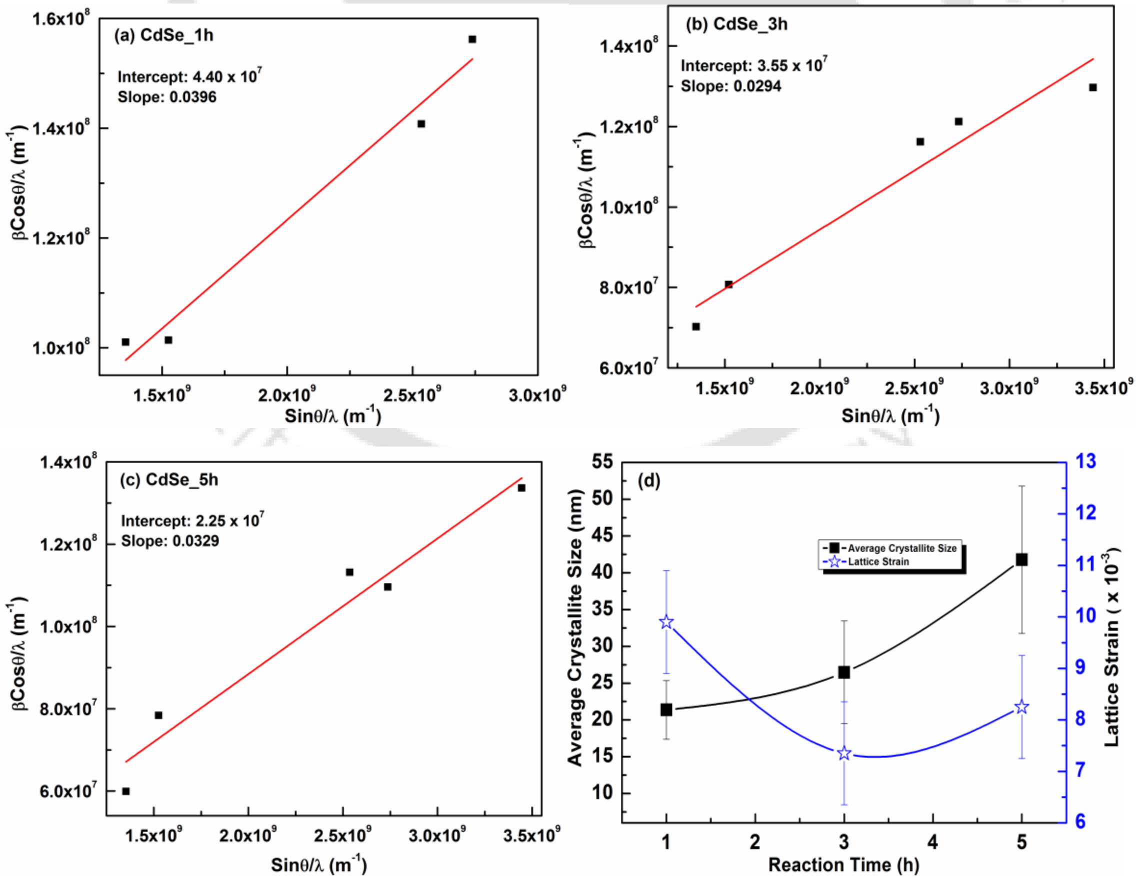

Figure 3.2: Williamson Hall plot of CdSe nanorods (a) CdSe_1h, (b) CdSe_3h and (c) CdSe_5h. (d) Plot of average crystallite size and lattice strain against reaction time with error bar.

Table 3.1: Structural parameters of CdSe nanorods.

Sample	Lattice constant (Å)		Lattice strain	Dislocation density (lines/m^2)	Average crystallite size (nm)
	‘a’	‘c’			
CdSe_1h	4.275±0.003	6.981±0.003	0.0099±0.0010	2.19 x 10^{15}	21.36±4
CdSe_3h	4.289±0.002	7.003±0.003	0.0074±0.0010	1.43 x 10^{15}	26.47±7
CdSe_5h	4.278±0.003	6.986±0.004	0.0082±0.0010	5.73 x 10^{14}	41.77±10

3.1.1.2 Composition and morphology studies

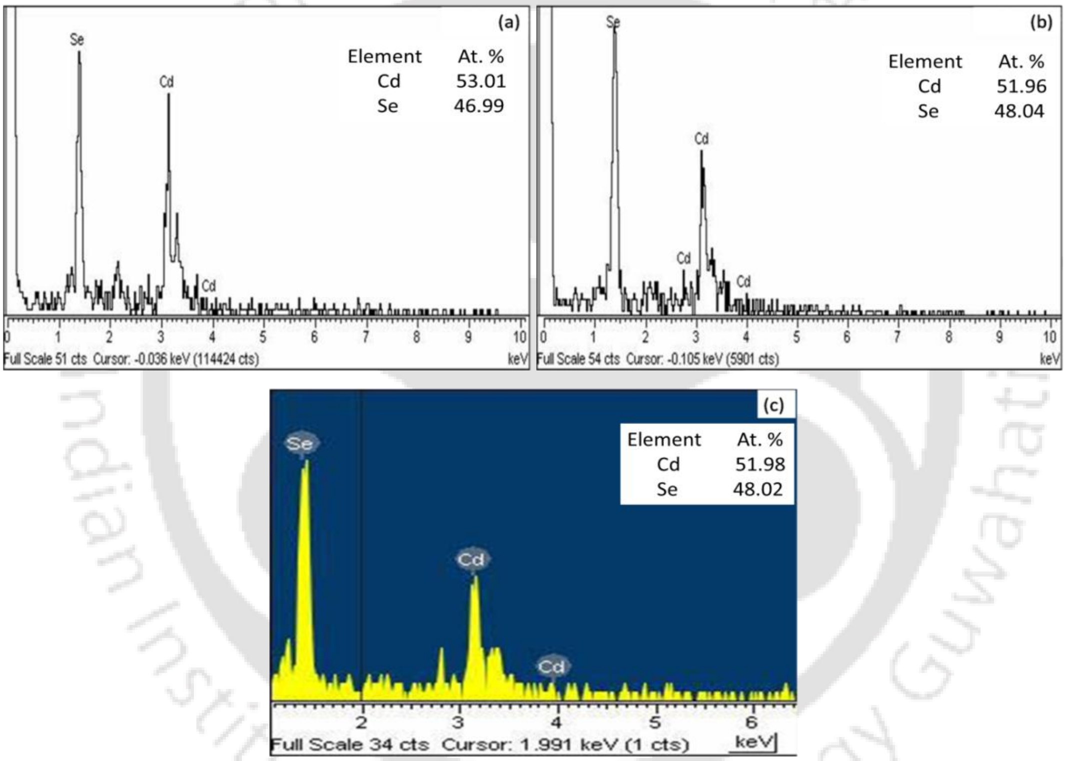

Figure 3.3: EDX spectra of CdSe nanorods; (a) CdSe_1h, (b) CdSe_3h and (c) CdSe_5h.

Figure 3.3 (a) - (c) show EDX spectra of the CdSe nanorods. The atomic percentage composition as given along with the EDX spectra are an average taken over 3 - 4 measurements. Synthesized nanorods are chemically pure and slightly cadmium rich. The CdSe_1h sample, in particular is highly rich in cadmium and the stoichiometry improves with increase in reaction time.

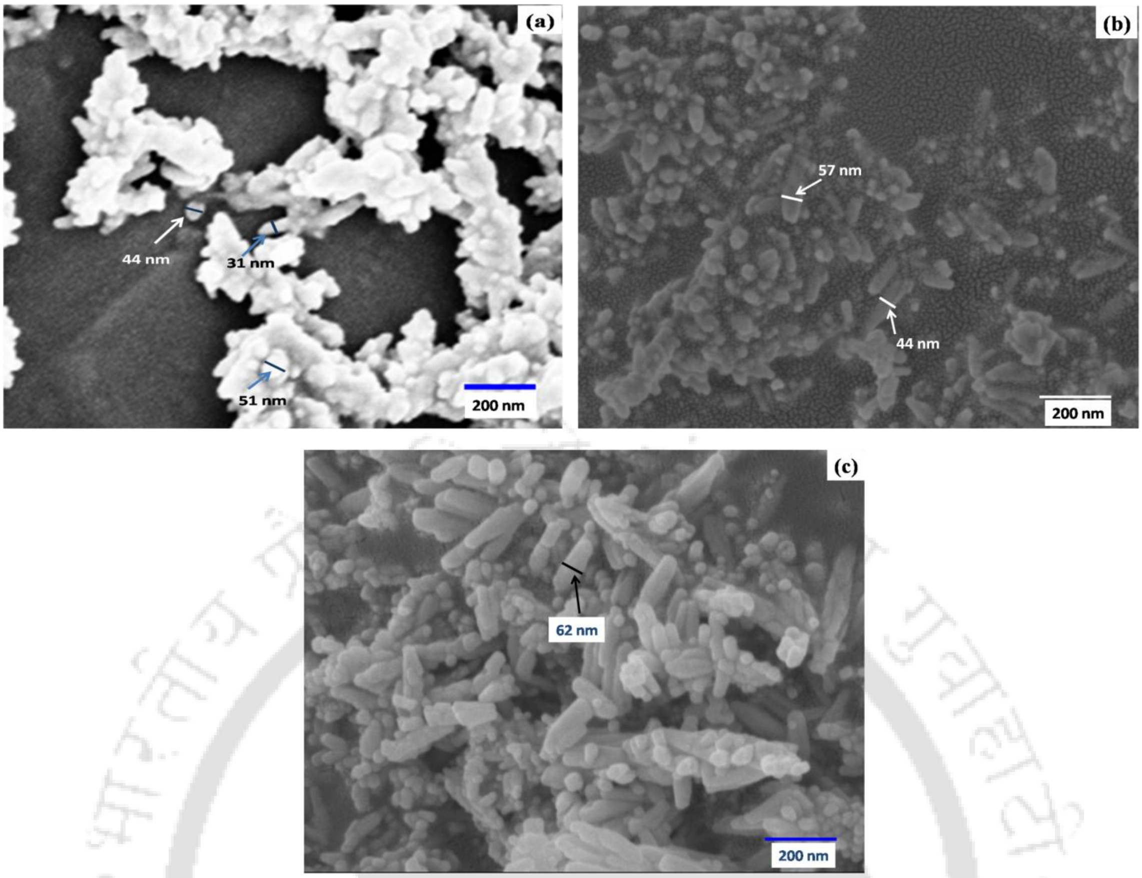

Figure 3.4: FESEM images of CdSe nanorods; (a) CdSe_1h, (b) CdSe_3h and (c) CdSe_5h.

Figure 3.4 (a) - (c) show FESEM images of the CdSe nanorods. Though particle size and morphology in each of the sample are broadly distributed, there is a change in morphology and average size of the particles in the samples with reaction time. While particles in CdSe_1h sample are mostly spherical and oval shaped, the particles for longer reaction time samples are mostly elongated rod-shaped. Diameter of the nanorods also improves with reaction time as indicated in the figures.

The observed changes in structural parameters, compositional stoichiometry and the particle size are a result of the growth process of the nanorods as discussed in chapter 2 section 2.1.1.2. Since the nanocrystal growth is inhibited and takes place in a controlled process, the crystallite size and the dimension of the nanorods are expected to improve with reaction time. Longer reaction time is also believed to provide sufficient time for atoms to occupy its lattice position resulting in improved crystallinity. The relatively slow rate of generation of Se^{2-} ions in comparison to Cd^{2+} ions is probably responsible for poor stoichiometry in sample prepared at lower reaction time, i.e., CdSe_1h.

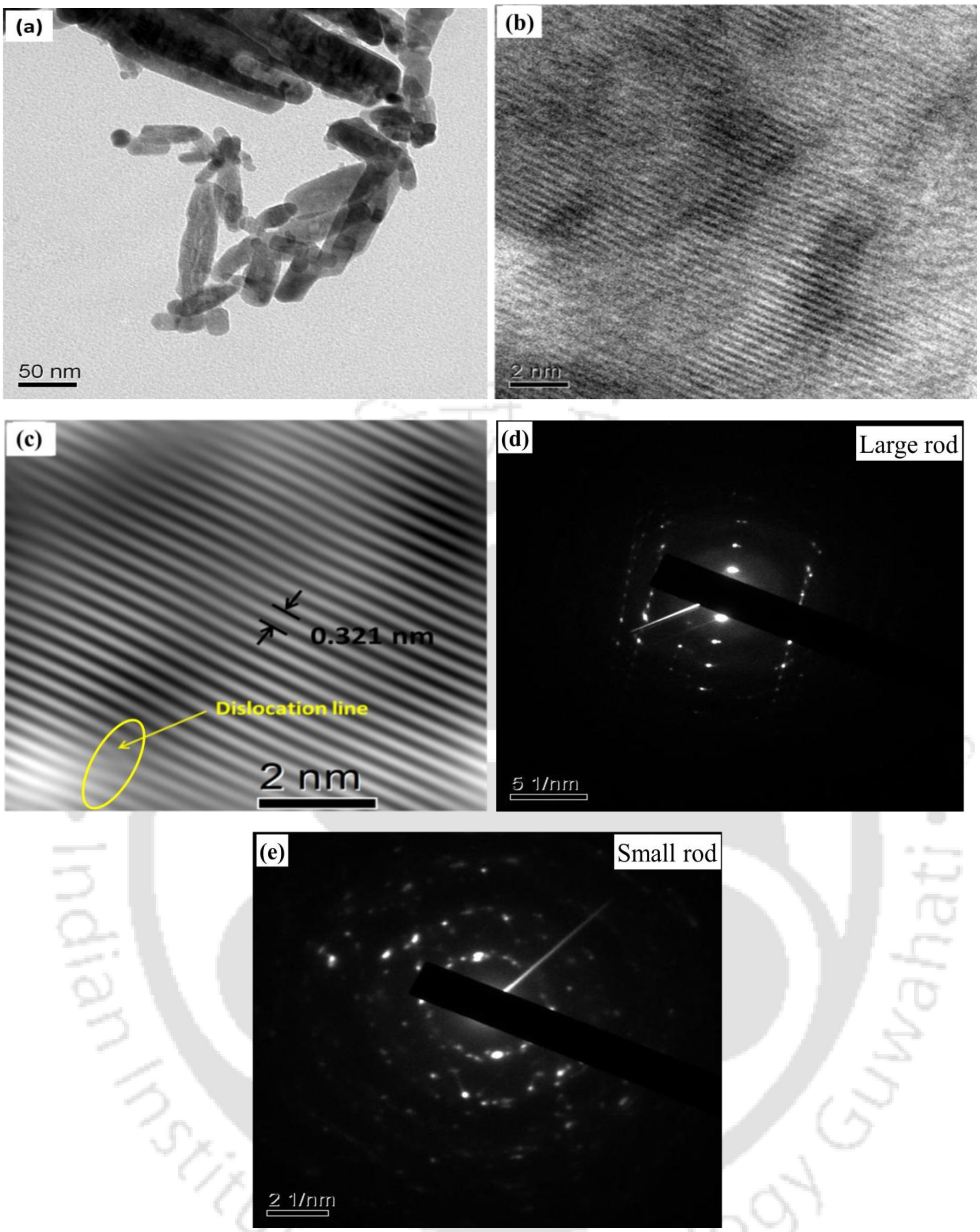

Figure 3.5: (a) TEM, (b) HRTEM, and (c) IFFT HRTEM images of CdSe_5h nanorods. (d) and (e) are SAED pattern images taken on large and small nanorods of CdSe_5h sample.

Figure 3.5 (a) shows the TEM image of CdSe_5h. The particles are mostly rod shaped but with broad distribution in size. Inverse fast Fourier transform (IFFT) is performed on the atomic planes shown in HRTEM image as in fig. 3.5 (b). Interplanar distances of atomic planes are measured on the IFFT HRTEM image. The crystal planes shown in the image corresponds to (101) plane of wurtzite CdSe with a d-spacing of 0.321 nm. Figure 3.5 (d) and (e) show the SAED pattern taken on larger and smaller nanorods respectively. Larger nanorods are found to have well defined diffraction pattern while the diffraction pattern on smaller particles is less defined and diffused, thus indicating broad distribution in crystallinity in the sample.

3.1.1.3 Thermal stability studies

Figure 3.6 (a) - (c) show thermogravimetric analysis (TGA), differential thermal analysis (DTA) and derivative thermogravimetry (DTG) curves of the CdSe nanoparticles. The TGA curves of all the three samples show similar change in weight as the samples are heated from room temperature to 800 ^{o}C. With the increase in temperature, both CdSe_3h and CdSe_5h samples show gradual weight loss (approx. 1 %) till 412 and 492 ^{o}C respectively. CdSe_1h sample also show similar gradual weight loss till about 340 ^{o}C, where a sudden change in weight occurs resulting in weight loss of about 2 %. As the temperature is increased further, interestingly all the samples show a small amount of weight gain until thermal decomposition takes place. The decomposition in all the three samples results in weight loss of about 35%. However, as is evident from the TGA curves and the DTG peaks, the onset temperature and the rate of weight loss slightly differ from one sample to another. The onset temperature for CdSe_1h is highest and is at about 600 ^{o}C, whereas for CdSe_3h and CdSe_5h samples decomposition takes place at 585 ^{o}C and 590 ^{o}C respectively. The DTG curve for CdSe_1h sample shows three peaks indicating three sets of TGA slopes corresponding to three steps of decomposition. The first peak being the most prominent among the three indicates maximum rate of weight loss in the decomposition process and is associated with a weight loss of about 16 %. The DTG curves of both CdSe_3h and CdSe_5h samples show two peaks corresponding to two steps of decomposition. In both the samples, the DTG peak at higher temperature is more prominent and relates to the faster decomposition process with more weight loss. In these samples, only about 10 % of the weight is lost in the first decomposition step. The possible chemical and physical transformations that cause the observed decomposition steps are discussed later.

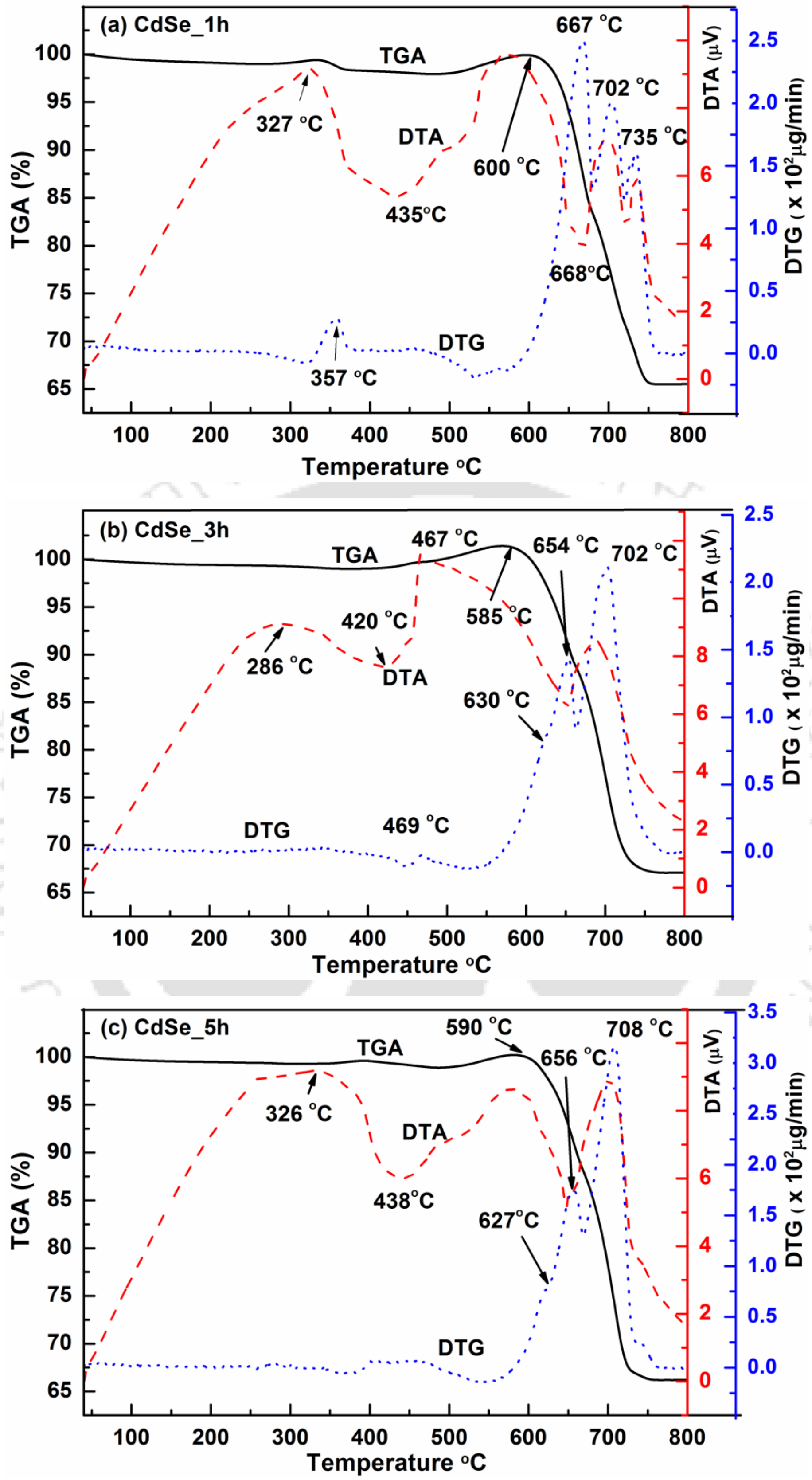

Figure 3.6: TGA, DTG and DTA curve of CdSe nanorods: (a) CdSe_1h, (b) CdSe_3h and (c) CdSe_5h.

DTA curves show endothermic and exothermic processes that take place during heating of the samples. In all the samples, the small gradual weight loss at lower temperature is associated with a broad endothermic peak. The first step of thermal decomposition in all the samples is associated with an endothermic process. The DTG peak for this step (at $\sim 656 - 667$ ℃) coincides with the dip in DTA. The second step of decomposition is associated with what appears to be exothermic peak at~ 700 ℃. The CdSe_1h sample shows an additional peak in DTG at ~ 735 ℃, which is again accompanied by an exothermic peak in DTA.

The observed small amount of weight loss at lower temperature before the thermal decomposition is often reported in TGA of nanoparticles [16-18]. It is due to the evaporation of impurities such as absorbed water and the residual traces of solvents and reagents contained in the nanoparticles. The temperature at which the evaporation of these impurities takes place depends on the nature of impurities and the nanoparticles. Other than a small fraction of weight loss due to impurities, the CdSe nanorods are quite stable up to significantly high temperature. As indicated by the weight loss in TGA, the impurities amount to about 1 % of the total weight in CdSe_3h and CdSe_5h. On the other hand, the total content of the impurities is about 2 % of the total weight of the material in CdSe_1h. This implies that the sample with shorter reaction time, i.e., CdSe_1h has more impurities due to high surface to volume ratio. The slight increase in weight while heating above 500 ^{o}C as observed in TGA curves has also been reported for ZnSe polycrystal [19] and on the same lines, it has been assigned to the diffusion of the purging gas N_2 in the porous nanoparticles.

To deduce the thermodynamic parameters that are associated with the thermal decomposition, the decomposition kinetics are analyzed using Coats Redfern method [20] as discussed in chapter 2 section 2.2.8. Attempts are made to fit our experimental data with all nine mechanistic equations for $g(\alpha)$ [21]. It is found that our results are best fitted with the contracting cylinder model, which defines $g(\alpha)$ as according to the relation $1-(1-\alpha)^{1/2}=kt$, where k is the Boltzmann constant and t is the time. In this model, nucleation is assumed to occur rapidly on the surface of the cylindrical nanoparticles and the rate of degradation is controlled by the resulting reaction interface progressing toward the center of the crystal [22].

Figure 3.7 (a) - (c) show the plot of $Ln\left[\frac{g(\alpha)}{T^2}\right]$ against 10^3/T for contracting cylinder model. The kinetic parameters such as the entropy of activation (ΔS), the enthalpy of activation (ΔH) and the free energy of activation (ΔG) are calculated using the equations

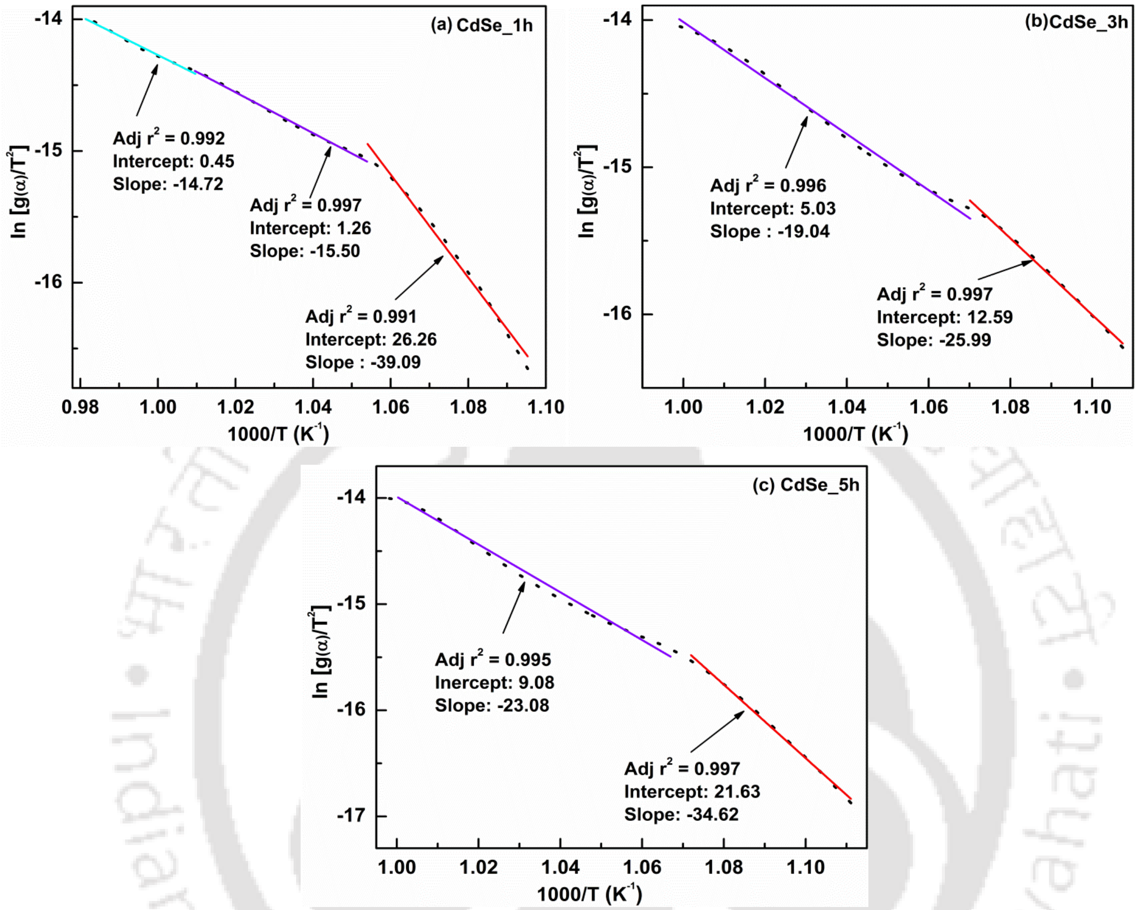

Figure 3.7: Coats Redfern plot of thermal decomposition of CdSe nanorods using contracting cylinder model. The Model function is given by $g(\alpha) = 1 - (1-\alpha)^{1/2}$.

Table 3.2: Thermodynamic parameters in thermal decomposition of CdSe nanorods.

Sample	**Decomposition**	**Activation energy E_a (kJ/mol)**	**Arrhenius Parameter**	**DTG Peak temperature T_p (^oC)**	**Entropy change ΔS (J/mol-K)**	**Enthalpy change ΔH (kJ/mol)**	**Gibbs Free Energy change ΔG (kJ/mol)**
CdSe_1h	Step 1	325	4.6×10^{16}	667	65	317	256
	Step 2	129	2.6×10^{5}	702	-151	121	268
	Step 3	127	1.1×10^{5}	735	-159	114	274
CdSe_3h	Step 1	216	3.6×10^{10}	654	-52	208	258
	Step 2	158	1.4×10^{7}	702	-118	150	265
CdSe_5h	Step 1	288	4.0×0^{14}	656	25	280	257
	Step 2	192	9.5×10^{8}	708	- 83	184	265

given in chapter 2 section 2.2.8. All the calculated thermodynamic parameters are given in table 3.2. For the first step of decomposition, the activation energy and the corresponding Arrhenius parameter of CdSe_1h is larger than the other two samples. However, for the second step of decomposition, the activation energy and the associated Arrhenius parameter increase as we go from one sample to another with longer reaction time. The change in thermal activation energy for the formation of activated complex as observed in the second step of decomposition is in agreement with that reported in literature in which the activation energy is lowered with the reduction in dimension [23-25]. Since, the reduction of particle size increases the surface to volume ratio of particles, density of dislocations, cracks and other discontinuities; increase in the number of active sites on the surface favourable for nucleation is anticipated for short duration samples. The unexpectedly large activation energy in the first step of decomposition of CdSe_1h sample could be related to larger amount of nitrogen already diffused in the nanorods. As mentioned before, the amount of weight loss due to impurities in this sample is larger than the weight lost in the other two samples. When comparing the TGA curves in the three samples, it can be seen that the CdSe_1h sample still gains weight even at the onset of dissociation temperature of the other two samples. Around this onset of dissociation temperature, it is possible that the diffusion of inert N_2 gas into the porous CdSe_1h nanorods and weight loss due to decomposition from the surface occur simultaneously. Because of larger porosity and specific surface area in CdSe_1h sample, N_2 diffusion is dominant and results in the apparent delay in thermal decomposition. However, once the decomposition is initiated in CdSe_1h sample, the rate as well as the amount of weight loss is larger than the other two samples.

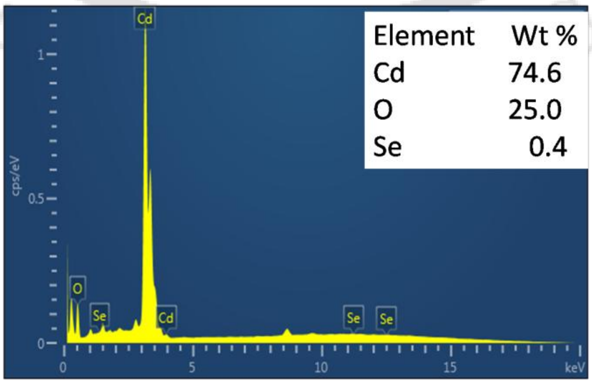

Element	Wt %
Cd	74.6
O	25.0
Se	0.4

Figure 3.8: EDX spectra of the residue of TGA measurement of CdSe_5h nanorods.

Table 3.3: Elemental weight changes due to decomposition in CdSe_5h.

Weight before decomposition (μ-gm)	Composition before degradation				Weight after decomposition (μ-gm)	Composition after degradation			Weight loss in Wt %
	Element	Atomic %	Weight %	Weight in μ-gm		Element	Weight %	Weight in μ-gm	
6627	Cd	51.98	60.9	4036	4390	Cd	74.6	3275	18.9
	Se	48.02	39.1	2590		Se	0.4	18	99.3
						O	25.0	1097	

To understand the actual chemical and physical transformation in the decomposition, EDX measurement is performed on the residue of CdSe_5h sample. The spectrum is shown in figure 3.8. The spectrum shows that the resulting compound after thermal decomposition contains large fraction of cadmium atoms, significantly large amount of oxygen atoms and very small traces of selenium atoms. The CdSe nanorods after passing through thermal decomposition are almost completely oxidized. Table 3.3 shows the elemental weight changes in the decomposition of CdSe_5h sample. At the end of the decomposition, about 18.9 weight % of Cd and 99.3 weight % of Se are lost. And about 25 weight % of O is gained in the process. This observation implies that the decomposition of the nanorods must have involved dissociation of the CdSe bonds and subsequent evaporation of some portion of Cd and most of the Se, which is accompanied by oxidation of residual Cd. It is also possible that small fraction of residual Se and other elements in the end product recrystallize to form $CdSe_xO_{1-x}$.

As given in table 3.2, the changes in activation enthalpy associated with all the steps of decomposition are positive implying that these steps are all associated with absorption of heat (endothermic). The positive value of ΔH associated with the first step of decomposition is thus, in agreement with the endothermic peak in the DTA curves. In this step, it is likely that heat absorbed by the nanorods results in removal of excess cadmium and dissociation of Cd-Se chemical bonds from the surface and subsequent evaporation of Se atoms. Since, the boiling point of bulk Se (~ 685 ^{o}C) is lower than the value for bulk Cd, which is 767 ^{o}C (approx.); in the temperature range of the first decomposition step, it is possible that evaporation of Se takes place while evaporation of Cd is unlikely to occur. The dissociation of Cd-Se chemical bonds in this step is expected to increase the disorder and the entropy change is thus likely to be positive in agreement with the calculated values. Since CdSe_1h nanorods are smaller and possess larger specific surface area, the weight loss in this decomposition step for the CdSe_1h sample is larger than the other two samples. Meanwhile, the enthalpy change associated with the second and the third decomposition steps appears to contradict the DTA curves. But it is likely that the apparent exothermic peak in DTA curves is partly due to the relatively large increase in sample temperature because of the significant weight loss in the decomposition. In this step, the thermal energy supplied is expected to dissociate most of the Cd-Se chemical bonds in the sample and evaporate almost all of the Se atoms. In the TGA measurement, amount of heat given to the reference sample and the CdSe nanorods in the sample compartment being equal, the significant weight loss in the decomposition step can result in positive DTA peak, which may not necessarily be associated with exothermic process. However, since, the entropy change in the second step is negative in all the samples and as we also observe the presence of O in the residue of CdSe_5h sample, it is possible that the second decomposition step also undergoes exothermic process resulting into recrystallization to form CdO and $CdSe_xO_{1-x}$ structures. As a result, the material is in the more ordered state than that after first step of decomposition. The Gibbs free energy of activation (ΔG) as given in table 3.2 is positive for all the steps of decomposition in all the samples. It shows that the decomposition steps are not spontaneous and have to be thermally activated.

3.1.1.4 Optical properties

Figure 3.9 (a) and (b) show the absorbance spectra of CdSe nanorods measured in transmission and reflection mode respectively. These measurements are performed as per the experimental details described in chapter 2 section 2.2.7. The concentration of solution used in transmission mode measurements is fixed at 0.26 mM for all the samples. All the samples in both measurements show broad absorption with an absorption edge having its onset at about 685 nm in CdSe_5h sample, which shifts to lower wavelength for samples prepared at shorter reaction time. The absorption onset wavelength of 685 nm in CdSe_5h corresponds to an energy gap of 1.81 eV, which is assigned to the direct transition in the bandgap of the sample and is larger than the reported bulk value of about 1.68eV [1].

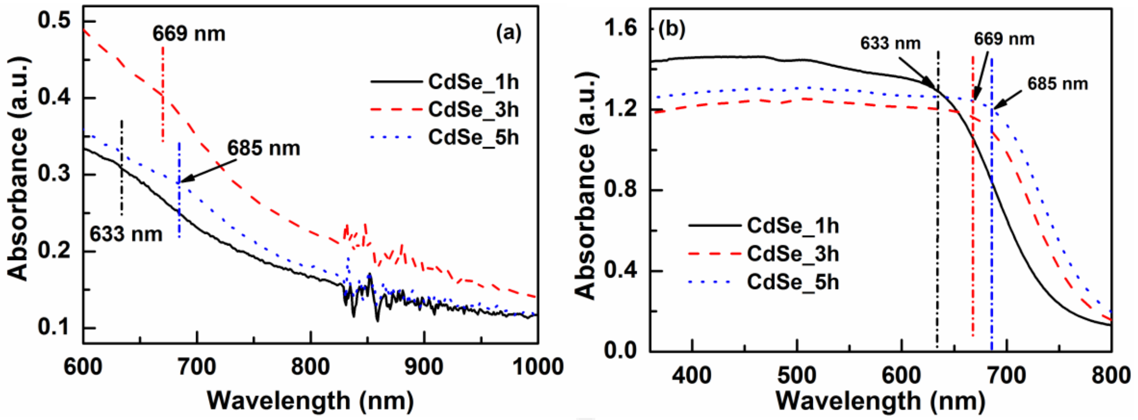

Figure 3.9: Absorbance spectra of CdSe nanorods taken in (a) transmission mode and (b) reflection mode.

The observed shift in absorption edge and the corresponding changes in the energy gap correspond to the reduction in particle size as is evident from the FESEM images. It is, therefore, apparent that the observed change in bandgap energy could be due to size dependent quantum confinement effect. However, since the nanorods diameter of the samples, which vary from 31 nm in CdSe_1h to 62 nm in CdSe_5h is much larger than the excitonic Bohr radius of bulk CdSe (only about 5.6 nm) [26], strong confinement effect that may significantly alter the bandgap is not possible. By employing Brus equation, Chukwuocha et al. [27], have shown that strong confinement limit for CdSe is at size 3.84 nm, which corresponds to confinement energy of about 1.015 eV. It has been shown that moderate confinement energy of about 0.13 eV, as observed in CdSe_5h sample, is possible only at particle size of about 8 nm. Therefore, only weak confinement effect due to change in electron-hole interaction energy, i.e., shifting of exciton energy states to higher energies is expected [28]. Thus, the observed phenomenon cannot be explained merely from the quantum size effect in nanoparticles.

Another factor that may cause change in bandgap energy is lattice strain. Thean et al. [29], theoretically calculated the bandgap widening of Si nanocrystals as a function of strain and showed that the coupling between the Si nanocrystal geometry and the symmetry generated by the strain potential can enhance confinement in the quantum dot. Experimental reports on several nanocrystals are found to be in agreement with this calculation [30-32]. Hence, strain induced enhancement of confinement is believed to be contributing for the bandgap widening as observed in our samples. As deduced from XRD, the lattice strain in these nanorods is quite large. And as also is evident from HRTEM image, the nanorods are characterized by the presence of number of dislocations. Thus, it is likely that the band structure in these samples would be altered by the lattice strain and results in enhanced confinement effect as observed.

The observed broad absorption edge in all the samples could be due to the large distribution in particle size as seen in FESEM and TEM images. Since large distribution in size is inherently associated with broad distribution in strain, both the size and strain induced confinement effects are believed to be responsible for the absence of sharp absorption edge.

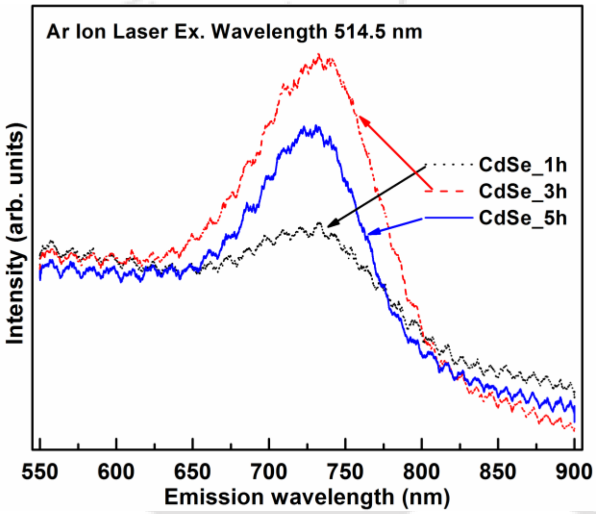

Figure 3.10: Room temperature photoluminescence (PL) spectra of CdSe nanorods taken with Ar ion laser excitation of 514.5 nm wavelength and 0.8 mW power.

Fig. 3.10 gives room temperature PL spectra of CdSe nanorods recorded using Ar ion laser source with 514.5 nm wavelength and 0.8 mW power. In the measurement range, only a single broad PL peak centered at around 725 nm is observed in all the samples. Under the same set of experimental condition, the PL peak of CdSe_1h sample is weakest and the peak for CdSe_3h sample is strongest.

It is expected that a PL peak corresponding to exciton emission from a single nanocrystal to be narrow. The observed broad emission band in our samples suggests the presence of large distribution in particle size in the nanorods. This is in agreement with XRD data, FESEM and TEM images of the CdSe nanorods. The strain and particle size induced confinement effect in the band edge emission of different size nanoparticles in each sample could result in the broad emission peak.

Surface of nanocrystals prepared by most of the prevailing synthesis route is usually characterized by the presence of large density of dangling bonds which can induce defects and adatoms, which in turn result in surface levels [33-36]. Since, nanocrystals have large specific surface area, the surface levels formed by defects and adatoms significantly influence the luminescent property of the material. The surface levels give rise to electronic states within the bandgap. These mid-gap states fill up to the Fermi level with electrons that originate in the bulk of the material and typically quench the PL intensity [34]. Since, the number of defects and the specific surface area in nanocrystals increase as the size of the nanocrystals decreases, the PL intensity quenching by the surface states will be more effective for smaller particles. This could be the reason for lower PL peak intensity as observed in CdSe_1h.

Another factor that could influence PL intensity is the high density of dislocations associated with high lattice strain. Dislocations in nanocrystals could form extended defect states, which usually act as a non-radiative recombination centers in semiconductor nanocrystals [37, 38]. Since, CdSe_3h sample has lowest lattice strain among the three samples prepared in this work, it is possible that the sample may have lowest non-radiative recombination centers that diminishes the PL intensity. This could explain the observed variation in PL intensity in the three samples.

3.1.1.5 Raman scattering studies

Fig. 3.11 shows room temperature Raman spectra of CdSe nanorods recorded using Ar ion laser with excitation wavelength of 514.5 nm. The spectra of both CdSe_3h and CdSe_5h exhibit a broad LO phonon mode with peak center at 204 cm^{-1}, which is slightly shifted towards lower wave number at 200 cm^{-1} in CdSe_1h. In comparison to the reported bulk LO phonon mode peak position at 210 cm^{-1}, the observed LO phonon mode in all the samples are red shifted. Extent of the red-shifting is even more pronounced for CdSe_1h sample. This size dependent red-shifting is quite common in Raman spectra of nanoparticles and is attributed to the result of the relaxation of the momentum conservation ($q \neq 0$) [39, 40]. Due to the negative phonon dispersion curve [41], the LO phonon mode is red-shifted once the phonon modes away from the zone center are activated.

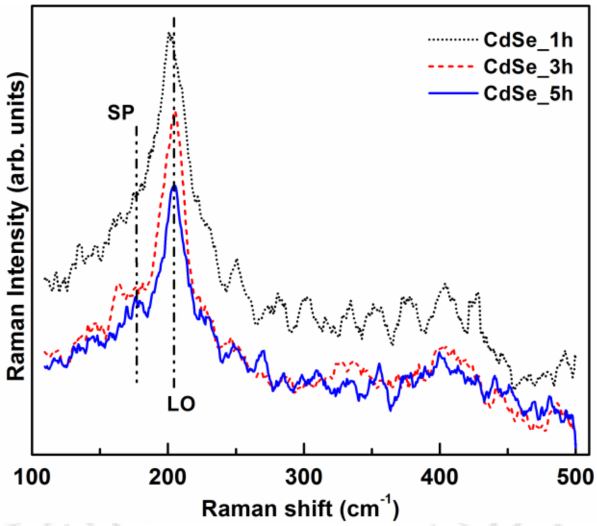

Figure 3.11: Room temperature Raman spectra of CdSe nanorods.

The shape of the LO phonon band in all the samples is slightly asymmetric, with a more pronounced low-frequency wing. Again, this asymmetry is often observed in nanocrystals, and is attributed to scattering by surface phonons whose contribution increases with the surface to volume ratio. However, rather low signal to noise ratio encumbers correct separation of the contribution of the surface phonons and determination of the surface phonon and LO phonon band parameters. Nevertheless, by visual inspection, the FWHM of LO phonon mode can be seen to be much larger than reported bulk value in II-VI materials, which is usually of the order of 7 – 8 cm^{-1} [42]. The increased FWHM as often reported in other nanocrystals is due to the nano size effect. The wide distribution in particle size in each sample also contributes to the broadening.

In addition to the LO phonon, very weak overtone 2LO phonon signature is also observed around 400 cm^{-1} in all the samples. Again, based on visual inspection, ratio of overtone to fundamental frequency (I_{2LO}/I_{LO}) slightly increases with increase in particle size, i.e., from CdSe_1h to CdSe_5h. It is a measure of the strength of the electron-phonon interaction [43]. The observed result thus suggest an increase in electron-phonon interaction with particle size. It is in agreement with some of the previous reports on semiconductor nanoparticles [44], where similar observation is reported. Theoretical formalism of Schmidt-Rink et al. [45] has also indicated that the strength of electron-phonon interaction should decrease for small nanoparticles.

3.1.2 Studies on ZnSe nanocrystals

3.1.2.1 Structural properties

Fig. 3.12 (a) shows XRD patterns of the samples prepared under different solvothermal reaction times. The spectra of all the samples have 3 (three) characteristic peaks, which are identified as peaks corresponding to (111), (220) and (311) planes of the cubic phase (zinc blende) of ZnSe. In addition to these characteristic peaks of ZnSe, peaks corresponding to (100), (002), (101) and (110) planes of ZnO are also observed in ZnSe_1h and ZnSe_3h samples. Lattice parameter ‘a’ is calculated from the characteristic diffraction peaks of ZnSe. The values as given in table 3.4 are comparable to the standard lattice parameter, i.e., 5.618 Å [PDF # 800021]. With the increase in reaction time, the diffraction peaks corresponding to the ZnSe planes become narrower, implying that the crystallinity of products is continuously improved. Average crystallite size and lattice strains are calculated using Debye Sherrer’s formula. The deduced average crystallite size, dislocation densities and lattice strains are given in table 3.4. The crystallite size is in the range of a few nanometers and is increased with increase in reaction time. The dependence of average crystallite size and lattice strain on the reaction time is shown in fig. 3.12 (b).

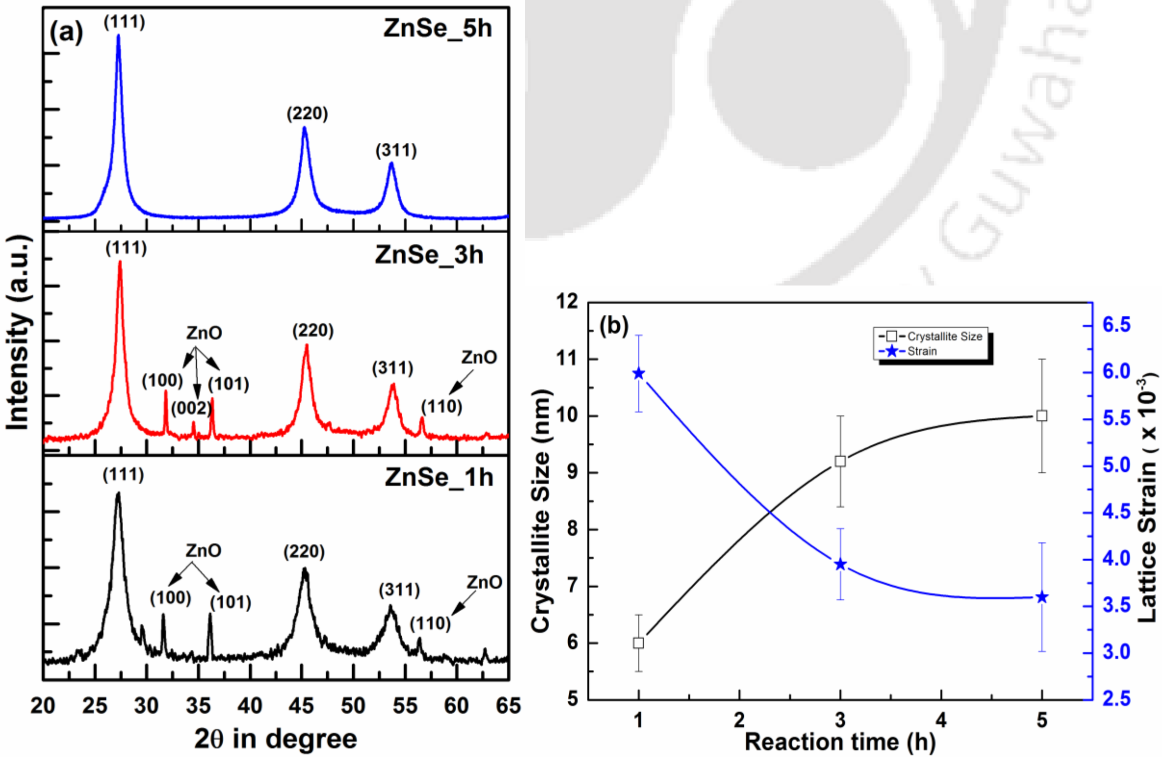

Figure 3.12: (a) XRD pattern of ZnSe powders, (b) Plot of crystallite size and lattice strain against reaction time.

Table 3.4: Structural parameters of ZnSe nanoparticles.

Sample	**Lattice constant ‘a’ (Å)**	**Lattice strain ‘ε’**	**Dislocation density (lines per m^2)**	**Crystallite size (nm)**
ZnSe_1h	5.67 ± 0.01	$5.99 \pm 0.41\times 10^{-3}$	$2.74\pm 0.05 \times 10^{16}$	6.0 ± 0.5
ZnSe_3h	5.63 ± 0.02	$3.95\pm 0.38 \times 10^{-3}$	$1.19\pm 0.22\times 10^{16}$	9.2 ± 0.8
ZnSe_5h	5.67 ± 0.01	$3.60\pm 0.58 \times 10^{-3}$	$9.91\pm 0.33\times 10^{15}$	10.0 ± 1.0

3.1.2.2 Composition and morphology studies

Figure 3.13 (a) - (c) show SEM images of ZnSe nanocrystals. The composition of the particles shown in the images is identified using EDX. As indicated in the figures, the ZnSe particles do not have regular shape. While some of the particles grow in spherical shape, there are rod shape formations as well. In agreement with ZnO peaks as observed in the XRD patterns, bulk rod shaped micron size ZnO formation is also found in ZnSe_1h and ZnSe_3h samples. A section of the SEM images of these two samples showing the formation of bulk ZnO is included as an inset to the respective SEM images. As seen from the SEM images, there is a large distribution in particle size in all the samples. While some of the particles have dimension in nanometres, large micron size spheres are also observed.

Similar to CdSe nanorods synthesis, the ZnSe nanocrystal growth is also inhibited and occurs in a controlled manner, the crystallite size and the dimension of the nanocrystals are expected to improve with reaction time. The remarkable difference in this case is that the ZnSe nanocrystals grow mostly as spheres in contrast to rods formation as observed in CdSe. It has been reported that the type of ligands play an important role in the morphology of the nanocrystals [46, 47]. But in both the cases the solvothermal reactions leading to the nanocrystal synthesis take place under the same set of experimental conditions with same ligands. Though the reason for the difference in morphological change in the two nanocrystal synthesis is not clear and needs further investigation, it appears that rod formation is thermodynamically more favourable in wurtzite crystal structure while it is not in zinc blende structure. In case of shorter synthesis time, the relatively slow rate of generation of Se^{2-} ions in comparison to Zn^{2+} ions is probably responsible for the formation of ZnO from the excess amount of Zn ions released in the solution. The bulk rod shaped ZnO with wurtzite crystal planes as observed in 1 and 3h samples support the previous statement.

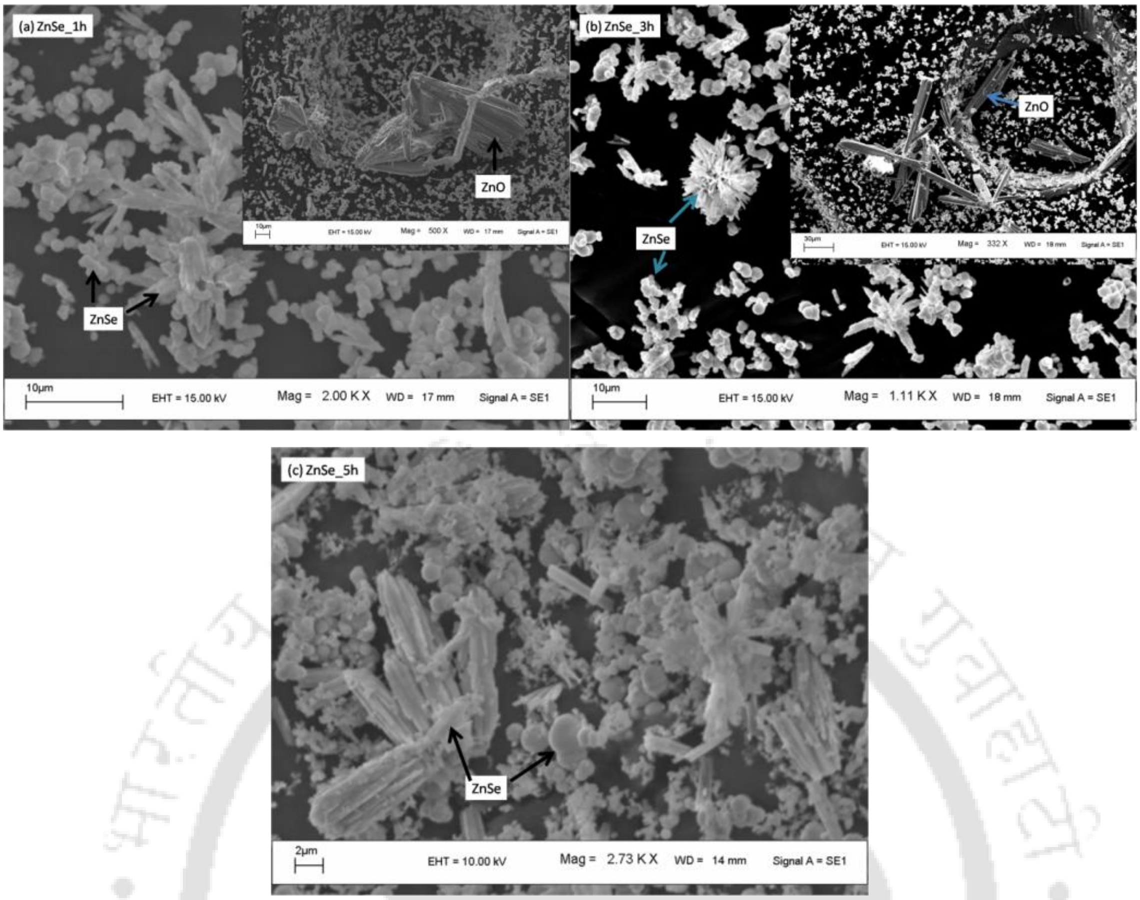

Figure 3.13: SEM images of ZnSe nanocrystals.

3.1.2.3 Thermal stability studies

Figure 3.14 (a) - (c) show thermogravimetric analysis (TGA), differential thermal analysis (DTA) and derivative thermogravimetry (DTG) curves of the ZnSe nanocrystals. The TGA curves of all the samples show similar weight loss as the samples are heated from room temperature to 800 ^{o}C. With the increase in temperature, the samples show gradual weight loss before thermal decomposition takes place. The weight loss before the onset of thermal decomposition in ZnSe_1h amount to about 4% of the original weight. In ZnSe_3h, the similar weight loss amount to about 3%, whereas in ZnSe_5h sample, only 2% of the original weight is lost. Above 350 ^{o}C, thermal decomposition in ZnSe_1h takes place with DTG peak at 429 ^{o}C and involves weight loss of about 30 %. This decomposition step is then followed by gradual weight loss and finally results in about 43 % weight loss at 800 ^{o}C. In ZnSe_3h and ZnSe_5h samples, the decomposition involves initial step involving small amount of weight loss with weak DTG peaks at 388 and 371 ^{o}C respectively, which is followed by abrupt weight loss (rapid decomposition) occurring

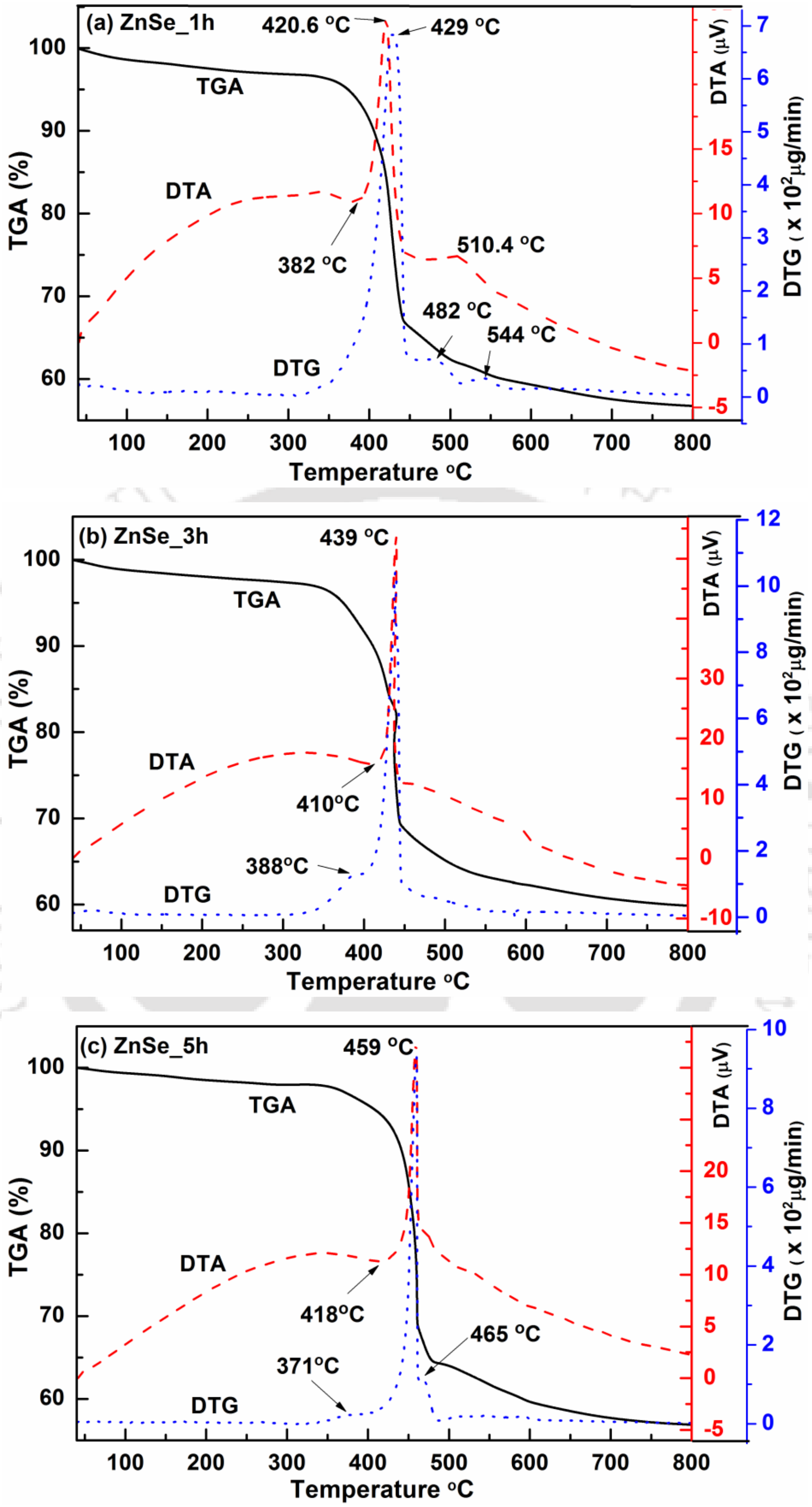

Figure 3.14: TGA, DTA and DTG of ZnSe nanocrystals.

almost instantaneously involving large fraction of the materials. Similar to ZnSe_1h, the decomposition in these samples is again subsequently followed by gradual weight loss. The DTG peak temperature associated with the thermal decomposition differs from one sample to another; increasing for samples prepared at longer synthesis time.

In all the samples, the gradual weight loss at lower temperature is accompanied with gradually changing DTA curve; slowly lowering the slope as it approaches an endothermic peak at the initial stage of thermal decomposition. Above this endothermic peak, the DTA curve in all the samples show a sharp positive peak at temperature close to the respective DTG peaks. Since, in all the samples the positive DTA peak is associated with sudden weight loss it may or may not relate to exothermic process as discussed already in the TGA measurement of CdSe.

The observed small amount of weight loss at lower temperature before the thermal decomposition is most likely caused by the evaporation of impurities as also observed in CdSe nanorods. It is observed in ZnSe nanocrystals that the weight loss corresponding to these impurities is lower in samples prepared for longer reaction time. This is because of the larger specific surface area in smaller particles, which results in more adsorbed impurities. Lack of sufficient reaction time in samples prepared for shorter reaction time may also results in more unwanted impurities.

The observed increase in DTG peak temperature for samples prepared at longer reaction time indicates an improvement in thermal stability in these samples. Since, particle size determines the thermal stability of nanoparticles as discussed in chapter 1 section 1.1.2, this observation is probably due to an increase in particle size for samples prepared for longer reaction time [23-25]. However, it is not possible to clearly identify the changes in particle size with reaction time from SEM images because of the large distribution in particle size and shape. Nevertheless, longer reaction time samples are expected to have larger particles according to the growth mechanism as discussed in chapter 2 section 2.1.1.3. It is also evident from XRD that samples prepared for longer reaction time evolve into particles with larger average crystallite size with lower dislocation densities.

To deduce the thermodynamic parameters that are associated with the thermal decomposition, the decomposition kinetics are analyzed using Coats Redfern method [20] as discussed in chapter 2 section 2.2.8. Since, the decomposition in 3 and 5h samples takes place within a very small temperature range; we cannot perform analysis using Coats Redfern method in these samples. We attempt to fit ZnSe_1h sample using all nine mechanistic equations for $g(\alpha)$ [21], as described in chapter 2 section 2.2.8. Fig. 3.15 (a) – (c) show the Coats-Redfern plots for three of the nine mechanistic equations, which are best matching with our experimental result. The range of the plot is chosen corresponding to the temperature range within which thermal decomposition takes place.

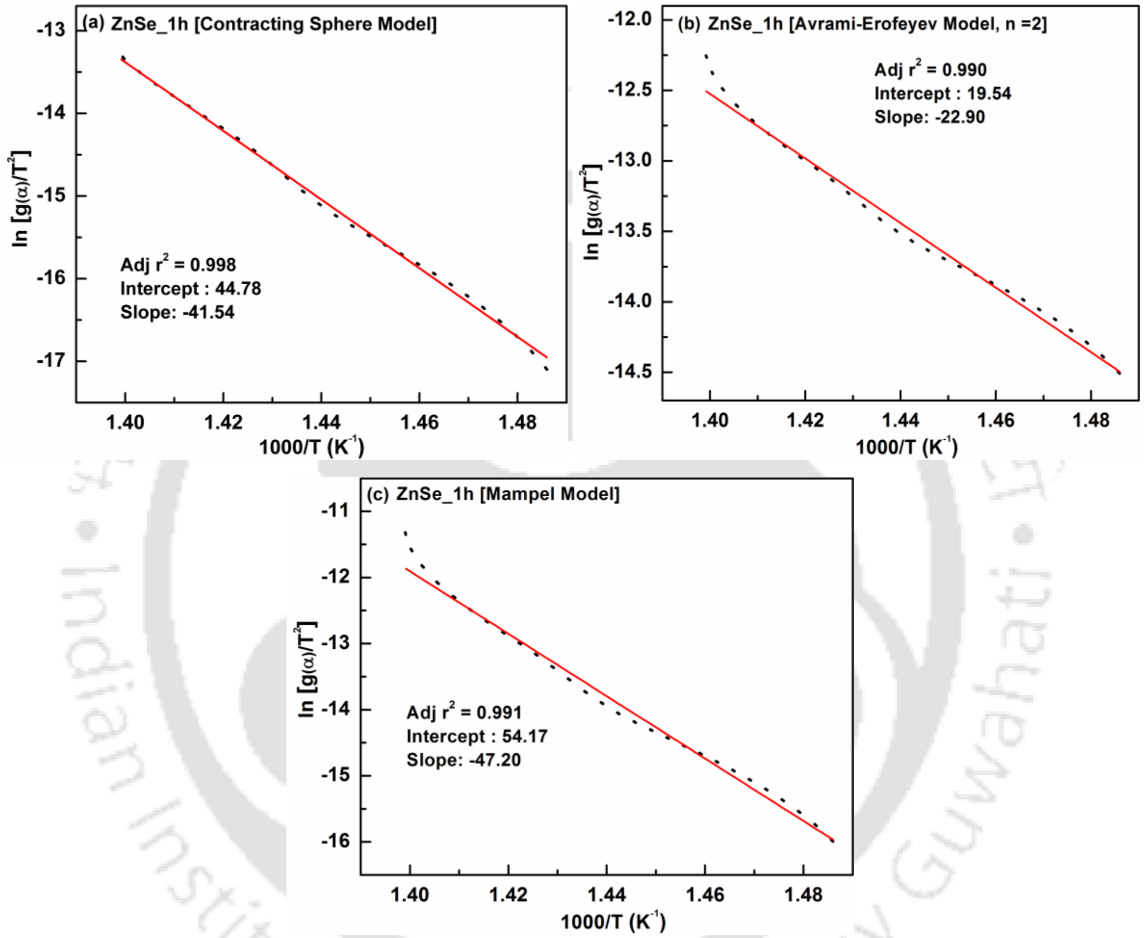

Figure 3.15: Plot of $Ln\left[\frac{g(\alpha)}{T^2}\right]$ against 10^3/T of ZnSe nanoparticles for various kinetic models (a) Contracting sphere, (b) Avrami-Erofeyev model (n = 2), (c) Mampel model.

All these three models appear to fit very well with our result. But the morphology of the ZnSe nanocrystals and the nature of the observed decomposition, which takes place with high decomposition rate, best matches with the assumptions of contracting sphere model [22], which defines $g(\alpha)$ as according to the equation $1-(1-\alpha)^{1/3} = kt$, where k is the Boltzmann constant and t is the time. The kinetic parameters such as the entropy of activation (ΔS), the enthalpy of activation (ΔH) and the free energy of activation (ΔG) are calculated using the equations given in chapter 2 section 2.2.8. All calculated thermodynamic parameters are given in table 3.5. The activation energy for thermal decomposition as deduced using contracting sphere model is 345 kJ/mol, which is comparable with the value obtained using Mample model (or first order nucleation model). Calculations using all the three models result in increase in entropy, enthalpy and Gibb's free energy. The positive value of activation enthalpy implies that heat is gained in this process, i.e., endothermic and results in decomposition amounting to increase in disorder in the system (positive ΔS).

Table 3.5: Thermodynamic parameters of thermal decomposition of ZnSe_1h nanocrystals.

Model	Adj. R^2	Activation energy E_a (kJ/mol)	DTG Peak temperature T_p (^{o}C)	Entropy change ΔS (J/mol-K)	Enthalpy change ΔH (kJ/mol)	Gibbs Free Energy change ΔG (kJ/mol)
Contracting Sphere	0.998	345	429	222	339	184
Avrami-Erofeyev	0.990	190	429	7	184	180
Mample	0.991	392	429	301	386	175

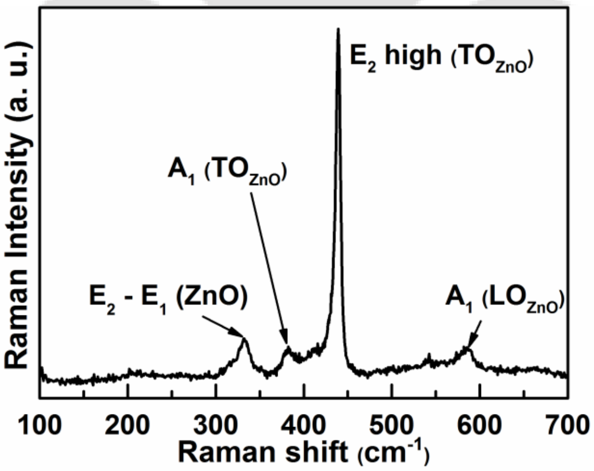

Figure 3.16: Raman spectra of the residue of TGA measurement of ZnSe_1h nanocrystals.

Figure 3.16 shows the Raman spectra of the residual sample, ZnSe_1h after TGA measurement. The peaks in the measurement range as identified in the figure correspond to phonon modes of ZnO. Since, the decomposition doesn't end after this step and the process continued till almost up to 800 ^{o}C with weak DTG peaks at 482 and 544 ^{o}C, we believe that this step with a mass loss of 30 % is due to the dissociation of Zn-Se chemical bond and subsequent evaporation of most of the Se atoms starting from the surface of the nanocrystals and progressing towards the center. The slow decomposition process, which follows this step and also accompanied by two DTG peaks (482 and 544 ^{o}C) and a weak DTA at 510 ^{o}C, is probably associated with evaporation of Se and some fraction of Zn from the bulk of the nanocrystals and exothermic reaction of residual zinc with oxygen to form ZnO. Gibbs free energy of activation (ΔG) gives information about the stability of the system. The observed increase in Gibbs free energy (positive ΔG) as given in table 3.5, is an indication that the reaction is not spontaneous and has to be activated.

3.1.2.4 Optical properties

Figure 3.17 (a) - (c) show the photoluminescence (PL) spectra of ZnSe nanocrystals recorded using an excitation wavelength of 300 nm in the wavelength range of 390 to 550 nm. All the samples prepared for different reaction time exhibit a broad PL peak at around 467 nm. The shape and the appearance of shoulder on the longer and the shorter wavelength sides clearly indicates that the PL peak is a result of overlapping of number of emission lines. The PL peak in each sample is, thus, deconvoluted so as to obtain individual emission lines that are responsible for the observed broad peak. Blue emission at around 454 nm in ZnSe_5h, which is denoted as NBE in the deconvoluted spectra, is attributed to excitonic recombination corresponding to the near-band edge emission of ZnSe. This peak is blue shifted to a small extent relative to the bulk value of 460 nm (corresponding to bulk bandgap of 2.7 eV [1]) due to the weak confinement effect in the nanocrystals. The corresponding NBE blue emission line in ZnSe_3h and ZnSe_1h are further shifted towards lower wavelength. The strongest emission line identified in the figure as D_1 is probably due to superposition of emission lines involving shallow defects and band edge emission of few bigger particles. The presence of broad shoulder on the longer wavelength side of the PL peak is interpreted as transitions corresponding to deep level defects identified as D_2, D_3 and D_4 in the deconvoluted spectra. These defect states are probably a result of dislocations, stacking faults, zinc vacancy and interstitial states in the nanocrystals. The green luminescence in particular, i.e., D_4 can be attributed to the recombination of an electron and photogenerated hole caused by surface defects [48]. In ZnSe_1h sample, additional luminescence peak at 439 nm is observed. The origin of this peak is not clearly understood, but, it could be caused by transitions corresponding to defect states in ZnO, which is also present in this sample.

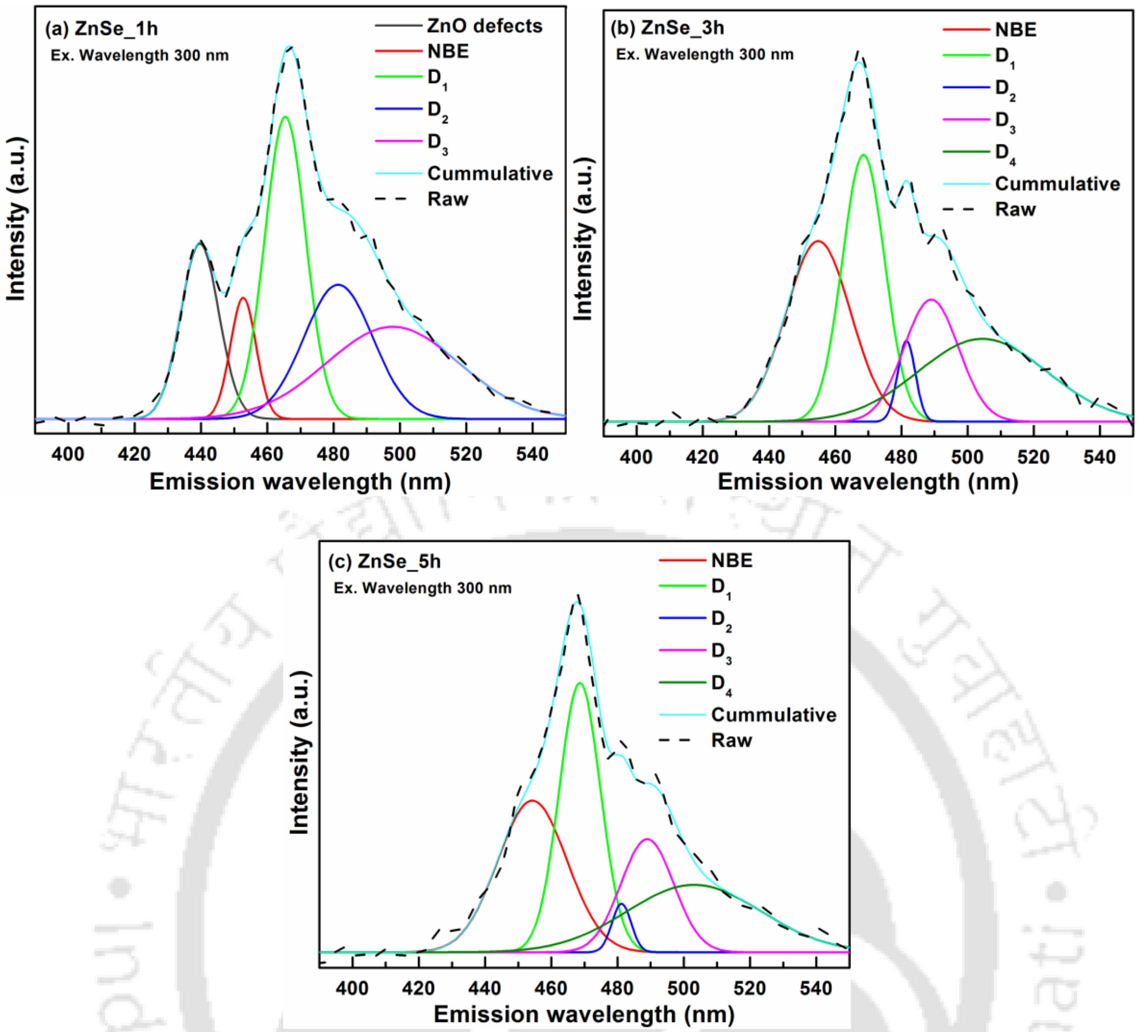

Figure 3.17: Room temperature photoluminescence (PL) spectra of (a) ZnSe_1h, (b) ZnSe_3h and (c) ZnSe_5h nanocrystals.

It is interesting to observe in the PL spectra of our samples that the transition via defect states is more dominant than the NBE transition. This could be partly due to inhibition of the NBE emission by the non-radiative recombination centers that are associated with large dislocations and strains in our samples as observed in XRD.

3.1.2.5 Raman scattering studies

Figure 3.18 shows the Raman spectra of ZnSe nanocrystals. All the samples show asymmetrically broadened LO phonon mode at around 245 cm^{-1}, which is red-shifted from the reported bulk value of 250 cm^{-1} [14]. In addition to this broad LO phonon, we have signature of 2-LO and other disorder induced phonons in the measurement range. The observed red-shifting and the asymmetric broadening of the LO phonon mode are often reported in Raman spectra of nanodimensional materials [49-51]. The phonon confinement effect and the increased specific surface area in smaller dimensional materials are responsible for these observed changes. Due to the negative phonon dispersion curve, the LO phonon mode is red-shifted once the phonon modes away from the zone center are activated [52, 53]. The asymmetry in the LO line shape, however, cannot be explained from the relaxation of q = 0 selection rule due to the small dispersion of phonons as was reported from macroscopic continuum dielectric model analysis [54]. This is due to the increased number of surface phonon modes in small nanocrystals.

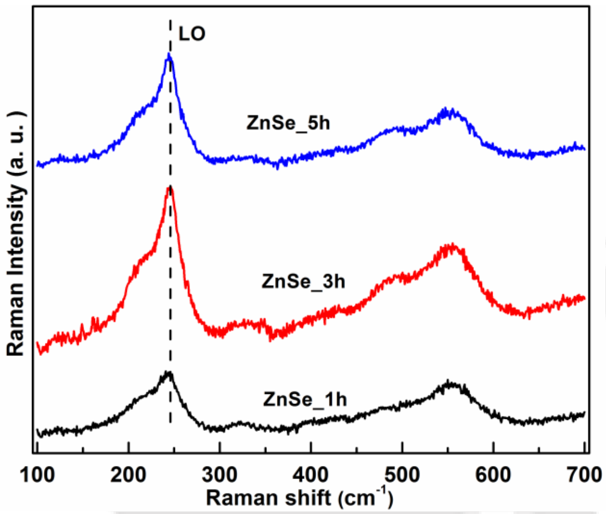

Figure 3.18: Room temperature Raman spectra of ZnSe nanocrystals.

To obtain the surface phonon and other phonon band parameters, the highly asymmetric LO phonon is deconvoluted using Gaussian line shape function in all the three samples. The deconvoluted spectra along with the cumulative fit and the raw data for each sample are shown in figure 3.19 (a) – (c). The deconvoluted spectra consist of three peaks, which are identified as TO, SP and LO phonon modes. Frequency, FWHM and intensity of the observed phonons are given in table 3.6. The observed TO phonon mode frequency matches with the reported bulk value [14, 55, 56]. FWHMs of the phonon modes are much larger than the FWHM of the bulk samples. This broadening of the phonon bands is a common characteristic for nanomaterials with small diameters [42]. The reduced dimension decreases the mean free path of phonons and the phonons confined in the nanocrystals frequently collide and relax at the interface, which results in shortening of the lifetime of phonons and contributes to the broadening. Lattice distortion and structural defects, which are common features of most nanocrystals also contributes to this shortening of phonon lifetime.

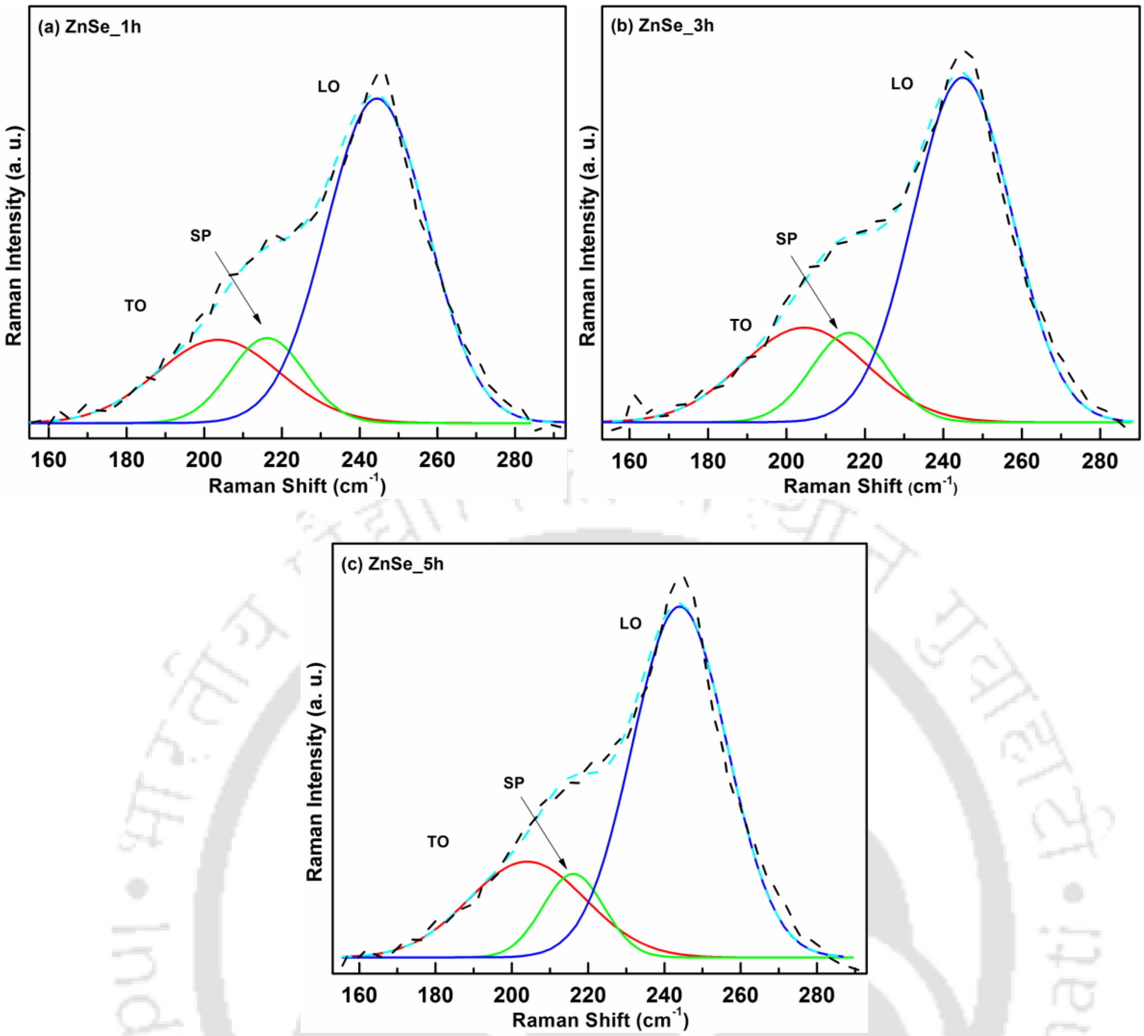

Figure 3.19: Deconvoluted Raman spectra of (a) ZnSe_1h, (b) ZnSe_3h and (c) ZnSe_5h nanocrystals.

Table 3.6: Phonon modes of ZnSe nanocrystals.

Phonon mode	**ZnSe_1h**			**ZnSe_3h**			**ZnSe_5h**		
	Band center cm^{-1}	**FWHM cm^{-1}**	**Intensity**	**Band center cm^{-1}**	**FWHM cm^{-1}**	**Intensity**	**Band center cm^{-1}**	**FWHM cm^{-1}**	**Intensity**
$\mathbf{TO}_{\mathbf{ZnSe}}$	204	37	213	204	38	417	204	36	291
$\mathbf{SP}_{\mathbf{ZnSe}}$	216	23	217	216	23	394	216	19	254
$\mathbf{LO}_{\mathbf{ZnSe}}$	244	31	829	245	29	1519	244	29	1068

3.2 Summary

CdSe and ZnSe nanostructured compounds are successfully synthesized by solvothermal process. The samples are synthesized for three different reaction time, 1h, 3h and 5h. In the synthesis of both CdSe and ZnSe nanocrystals, the solvothermal reactions leading to the nanocrystal growth take place under the same set of experimental conditions with same solvents. But, the resulting CdSe nanocrystals are wurtzite structure with rod shaped morphology whereas ZnSe nanocrystals are zinc blende structure with spherical shaped morphology. The crystallinity, compositional stoichiometry and particle size improve with reaction time. Both the nanostructured compounds possess good thermal stability. The thermal decomposition kinetics in both the compounds follow geometrical contraction model, which describes a system in which thermal decomposition occurs rapidly from the surface and the rate at which decomposition takes place controlled by the resulting interface progress toward the center of the crystal. Absorbance and photoluminescence study show the evidence of confinement effect by the presence of lattice strain in these nanostructures.

3.3 References

[1] M.O. Manasreh, Optoelectronic Properties of Semiconductors and Superlattices, Taylor & Francis Inc., New York, 2002.

[2] Z. Ning, H. Tian, C. Yuan, Y. Fu, H. Qin, L. Sun, H. Agren, Solar cells sensitized with type-II ZnSe-CdS core/shell colloidal quantum dots, Chemical Communications, 47 (2011) 1536-1538.

[3] J. Xu, X. Yang, Q.D. Yang, T.L. Wong, S.T. Lee, W.J. Zhang, C.S. Lee, Arrays of CdSe sensitized ZnO/ZnSe nanocables for efficient solar cells with high open-circuit voltage, J Mater Chem, 22 (2012) 13374-13379.

[4] P.K. Nair, M.T.S. Nair, V.M. García, O.L. Arenas, A.C.Y. Peña, I.T. Ayala, O. Gomezdaza, A. Sánchez, J. Campos, H. Hu, R. Suárez, M.E. Rincón, Semiconductor thin films by chemical bath deposition for solar energy related applications, Solar Energy Materials and Solar Cells, 52 (1998) 313-344.

[5] P.J. Sebastian, V. Sivaramakrishnan, CdSe thin films as solar control coatings, Solar Energy Materials and Solar Cells, 27 (1992) 321-326.

[6] E. Bormashenko, R. Pogreb, A. Sheshnev, S. Sutovski, Y. Bormashenko, Z. Pogreb, A. Katzir, Development of the technology of contacting ZnSe infrared optical windows using polyethylene films, Opt Eng, 40 (2001) 1754-1755.

[7] H. Wenisch, M. Fehrer, M. Klude, K. Ohkawa, D. Hommel, Internal photoluminescence in ZnSe homoepitaxy and application in blue-green-orange mixed-color light-emitting diodes, Journal of Crystal Growth, 214 (2000) 1075-1079.

[8] M.W. Cho, J.H. Chang, H. Wenisch, H. Makino, T. Yao, Blue-green light emitting diodes with new p-contact layers: ZnSe/BeTe, Phys Status Solidi A, 180 (2000) 217-223.

[9] H.S. Chen, H. Cheng-Kuo, H.-Y. Hong, InGaN-CdSe-ZnSe quantum dots white LEDs, Ieee Photonic Tech L, 18 (2006) 193-195.

[10] D.D. Wu, Z. Chen, G.B. Huang, X.G. Liu, ZnSe quantum dots based fluorescence sensors for Cu^{2+} ions, Sensors and Actuators A: Physical, 205 (2014) 72-78.

[11] J. Capon, J. Debaets, I. Derycke, H. Desmet, J. Doutreloigne, A. Vancalster, J. Vanfleteren, CdSe-Based Thin-Film Integrated Optical Sensors, Sensors and Actuators A: Physical, 32 (1992) 437-441.

[12] W.U. Huynh, J.J. Dittmer, A.P. Alivisatos, Hybrid Nanorod-Polymer Solar Cells, Science, 295 (2002) 2425-2427.

[13] A.K. Sharma, B.D. Gupta, Metal–semiconductor nanocomposite layer based optical fibre surface plasmon resonance sensor, Journal of Optics A: Pure and Applied Optics, 9 (2007) 180.

[14] S. Adachi, Handbook on Physical Properties of Semiconductors, Kluwer Academic Publishers, New York, 2004.

[15] G.K. Williamson, W.H. Hall, X-ray line broadening from filed Aluminium and Wolfram, Acta Metallurgica, 1 (1953) 22 - 31.

[16] T. Alhawi, M. Rehan, D. York, X. Lai, Synthesis of Zinc Carbonate Hydroxide Nanoparticles Using Microemulsion Process, Procedia Engineering, 102 (2015) 346-355.

[17] M.M. Ba-Abbad, A.A.H. Kadhum, A.B. Mohamad, M.S. Takriff, K. Sopian, Synthesis and catalytic activity of TiO_2 nanoparticles for photochemical oxidation of concentrated chlorophenols under direct solar radiation, Int. J. Electrochem. Sci, 7 (2012) 4871 - 4888.

[18] G.S. Paul, P. Gogoi, P. Agarwal, Structural and stability studies of CdS and SnS nanostructures synthesized by various routes, Journal of Non-Crystalline Solids, 354 (2008) 2195-2199.

[19] C. Liu, T. Wang, G. Zha, Z. Gu, W. Jie, $ZnCl_2$-assisted Synthesis of ZnSe Polycrystal, Journal of Materials Science & Technology, 28 (2012) 373-378.

[20] A.W. Coats, J.P. Redfern, Kinetic Parameters from Thermogravimetric Data, Nature, 201 (1964) 68-69.

[21] V. Šatava, Mechanism and kinetics from non-isothermal TG traces, Thermochimica Acta, 2 (1971) 423-428.

[22] A. Khawam, D.R. Flanagan, Solid-State Kinetic Models: Basics and Mathematical Fundamentals, The Journal of Physical Chemistry B, 110 (2006) 17315-17328.

[23] M. Fathollahi, S.M. Pourmortazavi, S.G. Hosseini, Particle Size Effects on Thermal Decomposition of Energetic Material, Journal of Energetic Materials, 26 (2007) 52-69.

[24] R. Liu, T. Zhang, L. Yang, Z. Zhou, Effect of particle size on thermal decomposition of alkali metal picrates, Thermochimica Acta, 583 (2014) 78-85.

[25] M.R. Sovizi, S.S. Hajimirsadeghi, B. Naderizadeh, Effect of particle size on thermal decomposition of nitrocellulose, Journal of Hazardous Materials, 168 (2009) 1134-1139.

[26] R.W. Meulenberg, J.R.I. Lee, A. Wolcott, J.Z. Zhang, L.J. Terminello, T. van Buuren, Determination of the Exciton Binding Energy in CdSe Quantum Dots, ACS Nano, 3 (2009) 325-330.

[27] E.O. Chukwuocha, M.C. Onyeaju, T.S.T. Harry, Theoretical Studies on the Effect of Confinement on Quantum Dots Using the Brus Equation, World Journal of Condensed Matter Physics, 2 (2012) 96-100.

[28] S. Suresh, Semiconductor Nanomaterials, Methods and Applications: A Review, Nanoscience and Nanotechnology, 3 (2013) 62-74.

[29] A. Thean, J.P. Leburton, Strain effect in large silicon nanocrystal quantum dots, Applied Physics Letters, 79 (2001) 1030-1032.

[30] A. Mughal, J.K. El Demellawi, S. Chaieb, Band-gap engineering by molecular mechanical strain-induced giant tuning of the luminescence in colloidal amorphous porous silicon nanostructures, Physical Chemistry Chemical Physics, 16 (2014) 25273-25279.

[31] C. Phadnis, K.G. Sonawane, A. Hazarika, S. Mahamuni, Strain-Induced Hierarchy of Energy Levels in CdS/ZnS Nanocrystals, The Journal of Physical Chemistry C, 119 (2015) 24165-24173.

[32] O. Demichel, V. Calvo, P. Noé, B. Salem, P.F. Fazzini, N. Pauc, F. Oehler, P. Gentile, N. Magnea, Quantum confinement effects and strain-induced band-gap energy shifts in core-shell Si-SiO_2 nanowires, Physical Review B, 83 (2011) 245443.

[33] J. Jasieniak, P. Mulvaney, From Cd-rich to Se-rich - The manipulation of CdSe nanocrystal surface stoichiometry, J Am Chem Soc, 129 (2007) 2841-2848.

[34] L.L. Peng, Y.H. Wang, Q.Z. Dong, Z.F. Wang, Passivated ZnSe nanocrystals prepared by hydrothermal methods and their optical properties, Nano-Micro Lett, 2 (2010) 190-196.

[35] W. Kim, S.J. Lim, S. Jung, S.K. Shin, Binary Amine-Phosphine Passivation of Surface Traps on CdSe Nanocrystals, J Phys Chem C, 114 (2010) 1539-1546.

[36] C.B. Huang, C.L. Wu, S.Y. Li, J.P. Lai, Y.B. Zhao, Quantitative model for the surface-related electron transfer in CdS quantum dots, Chem Res Chinese U, 25 (2009) 17-24.

[37] V. Higgs, F. Chin, X. Wang, J. Mosalski, R. Beanland, Photoluminescence characterization of defects in Si and SiGe structures, Journal of Physics: Condensed Matter, 12 (2000) 10105.

[38] M. Albrecht, J.L. Weyher, B. Lucznik, I. Grzegory, S. Porowski, Nonradiative recombination at threading dislocations in n-type GaN: Studied by cathodoluminescence and defect selective etching, Applied Physics Letters, 92 (2008) 231909.

[39] A. Tanaka, S. Onari, T. Arai, One phonon Raman scattering of CdS microcrystals embedded in a germanium dioxide glass matrix, Journal of the Physical Society of Japan, 61 (1992) 4222-4228.

[40] I.H. Campbell, P.M. Fauchet, The effects of microcrystal size and shape on the one phonon Raman spectra of crystalline semiconductors, Solid State Communications, 58 (1986) 739-741.

[41] F. Widulle, S. Kramp, N.M. Pyka, A. Gobel, T. Ruf, A. Debernardi, R. Lauck, M. Cardona, The phonon dispersion of wurtzite CdSe, Physica B, 263 (1999) 448-451.

[42] Y.T. Nien, B. Zaman, J. Ouyang, I.G. Chen, C.S. Hwang, K. Yu, Raman scattering for the size of CdSe and CdS nanocrystals and comparison with other techniques, Materials Letters, 62 (2008) 4522-4524.

[43] J.J. Shiang, S.H. Risbud, A.P. Alivisatos, Resonance Raman studies of the ground and lowest electronic excited-state in CdS nanocrystals, J Chem Phys, 98 (1993) 8432-8442.

[44] V. Sivasubramanian, A.K. Arora, M. Premila, C.S. Sundar, V.S. Sastry, Optical properties of CdS nanoparticles upon annealing, Physica E, 31 (2006) 93-98.

[45] S. Schmittrink, D.A.B. Miller, D.S. Chemla, Theory of the Linear and Nonlinear Optical-Properties of Semiconductor Microcrystallites, Physical Review B, 35 (1987) 8113-8125.

[46] H. Wang, Z. Guo, F. Du, Solvothermal synthesis of CdSe nanorods via DEA solution, Materials Chemistry and Physics, 98 (2006) 422-424.

[47] J. Yang, C. Xue, S.H. Yu, J.H. Zeng, Y.T. Qian, General synthesis of semiconductor chalcogenide nanorods by using the monodentate ligand n-butylamine as a shape controller, Angew Chem Int Edit, 41 (2002) 4697-4700.

[48] Y. Duan, S. Yao, C. Dai, X. Liu, G. Xu, Characterization of ZnSe microspheres synthesized under different hydrothermal conditions, Transactions of Nonferrous Metals Society of China, 24 (2014) 2588-2597.

[49] J. Marquina, C. Power, J. Gonz´alez, Raman scattering on ZnO nanocrystals, Revista Mexicana De Fisica S53 (2007) 170 - 173.

[50] M.J. Seong, O.I. Mićić, A.J. Nozik, A. Mascarenhas, H.M. Cheong, Size-dependent Raman study of InP quantum dots, Applied Physics Letters, 82 (2003) 185-187.

[51] J.J. Shiang, R.H. Wolters, J.R. Heath, Theory of size-dependent resonance Raman intensities in InP nanocrystals, The Journal of Chemical Physics, 106 (1997) 8981-8994.

[52] B. Hennion, F. Moussa, G. Pepy, K. Kunc, Normal modes of vibrations in ZnSe, Physics Letters A, 36 (1971) 376-378.

[53] R.K. Ram, S.S. Kushwaha, A. Shukla, Phonon assignments in II-VI and III-V semiconductor compounds having zincblende-type structure, Physica Status Solidi (b), 154 (1989) 553-564.

[54] H.Z. An, Q. Zhao, W.M. Du, Raman spectra of ZnSe nanoparticles synthesized by thermal evaporation method, Chinese Physics, 13 (2004) 1753-1757.

[55] D. Huang, C. Jin, D. Wang, X. Liu, J. Wang, X. Wang, Crystal structure and Raman scattering in $Zn_{1-x}Mg_xSe$ alloys, Applied Physics Letters, 67 (1995) 3611-3613.

[56] M. Kozielski, M. Szybowicz, F. Firszt, S. Legowski, H. Meczynska, J. Szatkowski, W. Paszkowicz, Study of the $A_{1-x}B_xC$ mixed crystals by Raman scattering, Cryst Res Technol, 34 (1999) 699-702.

Chapter 4

Growth and studies of CdS_xSe_{1-x} ternary alloy thin films

In this chapter, growth, structural and optical properties of CdS_xSe_{1-x} ternary alloy thin films as deposited by thermal evaporation of solvothermally synthesized CdS-CdSe composite powders are discussed. CdS_xSe_{1-x} ternary alloy semiconductor is one of the most important II-VI semiconductors with promising applications in various optoelectronic devices including photoelectrochemical hydrogen generation [1], tunable laser [2, 3], optical waveguides [4-7], sensors [8], solar cells [9], etc., mainly due to its wide-ranged tunable direct band gap which spans from visible ($\sim 2.42\,eV$ for CdS) to near IR ($\sim 1.68\,eV$ for CdSe)[10, 11]. The tunable property in this material can be achieved by altering the relative concentration of the anions, S and Se in the alloy, which can be done by using most of the existing thin film preparation techniques such as laser ablation [12-15], mechanical alloying [16], chemical bath deposition [17], etc. Besides being technologically important, it also possesses interesting optical and vibrational behavior. Spin orbit (SO) coupling effect in the optical spectra and two-phonon mode vibrational behavior in these alloys are interesting properties of these compounds, which may have certain implications in the performance of the material when used in optoelectronic devices. However, very few reports are available on the investigation of these two phenomena in CdS_xSe_{1-x}. The reported experimental work is mostly limited to nanocrystallites of these compounds dispersed in glass matrix [18] and sometimes on nanocrystals having nearly equal concentration of S and Se atoms in CdS_xSe_{1-x} alloys [14]. With these motivations, we prepare CdS_xSe_{1-x} ternary alloy thin films by varying the relative composition of CdS and CdSe in the composite powders. The structural, optical and vibrational properties of the films were investigated by X-ray diffraction (XRD), UV-Vis-NIR transmission and Raman scattering spectroscopy. We will discuss the changes in structural, optical and vibrational properties of the films with compositional variation in the following sections.

4.1 Results and discussion

4.1.1 EDX and XRD of the precursor CdS-CdSe composite powders`

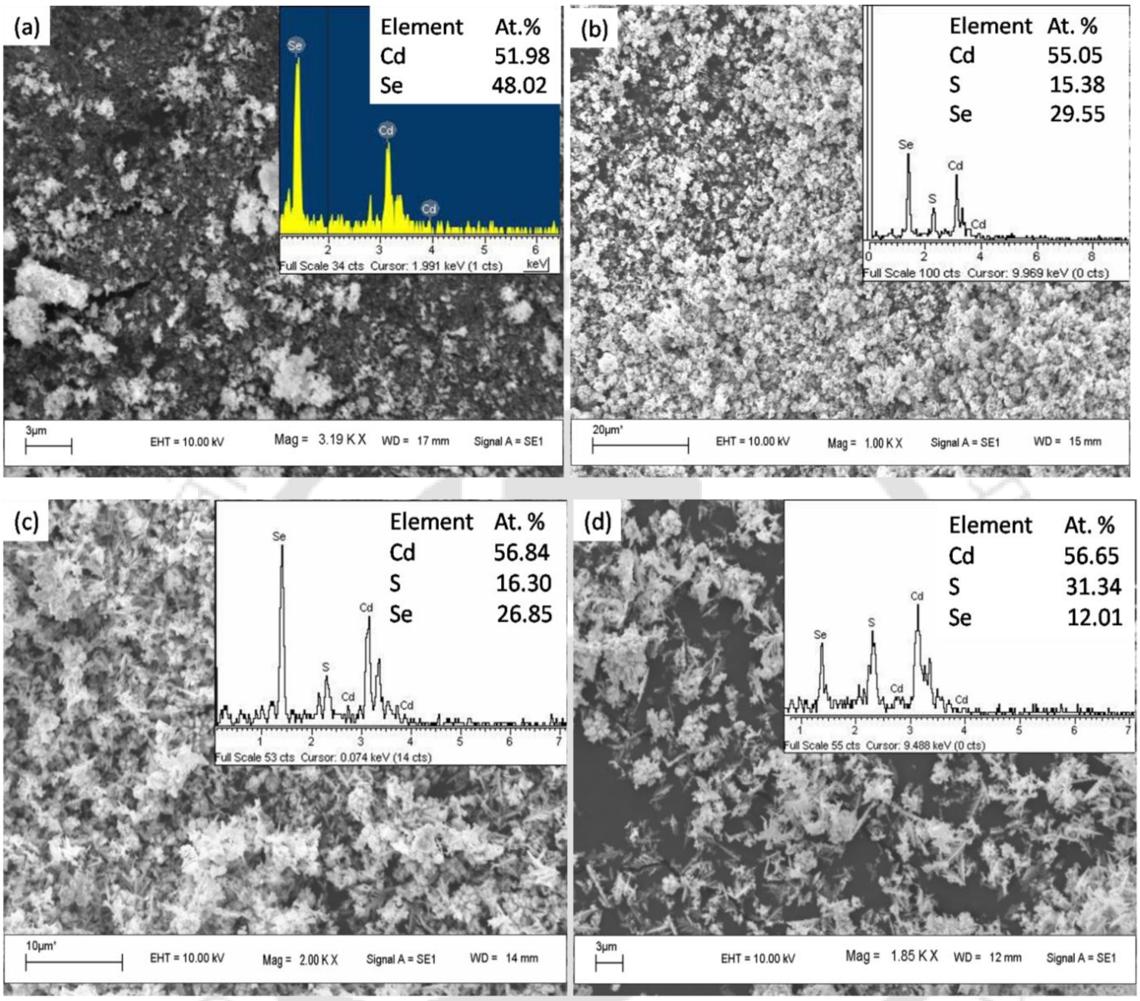

Figure 4.1: SEM images and EDX spectra of the synthesized binary and composite powders.

Figure 4.1 (a) - (d) shows the SEM images and the corresponding EDX spectra of the synthesized CdS-CdSe composite powders. The composition, as shown in the figures, are an average of the measurements taken over 2-3 different positions in the SEM images. As indicated in the EDX spectra, the synthesized powders are without any significant impurity and consist only of cadmium, sulfur and selenium. The three composite powder samples contain different amount of sulfur and selenium, which are uniformly mixed over the entire samples. Figure 4.2 (a) and (b) show the XRD patterns of two of the synthesized composite powders. The observed peaks correspond to the hexagonal planes of both CdSe and CdS indicating the composite nature of the synthesized powders.

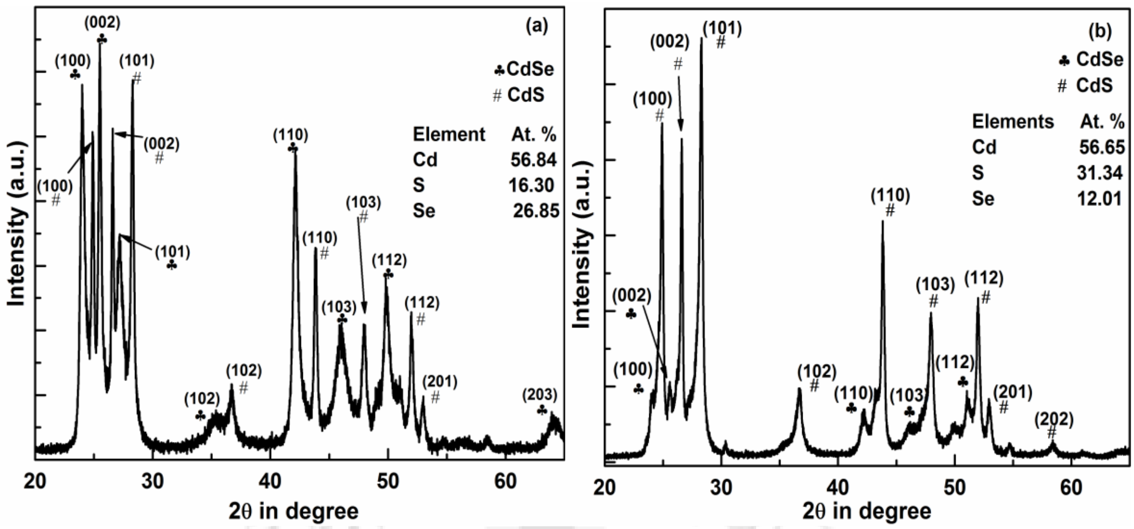

Figure 4.2: XRD pattern of two of the composite powders showing diffraction planes from both CdS and CdSe.

4.1.2 Composition and surface morphology studies of CdS_xSe_{1-x} thin films

Figure 4.3 (a) - (e) shows the EDX spectra of the films. The atomic percentage of different ions shown in this case are average over 3 - 4 measurements at different location on the films. All the films appear to be slightly Cd rich. The fraction of sulfur content (*x*) in the films is obtained by normalizing the total atomic percentage of anion content in the films. The standard deviation in composition is calculated for each of the ternary alloys. $CdS_{0.17}Se_{0.83}$ sample, in particular have relatively large standard error of about 0.05 in comparison to the errors of about 0.02 for the remaining ternary samples. It is observed here that the films do not maintain the same composition as that of the source nano-composite powders used for the preparation of the films. The S content in the films is slightly less than that in the source composite powders due to relatively low vapour pressure of CdS as compared to that of CdSe [19].

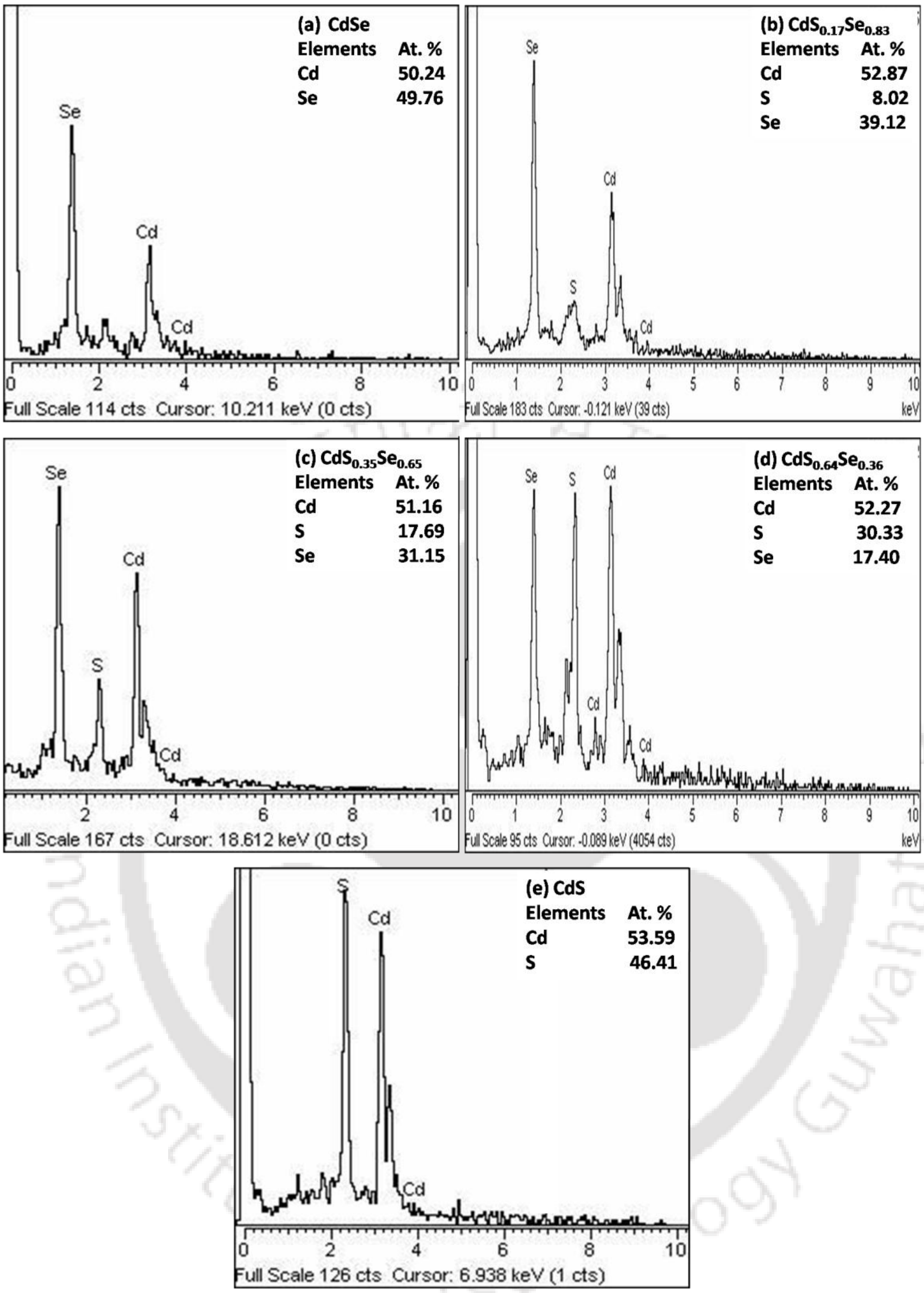

Figure 4.3: EDX spectra of CdS_xSe_{1-x} (x =0, 0.17, 0.35, 0.64, 1) thin films.

Figure 4.4 show FESEM images of the films. The films are deposited uniformly throughout the surface. While the CdS film mostly consist of almost spherical shaped grains, the ternary alloy films containing selenium have bigger irregular shaped grains. With the exception of $CdS_{0.35}Se_{0.65}$ sample, the grain size increases with increase in selenium content and the pure CdSe film possess surface consisting mostly of nanodimensional flakes. Though the reason for reduced grain size in $CdS_{0.35}Se_{0.65}$ sample is not very clear, this could be due to some variation in substrate temperature during deposition.

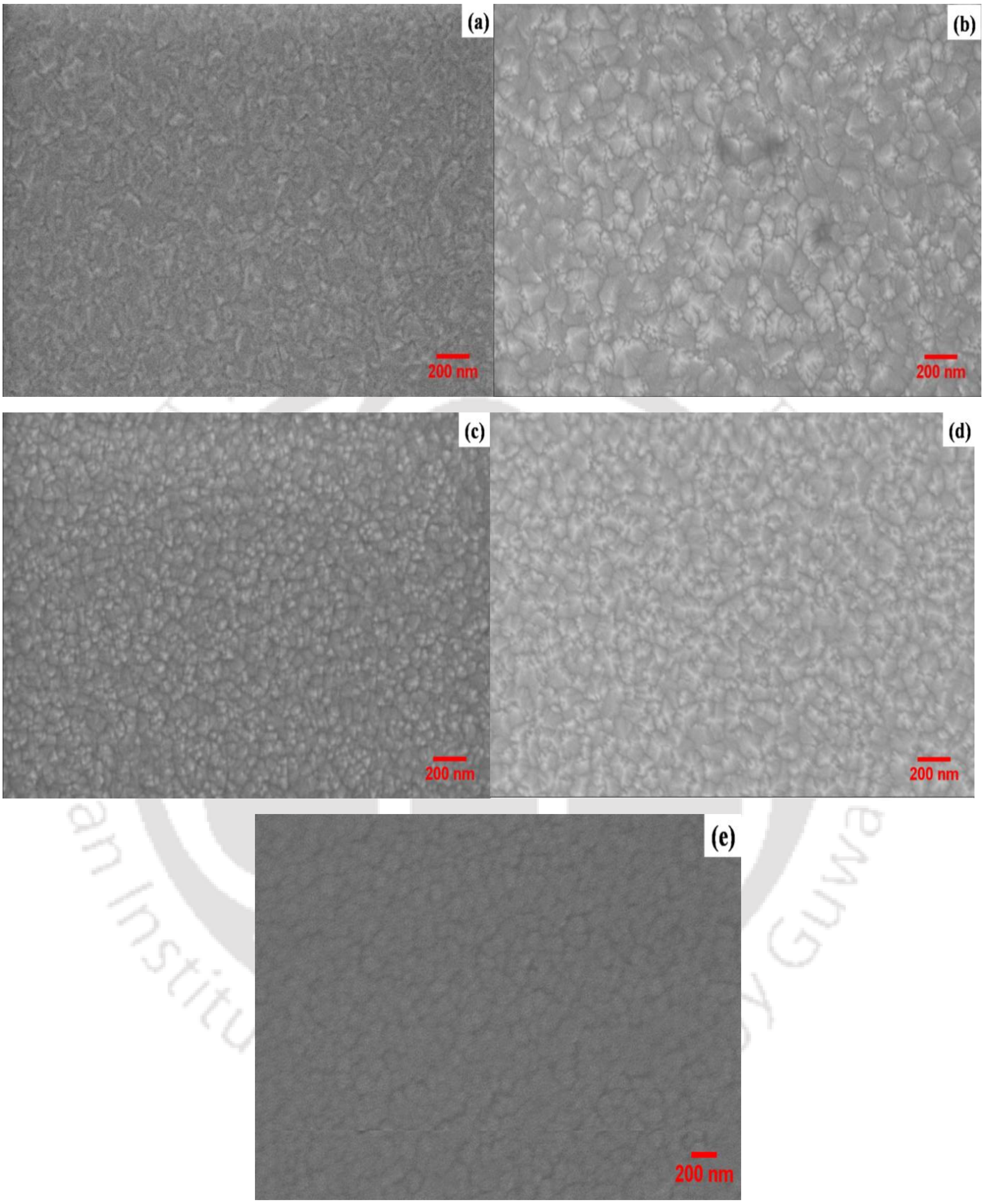

Figure 4.4: FESEM images of (a) CdSe, (b) $CdS_{0.17}Se_{0.83}$, (c) $CdS_{0.35}Se_{0.65}$, (d) $CdS_{0.64}Se_{0.36}$ and (e) CdS thin films.

4.1.3 XRD studies

Figure 4.5 (a) shows the XRD patterns of CdS$_x$Se$_{1-x}$ thin films (x =0, 0.17, 0.35, 0.64, 1). XRD patterns of CdS$_x$Se$_{1-x}$ thin film samples (x = 0, 0.17, 0.35, 0.64, 1) are shown in figure 5(a). All films show a sharp distinct peak with its 2θ value shifting from 25.440° in CdSe (x = 0) to 26.526° in CdS (x = 1) as listed in table 4.1. Direction of the peak shifting follows compositional changes, i.e., 2θ increases as fraction of sulfur increases. According to standard JCPDS data, the observed 2θ values of the end binary compounds are very close to the respective values of both (111) plane of zinc-blende structure and (002) plane of wurtzite structure of the compounds. The 2θ values of (002) plane of bulk wurtzite CdSe and CdS are found at 25.391° [PDF # 772307] and 26.660° [PDF # 800006] respectively. Whereas, the 2θ values of (111) plane of bulk zinc-blende CdSe and CdS are observed at 25.375° [PDF #190191] and 26.547° [PDF #800019] respectively. Therefore, the strong diffraction peak observed in our samples could correspond to any of the two crystal planes mentioned above. However, since the optical band gap of the end binary alloys, as obtained from UV-Vis-NIR transmission measurements (discussed later), are closer to the values for zinc blende structure [10], we believe that the films possess a zinc blende structure rather than the wurtzite structure of the source nano-composite powders. In addition to this strong diffraction peak, very weak diffraction peak around 2θ value of 46° is also observed which could be due to (103) plane of the wurtzite phase of the source compounds, traces of which is likely to be present in the films.

Lattice constant, lattice strain, dislocation densities and average crystallite sizes estimated from the XRD are listed in table 4.1. The lattice constant a decreases from 6.059Å to 5.816 Å as x increases from 0 to 1. This variation follows linear Vegard's relation for ternary alloys, i.e., $a_{CdS_xSe_{1-x}} = (1-x)a_{CdSe} + xa_{CdS}$ as shown in figure 4.1 (b). The crystallite size of films varies from 24 nm to 39.7 nm. These may be slightly underestimated as it is not possible to isolate the size and strain broadening of diffraction peaks for thin films where usually only single diffraction peak is observed [20].

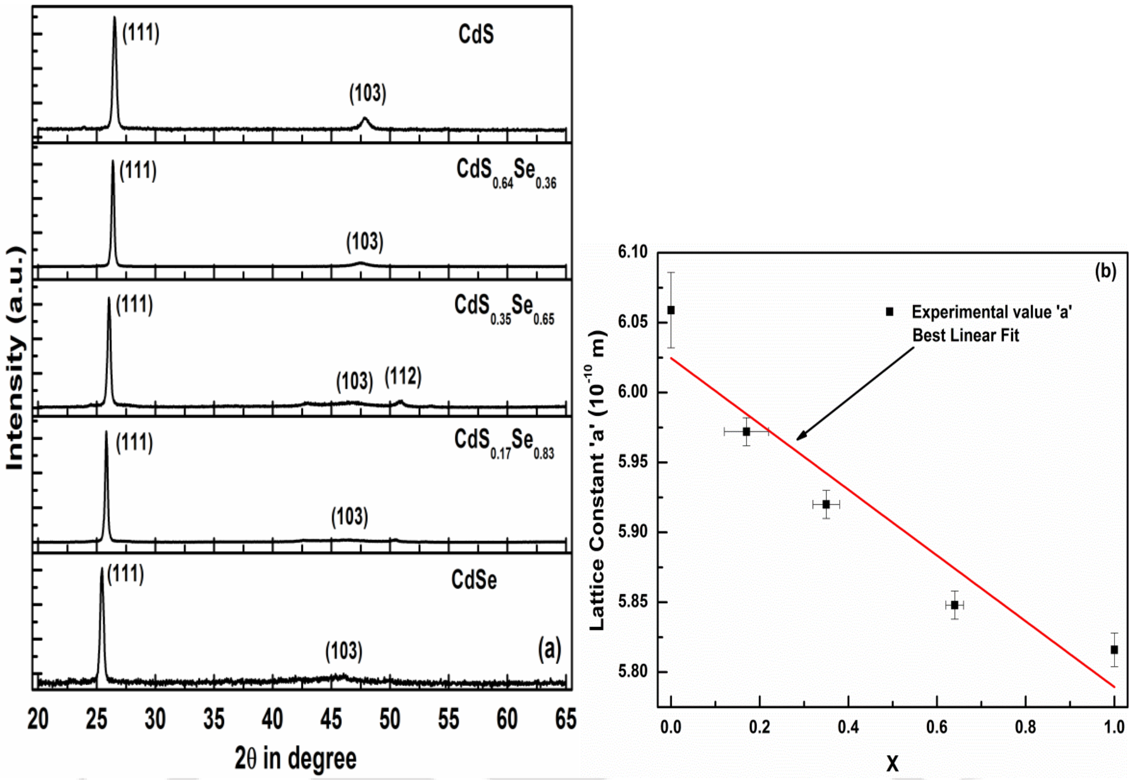

Figure 4.5: (a) XRD pattens of CdS$_x$Se$_{1-x}$ thin films (x = 0, 0.17, 0.35, 0.64, 1), (b) Plot of lattice constant (*a*) vs sulfur content (*x*).

Table 4.1: Structural parameters of CdS$_x$Se$_{1-x}$ thin films.

Sample	2θ (degree)	β (FWHM) (degree)	Lattice constant ‘a’ (Å)	Lattice strain (× 10^{-3})	Dislocation density (lines/m^2) (× 10^{15})	Average crystallite size(nm)
CdSe	25.440	0.288	6.059±0.027	1.23	1.15	29.5±0.3
CdS$_{0.17}$Se$_{0.83}$	25.823	0.215	5.972±0.010	0.91	0.64	39.6±0.2
CdS$_{0.35}$Se$_{0.65}$	26.051	0.254	5.920±0.010	1.08	0.89	33.6±0.1
CdS$_{0.64}$Se$_{0.36}$	26.379	0.215	5.848±0.010	0.91	0.64	39.7±0.2
CdS	26.526	0.356	5.816±0.012	1.51	1.74	24.0±0.1

4.1.4 UV-Vis-NIR studies

Figure 4.6(a) shows the UV-Vis-NIR transmission spectra of the thin films in the wavelength range 220 - 2500 nm at normal incidence. All the films show good interference pattern in the NIR region with maximum transmittance of about 90 %. The optical absorption edge as indicated by sharp drop in the transmittance spectra shifted towards shorter wavelength with increasing *x*.

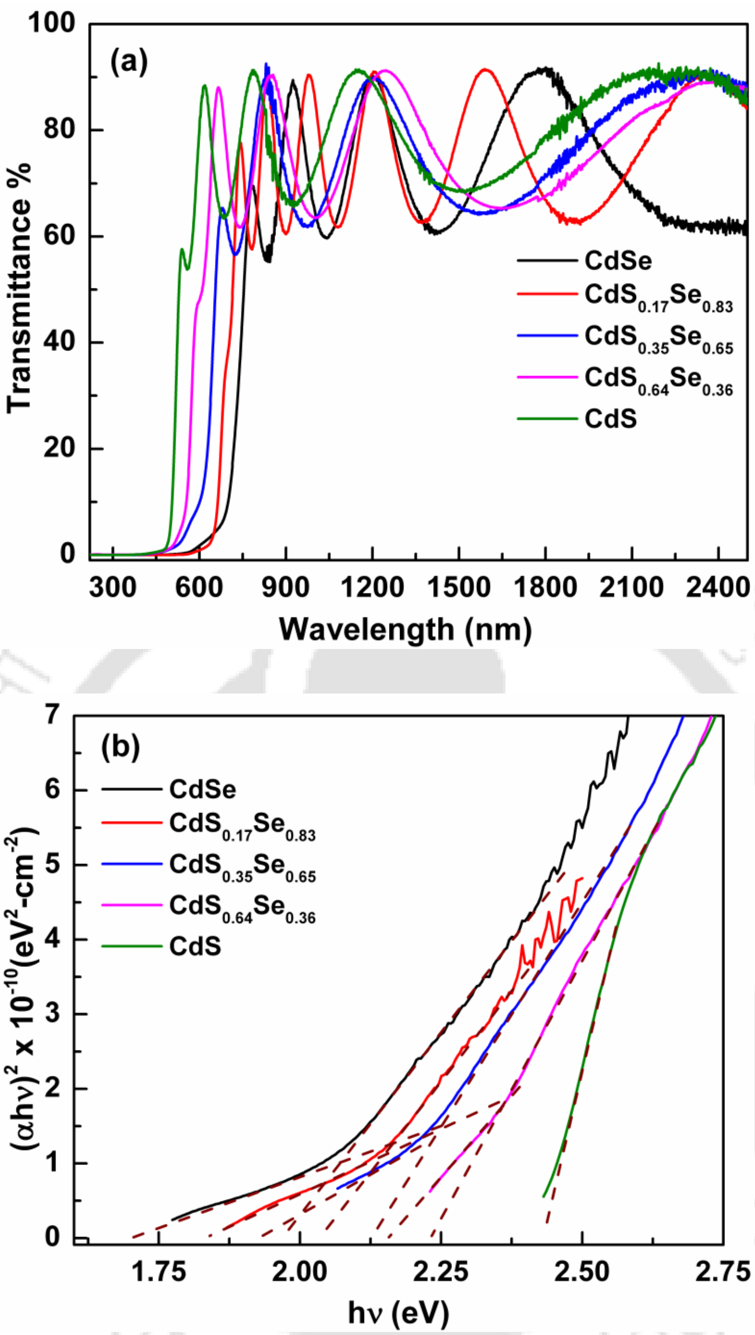

Figure 4.6: (a) UV-Vis-NIR transmission spectra of CdS_xSe_{1-x} thin films (x = 0, 0.17, 0.35, 0.64, 1), (b) $(\alpha h\nu)^2$ *vs* $h\nu$ plot.

Refractive index (n), absorption coefficient (α) and thickness of the films are determined using the method described by Swanepoel [21]. These quantities are given in table 4. 2. The refractive index value at 550 nm depends on the fraction of sulfur in the films; decreasing as the sulfur content increases. The values obtained for the end binary compounds, i.e., CdS and CdSe are comparable with those reported in literature [22-24].

Table 4.2: Band gap, refractive index and film thickness of CdS_xSe_{1-x} alloy thin films.

Sample	Film thickness (nm)	n (550nm)	E_{g1}(eV) $(\Gamma_8^v \rightarrow \Gamma_6^c)$	E_{g2}(eV) $(\Gamma_7^v \rightarrow \Gamma_6^c)$	SO splitting (eV)
CdSe	766	2.86	1.67 ± 0.02	1.97 ± 0.02	0.30 ± 0.02
$CdS_{0.17}Se_{0.83}$	980	2.77	1.82 ± 0.02	2.03 ± 0.02	0.21 ± 0.02
$CdS_{0.35}Se_{0.65}$	513	2.69	1.90 ± 0.02	2.11 ± 0.02	0.21 ± 0.02
$CdS_{0.64}Se_{0.36}$	530	2.66	2.15 ± 0.02	2.24 ± 0.02	0.09 ± 0.02
CdS	495	2.52	2.43 ± 0.02		0

The band gaps (E_g) are obtained from $(\alpha h\nu)^2$ *vs* $h\nu$ plot as shown in figure 4.6(b). The linear dependence of $(\alpha h\nu)^2$ on $h\nu$ in the plot indicates the occurrence of direct optical transition as expected in these semiconductors. The bandgap corresponding to each direct optical transition is obtained by fitting a straight line as shown in the figures. The values obtained from these fittings are given in table 4.2. The two optical transitions as deduced from the plot in all the samples containing selenium atoms correspond to direct transitions $(\Gamma_8^v \rightarrow \Gamma_6^c)$and $(\Gamma_7^v \rightarrow \Gamma_6^c)$ as have been reported for zinc-blende structure of binary compounds including ZnSe and CdSe [25-29]. These transitions are due to SO splitting of the valence band caused by the large ionic radii of Se atoms. For pure CdS films, only one direct optical transition is observed indicating the absence of any spin orbit splitting in the valence band of these films. The absence of SO splitting in CdS is due to the small ionic radii of S atoms. The magnetic field generated by orbiting electron in this case is too weak to induce any coupling with electron spin. The SO splitting energies in samples containing Se atom are calculated from the difference of the observed two band gaps. The observed SO splitting in CdSe is comparable with reported values [10, 30, 31]. The calculated SO splitting energy is a function of sulfur content in the samples, decreasing as the sulfur content increases as shown in figure 4.7 (a). Increase in sulfur (S) content in the alloy corresponds to decrease in selenium (Se) concentration in the lattice, the heavier atom which is responsible for SO splitting. The calculated band gap for the end binary compounds i.e., CdSe (1.67 eV) and CdS (2.43 eV) are comparable to the reported band gaps for zinc blende structure of the corresponding compounds; 1.68 eV and 2.42 eV for CdSe and CdS respectively [10, 11].

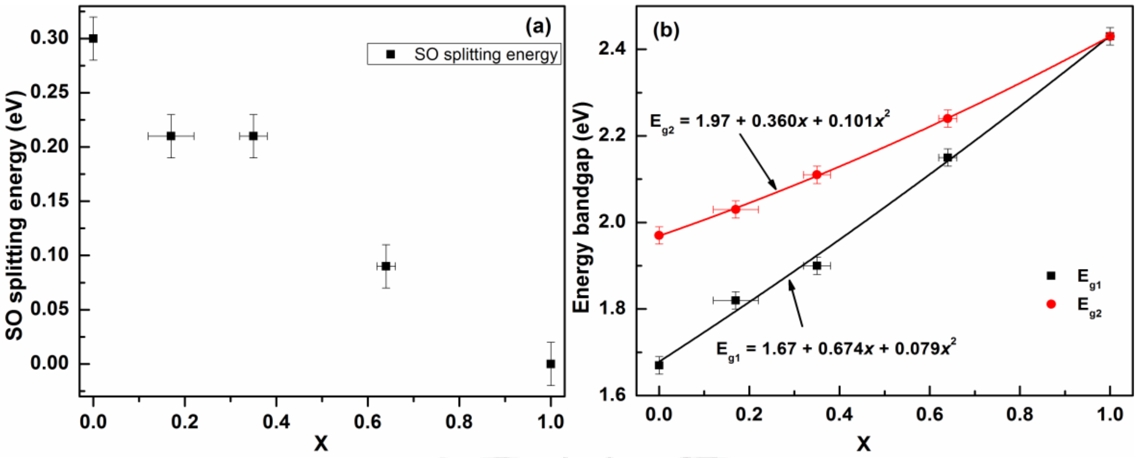

Figure 4.7: (a) Plot of SO splitting energy vs fraction of sulfur (*x*), (b) Plot of energy bandgap vs fraction of sulfur (*x*).

Figure 4.7 (b) shows the band gap variation with composition along with the second order polynomial fitting. This deviation from linear relation is a commonly observed phenomena in ternary alloy thin films and is mainly due to the difference in the lattice constants as atoms are substituted by another atoms in the alloying [32, 33]. The bowing parameters *b* in our samples are 0.079 and 0.101 eV respectively for E_{g1} and E_{g2}, which are lower than the reported value of 0.53 eV [10, 11].

4.1.5 Raman scattering studies

Room temperature Raman spectra of CdS_xSe_{1-x} (x = 0, 0.17, 0.35, 0.64, 1) thin films are shown in figure 4.8. CdSe thin film has distinct vibrational bands corresponding to TO_{CdSe}, LO_{CdSe} and $2LO_{CdSe}$ phonons. The spectra of all the ternary samples exhibit prominent Raman bands corresponding to both CdSe and CdS-like phonons as predicted by modified random element isodisplacement model (MREI) [34]. With the increase in fraction of sulfur in the film, intensity of CdS-like phonon modes is observed to increase while intensity of CdSe like phonon modes decreases. Since, these phonon bands are close to the reported LO phonons of the respective binary compounds; these are identified as LO_{CdSe} and LO_{CdS} phonon modes. As clearly seen from the spectra, these phonon modes are highly asymmetric towards the lower wave number side. In addition to these first order Raman lines, higher order phonon modes identified as $2LO_{CdSe}$, $2LO_{CdS}$ and LO_{CdSe} + LO_{CdS} phonons are also observed. The binary compound CdS thin film has two Raman lines; a strong LO_{CdS} phonon mode with asymmetric broadening towards the lower wave number side and a weak higher order $2LO_{CdS}$ phonon mode as indicated in the figure. The presence of only the characteristic phonon modes in the end binary compounds further supports the EDX measurements on these films.

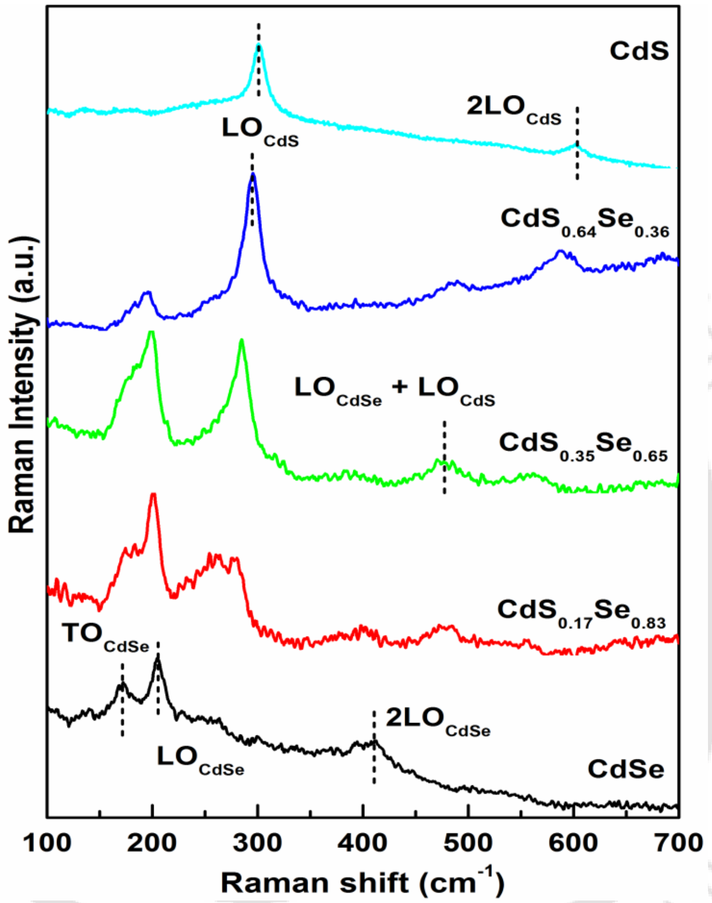

Figure 4.8: Raman spectra of CdS_xSe_{1-x} (x = 0, = 0, 0.17, 0.35, 0.64, 1) thin films.

The Raman spectra are further analyzed by deconvoluting the recorded spectra as shown in figures 4.9 (a) - (e). Since, most phonon broadenings are homogeneous; all the observed peaks in Raman Spectra are fitted with Lorentzian distribution. The black coloured dotted lines in each figures corresponds to recorded raw data in Raman spectra.

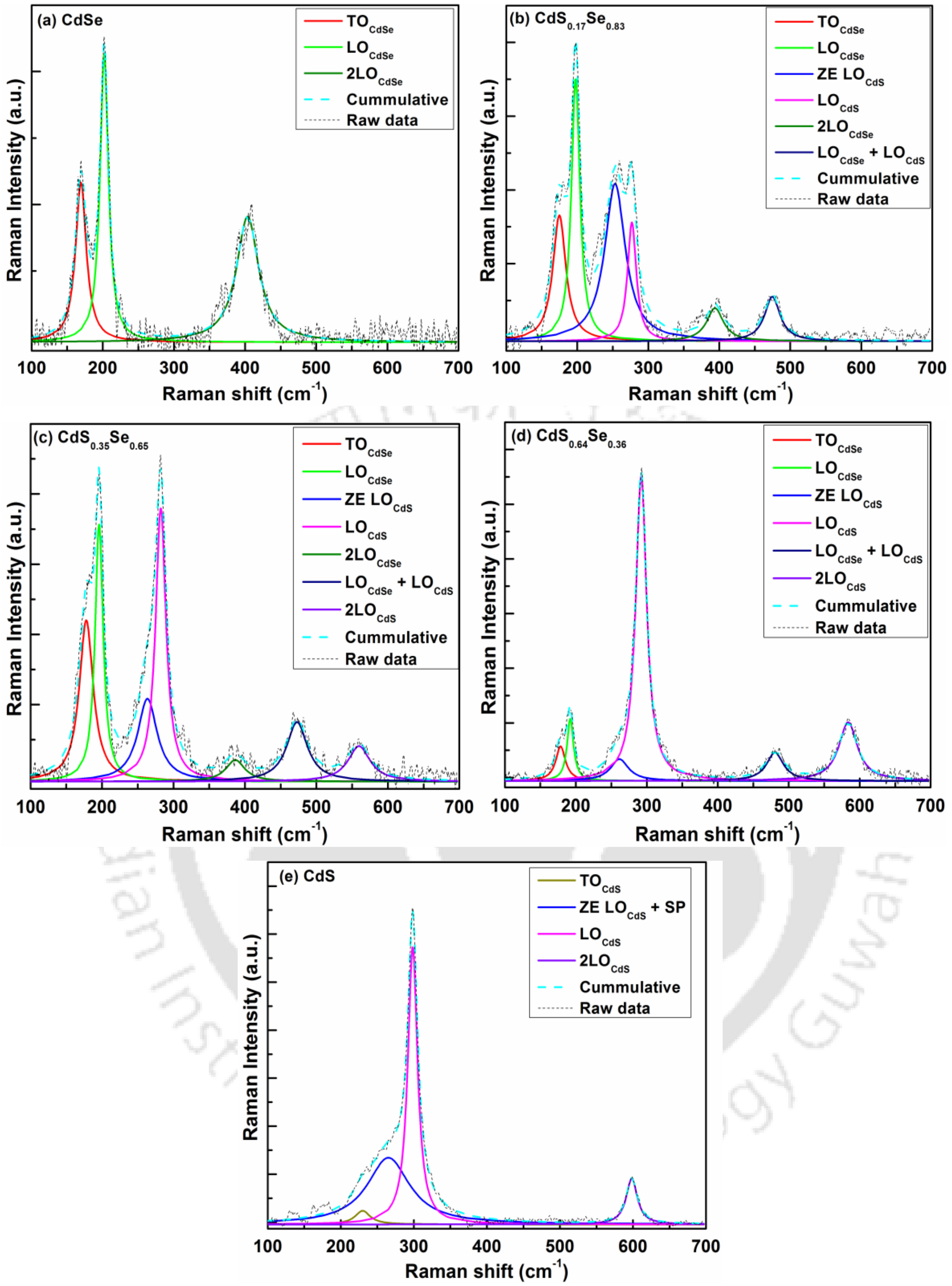

Figure 4.9: Deconvoluted Raman spectra of CdS$_x$Se$_{1-x}$ (x= 0, 0.17, 0.35, 0.64, 1) thin films.

Table 4.3: Phonon modes of CdS_xSe_{1-x} (x = 0, 0.17, 0.35, 0.64, 1) thin films.

Phonon mode	CdSe			$CdS_{0.17}Se_{0.83}$			$CdS_{0.35}Se_{0.65}$			$CdS_{0.64}Se_{0.36}$			CdS		
	Band center	FWHM (cm^{-1})	Intensity	Band center	FWHM (cm^{-1})	Intensity	Band center	FWHM (cm^{-1})	Intensity	Band center	FWHM (cm^{-1})	Intensity	Band center	FWHM (cm^{-1})	Intensity
TO_{CdSe}	169	18.3	120	175	22.2	171	178	23.7	230	179	16.6	63			
LO_{CdSe}	202	14.1	217	198	14.4	355	196	13.6	366	192	11.0	114			
TO_{CdS}													230	25.6	142
ZE LO_{CdS}				253	35.1	214	263	33.1	118	262	30.7	40	265	70.8	694
LO_{CdS}				277	14.8	161	282	17.7	389	292	18.8	557	298	16.0	2887
$2LO_{CdSe}$	404	38.0	94	394	28.8	45	387	32.7	31						
$LO_{CdS}+LO_{CdSe}$				475	26.6	60	473	35.2	85	481	28.8	52			
$2LO_{CdS}$							560	37.5	51	584	31.7	107	598	18.4	477

The cumulative fit as indicated in the figures match very well with the raw data in all the spectra. Table 4.3 shows the band center position, the full-width at half maxima (FWHM) and the intensity of all the observed phonon modes. All the phonon modes including the zone center phonons have FWHM, which is comparatively much larger than the reported bulk values for the II-VI binary compounds [35]. The LO phonon modes of both CdSe and CdS are slightly red-shifted from the reported values (LO_{CdSe} = 211 cm^{-1} [10, 36], LO_{CdS} = 305 cm^{-1} [10, 36, 37]).

The observed asymmetric broadening of LO_{CdS} mode of pure CdS was reported for CdS thin films prepared using chemical bath deposition technique [37] and was attributed to the presence of surface phonon (SP). The large asymmetric broadening in our CdS sample is best fitted with three Lorentzians as shown in figure 4.9 (e). In this fitting, small signature of TO_{CdS} mode is observed at 230 cm^{-1}, which is normally absent in most of the reported Raman measurements on CdS samples. This occurrence of small signature of TO_{CdS} mode could be due to the TO resonant scattering in our sample. The energy of the excitation photon 2.41 eV (514.5 nm) is slightly smaller than the observed band gap 2.43 eV, which satisfies the necessary resonance condition of the TO mode of CdS films [38]. Since the crystallite size in CdS sample is small, the additional phonon mode with large FWHM observed in this three Lorentzians fitting is assigned to the SP vibration and other disorder activated phonons. The presence of non-uniform strain in the crystal may also add to the large FWHM of this mode.

The asymmetric broadening as observed in CdS_xSe_{1-x} ternary alloys have been discussed by several authors [14, 18, 39]. Since, this asymmetric broadening exists even in bulk samples, the surface phonon is ruled out as the sole cause of this broadening [39]. Various models such as Fano profile model [39], special correlation model [14, 39] and two-Lorentzians model [14, 39] have been used to explain the observed phenomenon. Ingale, et al. [39], in their investigation of these three models on CdS_xSe_{1-x}showed that the two-Lorentzian model involving the disorder induced zone edge phonon best describe the asymmetry observed in these alloys. Pagliara et al. [14], also in their investigation on the effect of disorder on the Raman scattering of CdS_xSe_{1-x} films deduced that the disorder induced zone edge phonons are responsible for asymmetric broadening in CdS-like LO_{CdS} phonon modes. In the light of the previous reports, the observed first order LO Raman lines in our samples are also fitted with two Lorentzians. The second Lorentzian on the lower wave number side of LO_{CdS} mode is identified as the zone edge (ZE) LO_{CdS} phonon. The origin of this phonon can be understood from the dispersion curve of CdS [10]. In the dispersion curve of CdS, the LO_{CdS} and TO_{CdS} phonon modes are still separated at the zone boundaries forming distinct zone edge phonon vibrations, ZE-LO_{CdS} and ZE-TO_{CdS} respectively at frequencies which are slightly different from the respective zone center phonon modes. These phonon modes can become Raman active once we have significant disorder. The ZE-LO_{CdS} frequency being lower than the zone center LO_{CdS} phonon mode, results in asymmetric broadening of LO_{CdS} on the lower wave number side as observed in our samples. However, the Raman line on the lower wave number side of LO_{CdSe} is assigned to TO_{CdSe} phonon mode of CdSe. Although it is possible that the disorder activated phonons may also contribute to the observed asymmetric broadening in the LO_{CdSe} phonon, it is more likely that TO_{CdSe} will dominate as strong peak corresponding to this mode is also observed in the Raman spectra of pure binary CdSe films.

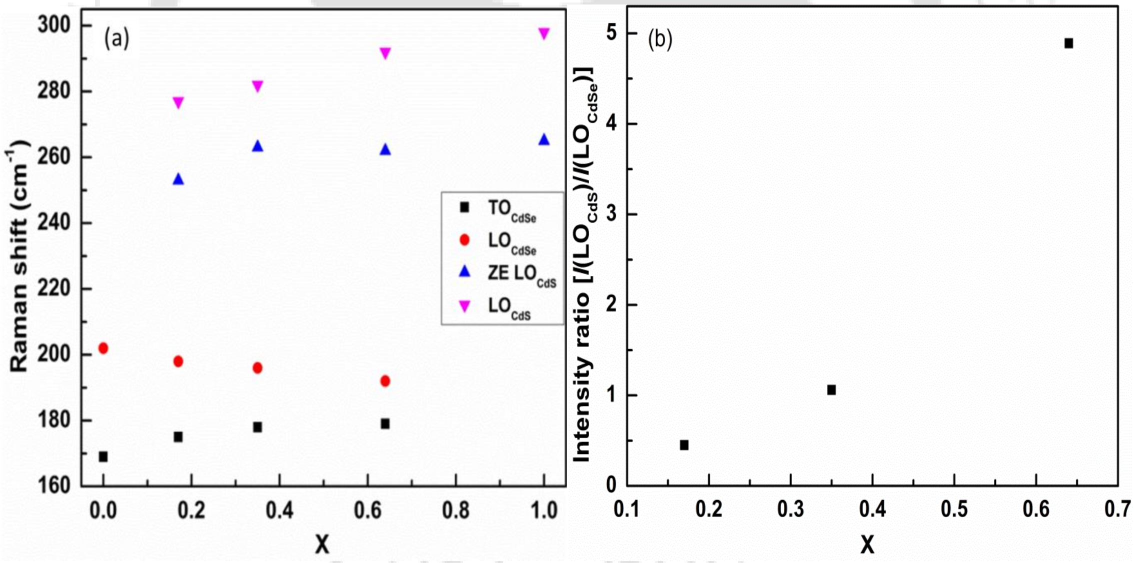

Figure 4.10: (a) Plot of Raman shift vs fraction of sulfur (x), (b).Plot of intensity ratio of the two LO phonons $\left[\frac{I(LO_{ZnS})}{I(LO_{ZnSe})}\right]$ vs fraction of sulfur (x).

Figure 4.10 (a) shows, the Raman shift of the observed first order Raman modes plotted against the sulfur content (x). The gap between TO_{CdSe} and LO_{CdSe} phonon modes, which are widely separated for pure CdSe sample, gets narrower with the increase in sulfur content. These phonon modes appear to approach a single vibrational mode known as gap mode as the fraction of selenium in the ternary alloy reduces. This observation is in agreement with the calculated concentration dependence of TO_{CdSe} and LO_{CdSe} phonon modes for CdS_xSe_{1-x} [39]. Brafman et al. [40], also reported similar observation for ZnSe-like TO and LO phonons in ZnS_xSe_{1-x} ternary alloy thin films. From the figure, the observed LO_{CdS} phonon mode frequency can also be seen to increase gradually with increase in sulfur content (x) in agreement with earlier reports [41]. The ZE LO_{CdS} phonon mode frequency, however, does not show much dependence on compositional variation. Since, the ZE phonons are activated due to lattice disorder, the FWHMs and the intensities of the phonon modes are a measure of disorder in the lattice. In the intermediate ternary alloys, the FWHM and the intensity of the ZE LO_{CdS} phonon decrease with the increase in a fraction of S atom in the alloy as shown in table 4.3. This may be due to smaller lattice disorder in our ternary systems when heavier Se is substituted with S atom. The heavier Se atom, if it forms point defects, may cause larger lattice distortion. The EDX measurements also show that the samples with more Se atoms have larger non-uniformity in composition (larger standard error) and hence larger compositional disorder. However, the seemingly large zone edge phonon observed in the pure CdS sample could be due to the presence of surface phonon (SP) contribution, which may arise due to the smaller dimension of the prepared sample.

The plot of intensity ratio of the two LO phonons $\left[\frac{I(LO_{CdS})}{I(LO_{CdSe})}\right]$ against the fraction of sulfur (x) are given in figure 4.10 (b). The plot shows that the relative strength of the zone center phonons is dependent on the fraction of sulfur as has been reported for other mixed crystals exhibiting two-mode behavior [33]. The increased intensity ratio $\left[\frac{I(LO_{CdS})}{I(LO_{CdSe})}\right]$ corresponds to the increasing number of Cd-S bond (decreasing number of Cd-Se bond) in the mixed crystal as more number of anion sites in the crystal is occupied by S atom.

4.2 Summary

Though, the preparation technique of CdS_xSe_{1-x} ($0 \leq x \leq 1$) thin films developed in this work is a bit lengthy as it involves two step processes, it, however, does not require sophisticated instruments and the starting compound is prepared using already well-established low cost processes. The thin films have uniform deposition with good crystallinity and tunable structural and optical properties. Valence band splitting due to spin orbit coupling, as reported for binary CdSe compound has also been observed in the ternary CdS_xSe_{1-x} ($0 \leq x \leq 1$) thin films. Further, we are able to show that the SO splitting is a function of Se content in the ternary alloy films, decreasing as the concentration of Se decreases. The dual phonon modes observed in our CdS_xSe_{1-x} samples follow the reports on nanocrystal doped glasses and thin films prepared using more sophisticated processes. The FWHM and the intensity of the disorder ZE phonon observed in our samples are found to decrease with Se content due to lower compositional disorder and smaller lattice distortion.

4.3 References

[1] G. Ai, R. Mo, H. Xu, Q. Chen, S. Yang, H. Li, J. Zhong, Composition-optimized TiO_2/CdS_xSe_{1-x} core/shell nanowire arrays for photoelectrochemical hydrogen generation, Journal of Applied Physics, 116 (2014) 174306.

[2] J. Bille, B.M. Kramer, P. Reimers, W. Ruppel, R. Stille, Continuously tunable laser emission by CdS_xSe_{1-x} graded band gap crystals, Physica Status Solidi (b), 36 (1969) K71 - K74.

[3] J. Bille, H. Liebing, G. Scheiber, P. Mengel, Tunable laser emission of CdS_xSe_{1-x} graded band gap crystals by two-photon excitation, Physica Status Solidi (a), 12 (1972) K91 - K93.

[4] Z.E. Buachidze, I.V. Vasilishcheva, V.N. Morozov, V.A. Pletnev, A.S. Semenov, P.V. Shapkin, Development and investigation of integrated-optics CdS_xSe_{1-x} waveguides, Kvantovaya Elektron, 12 (1985) 1814-1818.

[5] Z.E. Buachidze, I.V. Vasilishcheva, V.N. Morozov, V.A. Pletnyov, A.S. Semyonov, P.V. Shapkin, Development and studies of thin-film CdS_xSe_{1-x} waveguides, Kvantovaya Elektron, 9 (1982) 2329-2330.

[6] Z.E. Buachidze, I.S. Goldobin, B.N. Morozov, V.A. Pletnev, A.S. Semenov, P.V. Shapkin, Waveguide bragg modulators utilizing CdS_xSe_{1-x} crystals, Kvantovaya Elektron, 13 (1986) 698-703.

[7] Z.E. Buachidze, V.N. Morozov, V.A. Pletnev, M. Pukhta, A.S. Semenov, J. Ctyroky, Light propagation in a planar waveguide CdS_xSe_{1-x} structure with the variable bandgap along the surface, Kvantovaya Elektron, 14 (1987) 1619-1624.

[8] Y.J. Choi, K.S. Park, J.G. Park, Network-bridge structure of CdS_xSe_{1-x} nanowire-based optical sensors, Nanotechnology, 21 (2010) 505605.

[9] Z. Li, L.B. Yu, Y.B. Liu, S.Q. Sun, CdS_xSe_{1-x} alloyed quantum dots-sensitized solar cells based on different architectures of anodic oxidation TiO_2 film, J Nanopart Res, 16 (2014) 2779.

[10] S. Adachi, Handbook on Physical Properties of Semiconductors, Kluwer Academic Publishers, New York, 2004.

[11] M.O. Manasreh, Optoelectronic Properties of Semiconductors and Superlattices, Taylor & Francis Inc., New York, 2002.

[12] G. Perna, S. Pagliara, V. Capozzi, M. Ambrico, T. Ligonzo, Optical characterization of CdS_xSe_{1-x} films grown on quartz substrate by pulsed laser ablation technique, Thin Solid Films, 349 (1999) 220-224.

[13] G. Perna, S. Pagliara, V. Capozzi, H. Ambrico, M. Pallara, Excitonic luminescence of CdS_xSe_{1-x} films deposited by laser ablation on Si substrate, Solid State Communications, 114 (2000) 161-166.

[14] S. Pagliara, L. Sangaletti, L.E. Depero, V. Capozzi, G. Perna, Effect of disorder on the Raman scattering of CdS_xSe_{1-x} films deposited by laser ablation, Solid State Communications, 116 (2000) 115-119.

[15] H.S. Kwok, J.P. Zheng, S. Witanachchi, L. Shi, D.T. Shaw, Growth of CdS_xSe_{1-x} thin-films by laser evaporation deposition, Applied Physics Letters, 52 (1988) 1815-1818.

[16] G. Tan, S. Li, J.B. Murowchick, C. Wisner, N. Leventis, Z. Peng, Preparation of uncapped $CdSe_{1-x}S_x$ semiconducting nanocrystals by mechanical alloying, Journal of Applied Physics, 110 (2011) 124306.

[17] R.S. Mane, C.D. Lokhande, Studies on chemically deposited cadmium sulphoselenide (CdSSe) films, Thin Solid Films, 304 (1997) 56-60.

[18] A.M. Alcalde, A.A. Ribeiro, N.O. Dantas, D.R. Mendes, G.E. Marques, C. Trallero-Giner, Optical phonons and Raman scattering in ternary II-VI spheroidal nanocrystals embedded in a glass matrix, Journal of Non-Crystalline Solids, 352 (2006) 3618-3623.

[19] A. Goswami, Thin Film Fundamentals New Age International Limited, 1996.

[20] G.K. Williamson, W.H. Hall, X-ray line broadening from filed Aluminium and Wolfram, Acta Metallurgica, 1 (1953) 22 - 31.

[21] R. Swanepoel, Determination of the thickness and optical constants of amorphous silicon, Journal of Physics E: Scientific Instruments, 16 (1983) 1214.

[22] L. Hannachi, N. Bouarissa, Band parameters for cadmium and zinc chalcogenide compounds, Physica B: Condensed Matter, 404 (2009) 3650-3654.

[23] T.S. Moss, A Relationship between the Refractive Index and the Infra-Red Threshold of Sensitivity for Photoconductors, Proceedings of the Physical Society. Section B, 63 (1950) 167.

[24] P. Herve, L.K.J. Vandamme, General Relation between Refractive-Index and Energy-Gap in Semiconductors, Infrared Phys Techn, 35 (1994) 609-615.

[25] B. Pejova, The higher excited electronic states and spin-orbit splitting of the valence band in three-dimensional assemblies of close-packed ZnSe and CdSe quantum dots in thin film form, J Solid State Chem, 181 (2008) 1961-1969.

[26] S. Velumani, X. Mathew, P.J. Sebastian, S.K. Narayandass, D. Mangalaraj, Structural and optical properties of hot wall deposited CdSe thin films, Solar Energy Materials and Solar Cells, 76 (2003) 347-358.

[27] U. Pal, D. Samanta, S. Ghorai, A.K. Chaudhuri, Optical constants of vacuum-evaporated polycrystalline cadmium selenide thin films, Journal of Applied Physics, 74 (1993) 6368-6374.

[28] G.K.M. Thutupalli, S.G. Tomlin, The optical properties of thin films of cadmium and zinc selenides and tellurides, Journal of Physics D: Applied Physics, 9 (1976) 1639.

[29] E. Bacaksiz, S. Aksu, I. Polat, S. Yilmaz, M. Altunbas, The influence of substrate temperature on the morphology, optical and electrical properties of thermal-evaporated ZnSe thin films, Journal of Alloys and Compounds, 487 (2009) 280-285.

[30] Y.D. Kim, M.V. Klein, S.F. Ren, Y.C. Chang, H. Luo, N. Samarth, J.K. Furdyna, Optical properties of zinc-blende CdSe and $Zn_xCd_{1-x}Se$ films grown on GaAs, Physical Review B, 49 (1994) 7262-7270.

[31] M. Willatzen, M. Cardona, N.E. Christensen, Spin-orbit coupling parameters and electron g factor of II-VI zinc-blende materials, Physical Review B, 51 (1995) 17992-17994.

[32] T.M. Hayes, J.B. Boyce, Solid State Physics, Academic, New York, 1982.

[33] K.C. Hass, Bond relaxation in $Hg_{1-x}Cd_xTe$ and related alloys, Journal of Vacuum Science & Technology A: Vacuum, Surfaces, and Films, 5 (1987) 3019.

[34] I.F. Chang, S.S. Mitra, Application of a modified random-element-isodisplacement model to long-wavelength optic phonons of mixed crystals, Physical Review, 172 (1968) 924-933.

[35] Y.T. Nien, B. Zaman, J. Ouyang, I.G. Chen, C.S. Hwang, K. Yu, Raman scattering for the size of CdSe and CdS nanocrystals and comparison with other techniques, Materials Letters, 62 (2008) 4522-4524.

[36] S.N. Behera, P. Nayak, K. Patnaik, A new criterion for the mixed crystal behaviour in the diatomic linear chain model, Pramana - J. Phys., 8 (1977) 255-265.

[37] K.K. Nanda, S.N. Sarangi, S.N. Sahu, S.K. Deb, S.N. Behera, Raman spectroscopy of CdS nanocrystalline semiconductors, Physica B, 262 (1999) 31-39.

[38] C.M. Dai, D.S. Chuu, Observation of the transverse optical phonon mode in CdS film at 4880-A excitation, Journal of Applied Physics, 71 (1992) 3056-3058.

[39] A. Ingale, K.C. Rustagi, Raman spectra of semiconductor nanoparticles: Disorder-activated phonons, Physical Review B, 58 (1998) 7197-7204.

[40] O. Brafman, I.F. Chang, G. Lengyel, S.S. Mitra, E. Carnall, Optical phonons in ZnS$_x$Se$_{1-x}$ mixed crystals, Phys Rev Lett, 19 (1967) 1120-1123.

[41] A. Tu, P.D. Persans, Raman scattering as a compositional probe of II-VI ternary semiconductor nanocrystals, Applied Physics Letters, 58 (1991) 1506-1508.

Chapter 5

Growth and studies of ZnS_xSe_{1-x} ternary alloy thin films

In this chapter, growth, structual and optical properties of ZnS_xSe_{1-x} ternary alloy thin films as deposited by thermal evaporation of solvothermally synthesized ZnS-ZnSe composite powders are discussed. Since ternary alloying can be easily achieved by most deposition techniques in II-VI compounds [1-5], it is a very useful tool to control the structural and optical properties in order to design a material that may possess desired properties for a specific application. This possibility enhances the applicability of the II-VI compounds in various fields such as blue-green LEDs [6, 7], blue-green lasers [8], photodetectors [9], and as a buffer layer in thin film solar cells [10]. The material, in addition to being very promising for many electronic applications, also possess interesting optical and vibrational behavior. Spin orbit (SO) coupling effect in the optical spectra and two-phonon mode vibrational behavior in these alloys are interesting properties of these compounds, which may have certain implications in the performance of the material when used in optoelectronic devices. Though a few reports are available in literature, these two phenomena have not been clearly understood and to our knowledge there have not been proper experimental reports on the gap mode vibration of selenium in ZnS crystal as predicted theoretically [11]. With these motivation, we prepare ZnS_xSe_{1-x} (x = 0, 0.41, 0.51, 0.91, 1) ternary alloy thin films by varying the relative composition of ZnS and ZnSe in the composite powders. The structural, optical and vibrational properties of the films were investigated by X-ray diffraction (XRD), UV-Vis-NIR transmission and Raman scattering spectroscopy. We will discuss the changes in structural, optical and vibrational properties of the films with compositional variation in the following sections.

5.1 Results and discussion

5.1.1 EDX and XRD of the precursor ZnS-ZnSe composite powders

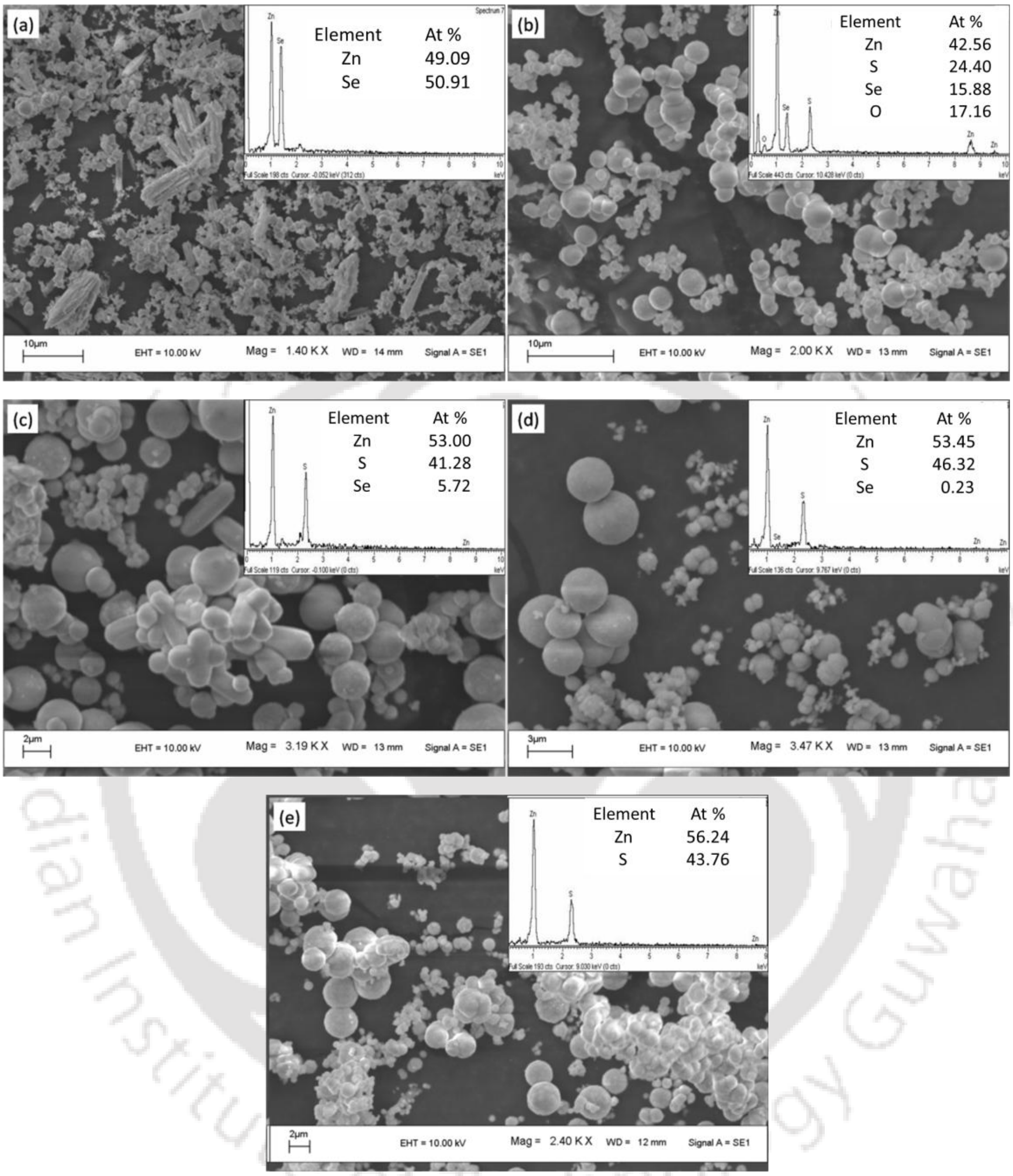

Figure 5.1: SEM images and EDX spectra of the synthesized binary and composite powders.

Figure 5.1 (a) - (e) show the SEM images and the corresponding EDX spectra of the synthesized ZnS-ZnSe composite powders. The composition, as shown in the figures, are an average of the measurements taken over 2-3 different positions in the SEM images. In addition to zinc, sulfur and selenium, traces of oxygen are also present in the composite powders. The three composite powder samples contain differerent amount of sulfur and selenium, which are uniformly mixed over the entire samples. Figure 5.2 (a) and (b) show the XRD patterns of two of the synthesized composite powders. The observed peaks correspond to the cubic planes of both ZnSe and ZnS indicating the composite nature of the synthesized powders.

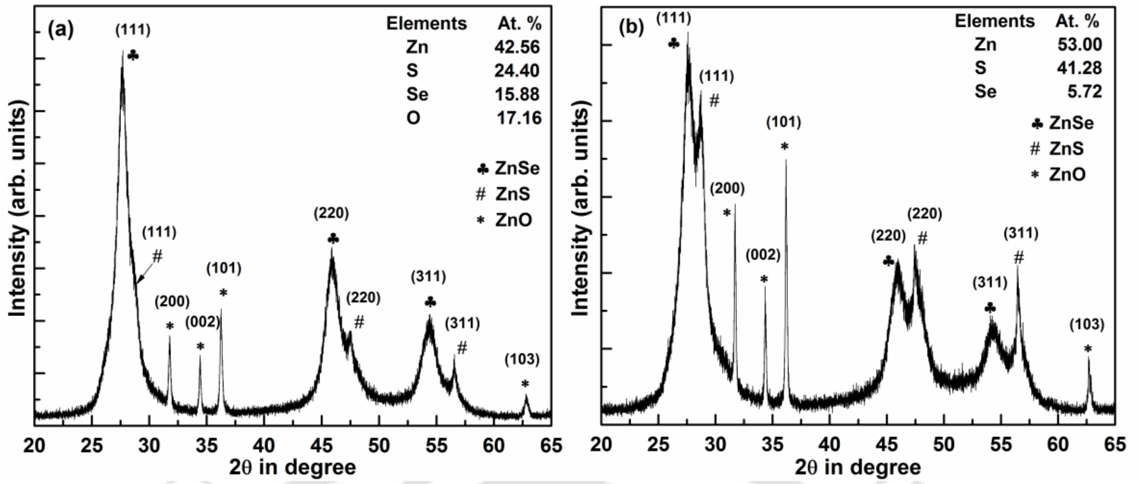

Figure 5.2: XRD pattern of two of the composite powders showing diffraction planes from both ZnS and ZnSe.

5.1.2 Composition and surface morphology studies of ZnS_xSe_{1-x} thin films

Figure 5.3 (a) - (e) show the EDX spectra of the films. The atomic percentage of different ions shown in this case are average over 2-3 measurements at different location on the films. Except for ZnSe, all the remaining films appear to be slightly Zn rich. The fraction of sulfur content (x) in the films is obtained by normalizing the total atomic percentage of anion content in the films. It is observed here that the films do not maintain the same composition as the source material. This may be understood by looking at the phenomena involve in our sample preparation process. Although the mechanism involved in the thermal evaporation process is quite simple and well understood, our preparation process, however, involves evaporation of composite powders consisting of two different binary compounds with different vapour pressure. The crystal growth in thermal evaporation process is largely determined by the rate of solid transport. The number of molecules (n) striking a surface of the substrate per unit area per unit time is related to the vapour pressure (p) as $n = (2\pi mkT)^{-1/2}.p$, where m is the molecular mass, and T is the absolute temperature [12]. Since the vapour pressure of ZnSe is higher than the vapour pressure of ZnS [13], it, therefore, results in unequal amount of ZnS and ZnSe molecules striking the surface of the substrate even for the same amount of the two materials. Hence, the formation of Zn-Se bonding in the resulting alloy is more favourable than Zn-S and thus, the composition of the resulting alloys do not match with the source composite powders.

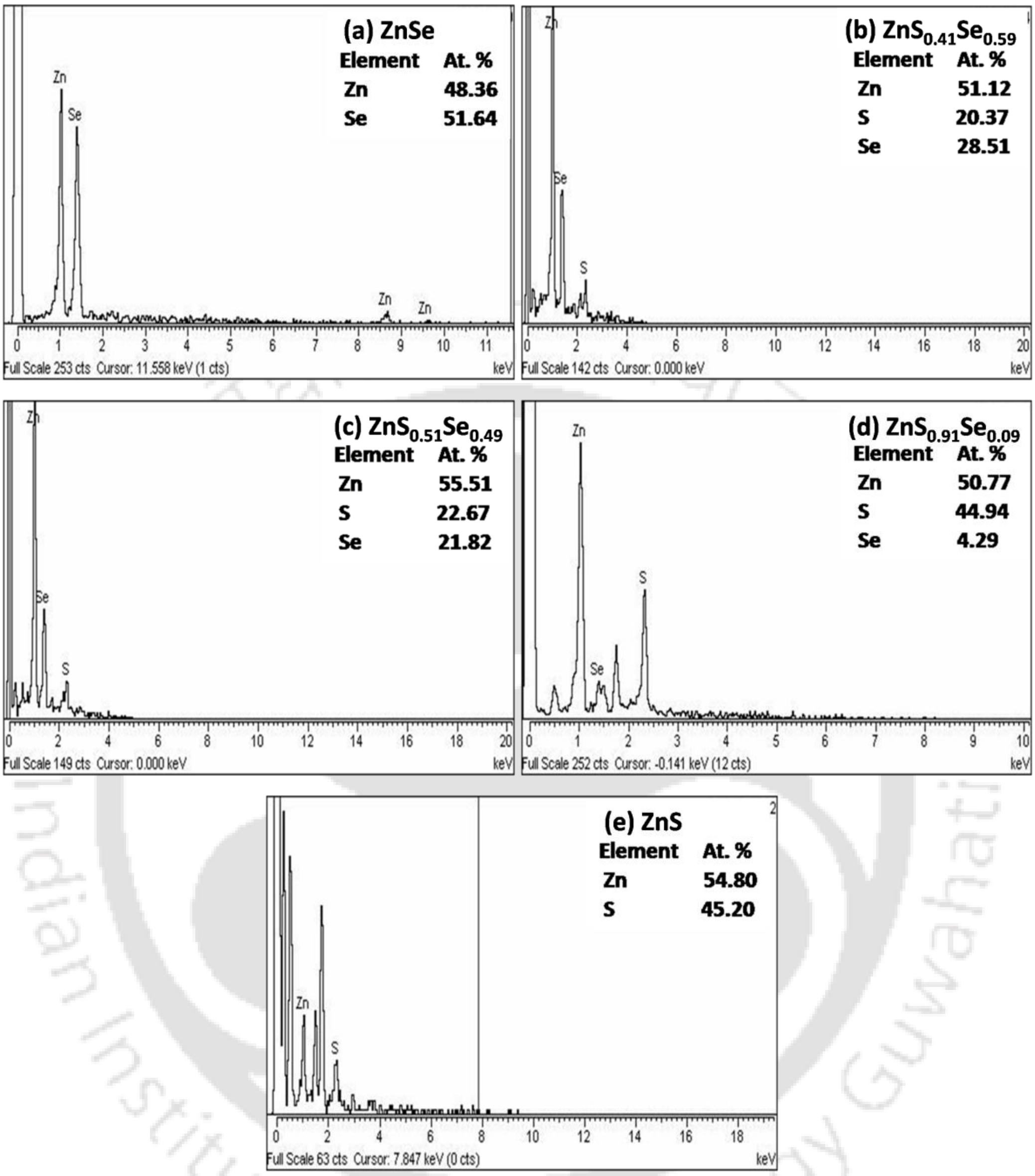

Figure 5.3: EDX spectra of ZnS_xSe_{1-x} (x = 0, 0.41, 0.51, 0.91, and 1) thin films.

FESEM images of the films are shown in figure 5.4. The films are deposited uniformly throughout the surface and consist of densely packed small grains without any pinhole. $ZnS_{0.41}Se_{0.59}$, $ZnS_{0.91}Se_{0.09}$ and ZnS samples consist of small and spherical shaped grains with an average diameter of around 50 nm. ZnSe and $ZnS_{0.51}Se_{0.49}$ samples, on the other hand, have much bigger irregular shaped grains with almost 100 nm diameter. Thus, the dimension of the grains and hence, the quality of the film surface is not monotonically varying with composition. Though the reason for this is not very clear, this could be due to some variation in substrate temperature during deposition.

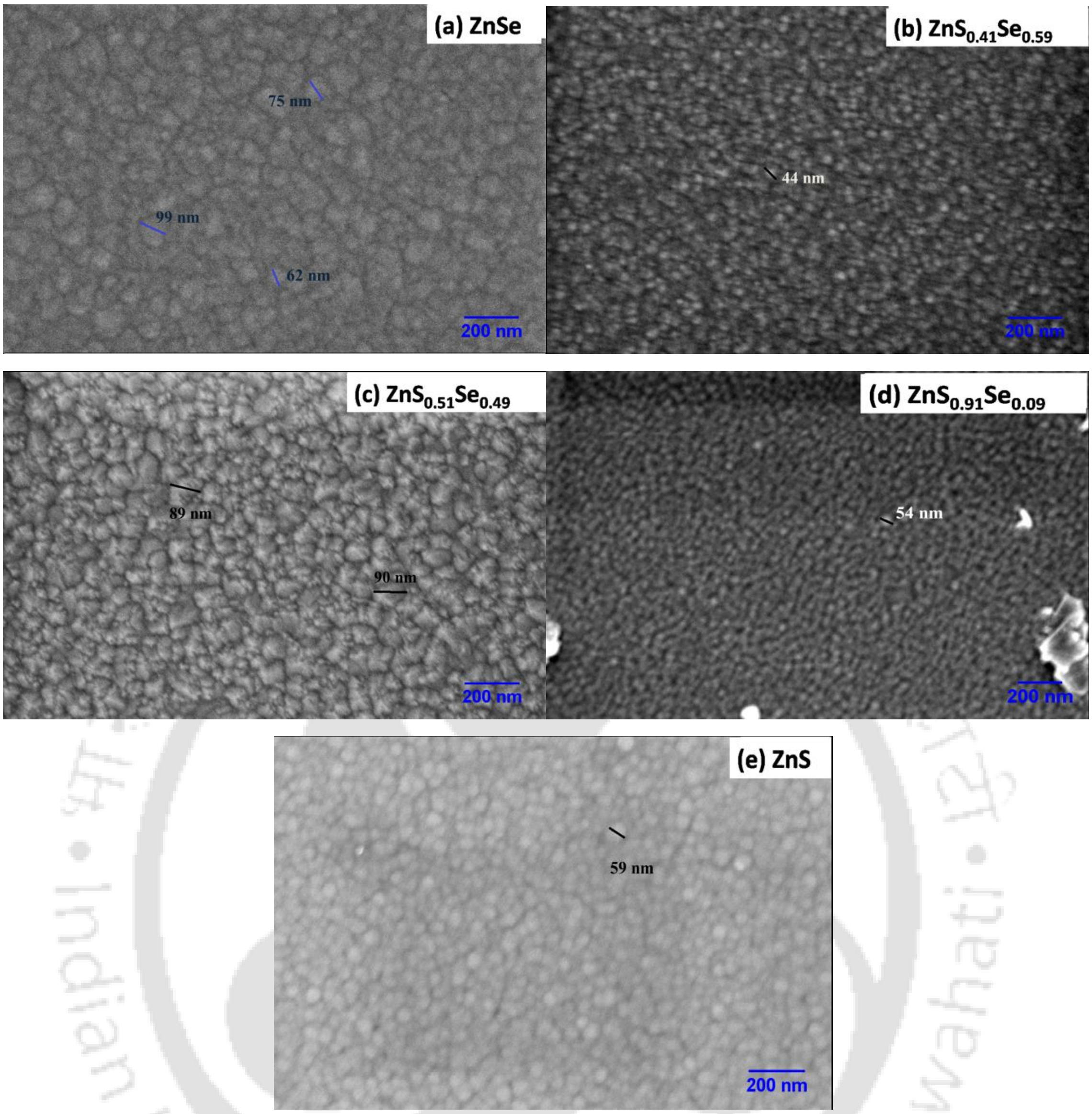

Figure 5.4: FESEM images of ZnS_xSe_{1-x} (x = 0, 0.41, 0.51, 0.91, and 1) thin films.

5.1.3 XRD studies

Figure 5. 5(a) show the XRD patterns of ZnS_xSe_{1-x} thin films (x = 0, 0.41, 0.51, 0.91, and 1). Contrary to the powder samples, where we observed peaks corresponding to the crystal planes of both ZnS and ZnSe, only one distinct characteristic peak corresponding to (111) plane of zinc blende structure [PDF #800021, PDF #772100] of the compound is observed. With the changing composition, the 2θ value of the diffraction peak shifts from 27.26° in ZnSe (x = 0) film to 28.62° in ZnS (x = 1) film.

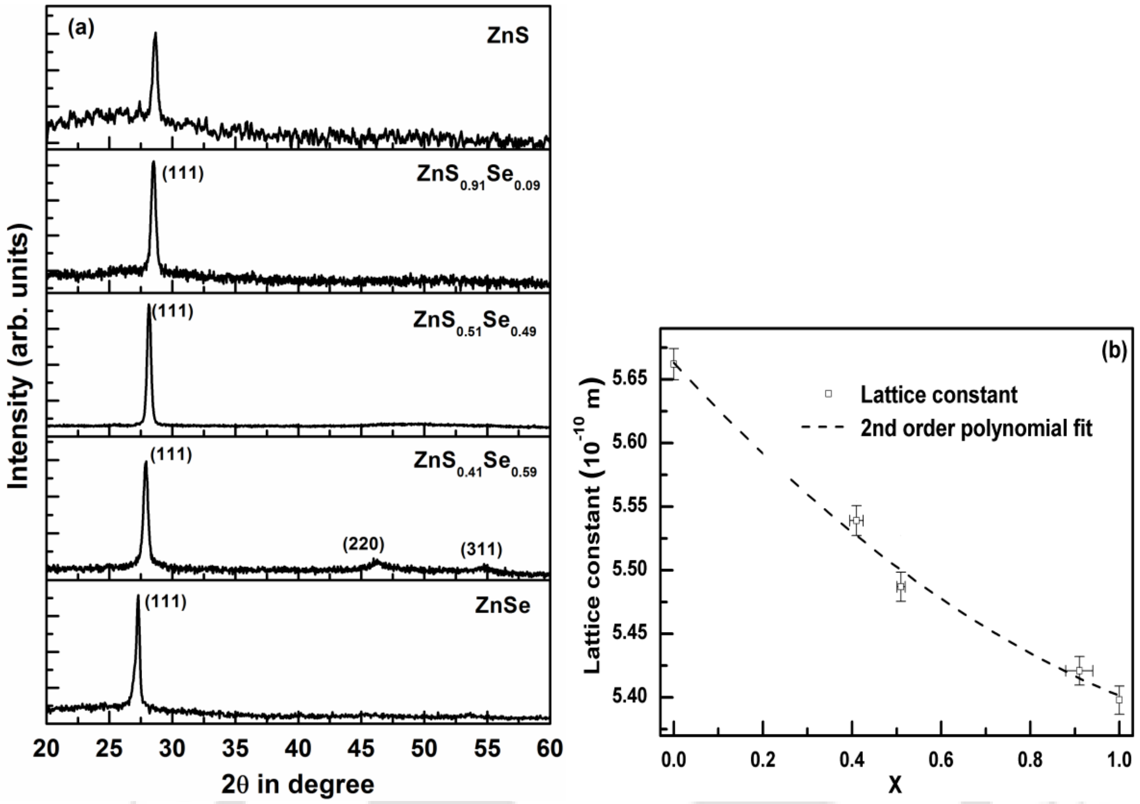

Figure 5.5: (a) XRD pattens of ZnS_xSe_{1-x} thin films (x = 0, 0.41, 0.51, 0.91, 1). (b) Plot of lattice constant (*a*) vs sulfur content (*x*).

Table 5.1: Structural parameters of ZnS_xSe_{1-x} thin films.

Sample	2 θ (degree)	β (FWHM) (degree)	Lattice constant 'a' (Å)	Lattice strain (× 10^{-3})	Dislocation density (lines/m^2) (× 10^{15})	Average crystallite size(nm)
ZnSe	27.260	0.316	5.662	1.34	1.37	27
$ZnS_{0.41}Se_{0.59}$	27.880	0.395	5.539	1.67	2.13	22
$ZnS_{0.51}Se_{0.49}$	28.150	0.309	5.487	1.30	1.30	28
$ZnS_{0.91}Se_{0.09}$	28.500	0.386	5.421	1.63	2.03	22
ZnS	28.625	0.376	5.398	1.59	1.93	23

Structural parameters of the alloys calculated from the (111) plane using Debye-Sherrer formula are given in table 5.1. Lattice constant '*a*'of the films decreases from 5.662 Å to 5.398 Å as *x* increases from 0 to 1. As shown in figure 5.5(b), this variation of lattice constant with composition nearly follows linear Vegard's relation, but with small deviations. Although, most mixed crystals have been assumed to follow the empirical Vegard's relation, deviation from the linear relation has been observed both experimentally and theoretically [14-17]. This could be due to large lattice parameter difference of the constituting binary compounds and non-linear variation of cell volume with compositional changes. The observed lattice parameter variation given in figure 5.5 (b), follows second order polynomial relation, $a_{ZnS_xSe_{1-x}} = (1-x)a_{ZnSe} + xa_{ZnS} - x(1-x)b$, with a bowing parameter b equal to 0.12 Å.

The calculated lattice strain and dislocation density of the films are given in table 5.1. These parameters correlate with the grain size of the particles. Samples with larger grains such as ZnSe and $ZnS_{0.51}Se_{0.49}$ have lower lattice strain and dislocation densities in comparision to the other three samples. The average crystallite size vary from 20 to 27 nm, which is much smaller than the grain sizes as observed in FESEM images. Since, it is not possible to isolate the size and strain broadening from a single diffraction peak [18], the average crystallite size as obtained from Debye-Sherrer formula is likely to be underestimated, whereas the strain and dislocation density may be slightly overestimated.

5.1.4 UV-Vis-NIR studies

Figure 5.6 (a) show the UV-Vis-NIR transmission spectra of the thin films at normal incidence. All the films show good interference pattern in the NIR region with maximum transmittance of about 90 % indicating that the films are uniformly deposited on the substrate. Optical absorption edge, as indicated by a sharp drop in the transmittance spectra, moves towards shorter wavelength with increasing x.

Optical parameters such as refractive index (n), absorption coefficient (α) and thickness of the films are determined from the transmission spectra using the method described by Swanepoel [19]. From these parameters, we obtain $(\alpha h\nu)^2$ *vs* $h\nu$ plot as given in figures 5.6 (b) - (f). The linear dependence of $(\alpha h\nu)^2$ on $h\nu$ in the plot indicates the occurrence of direct optical transition as expected in these semiconductors. The bandgap corresponding to each direct optical transitions are obtained by fitting a straight line as shown in the figures. The values obtained from these fittings are given in table 5.2. The binary sample ZnSe and the ternary samples with significant fraction of selenium atoms, $ZnS_{0.41}Se_{0.59}$, and $ZnS_{0.51}Se_{0.49}$ posses two bandgaps E_{g1} and E_{g2} corresponding to two direct optical transitions, $(\Gamma_8^v \rightarrow \Gamma_6^c)$and $(\Gamma_7^v \rightarrow \Gamma_6^c)$. However, the remaining two samples with very little amount of Se, $ZnS_{0.91}Se_{0.09}$ and ZnS posses only one bandgap. The bandgap values for the binary compounds, ZnSe and ZnS are comparable to the respective values as reported in literature [20-23].

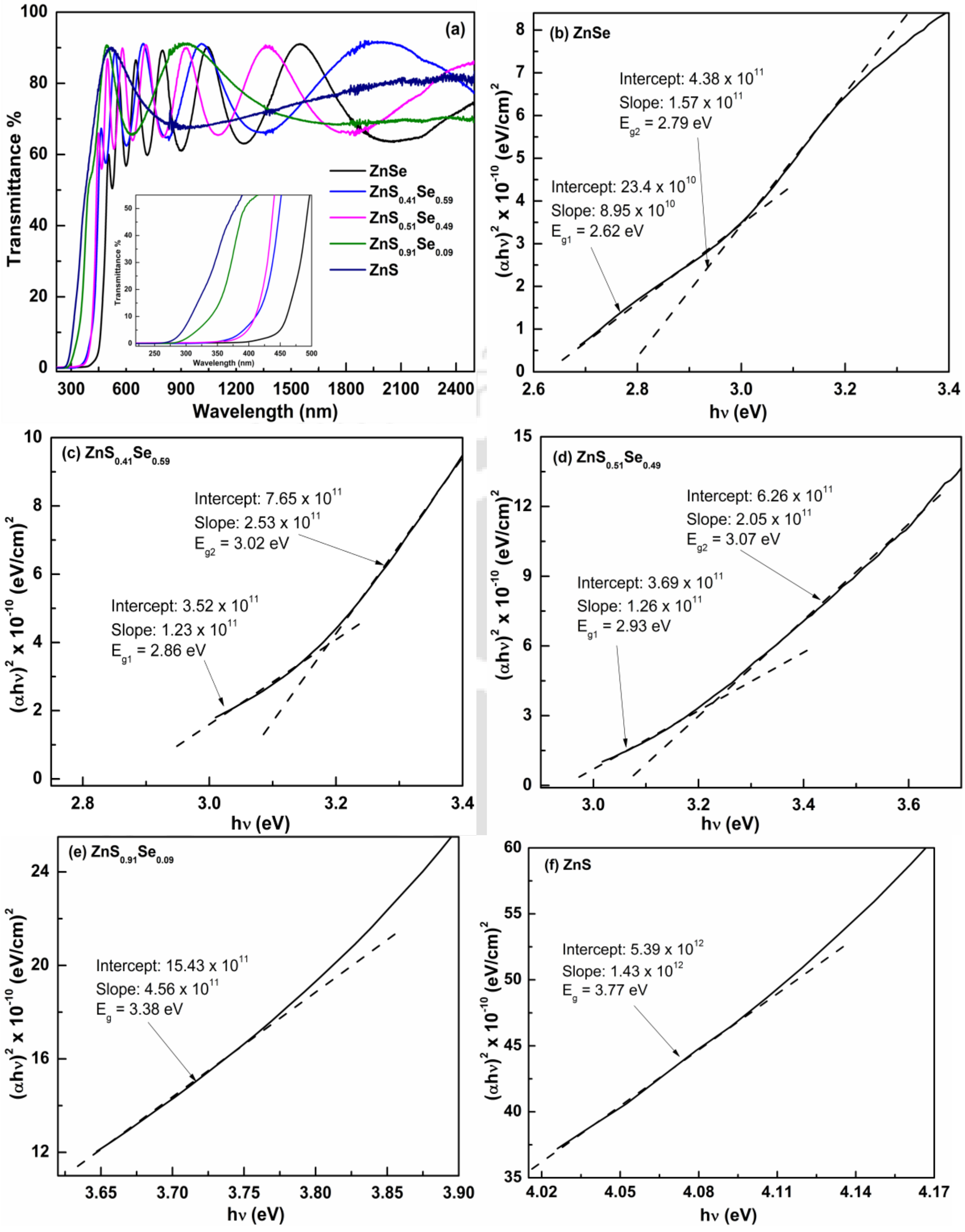

Figure 5.6: (a) UV-Vis-NIR transmission spectra of ZnS_xSe_{1-x} thin films (x = 0, 0.41, 0.51, 0.91, 1), (b) – (f) $(\alpha h\nu)^2$ *vs* $h\nu$ plot.

Table 5.2: Band gap, refractive index and film thickness of ZnS$_x$Se$_{1-x}$ alloy thin films.

Sample	Film thickness (nm)		n (550nm)	E$_{g1}$ ($\Gamma_8^v \to \Gamma_6^c$) eV	E$_{g2}$ ($\Gamma_7^v \to \Gamma_6^c$) eV	S-O splitting eV
	UV data	Profilometer				
ZnSe	640	670	2.61	2.62	2.79	0.17
ZnS$_{0.41}$Se$_{0.59}$	432	500	2.48	2.86	3.02	0.16
ZnS$_{0.51}$Se$_{0.49}$	590	550	2.45	2.93	3.07	0.14
ZnS$_{0.91}$Se$_{0.09}$	200	200	2.43	3.38		0
ZnS		152		3.77		0

The observed two direct optical transitions in ZnSe has been reported both theoretically and experimentally [24, 25]. However, for ternary compounds, the occurrence of two direct optical transitions is not reported to the best of our knowledge. The reported ZnSe band structure calculations [24] have shown that the valence band splits at the zone center into Γ_7^v and Γ_8^v resulting in two direct optical transitions as reported in this work. This splitting is, however, absent in the band structure of ZnS [26]. This splitting is due to the spin orbit (SO) coupling effect in the valence band, often observed in compounds consisting of anions with large ionic radii such as CdSe, CdTe, etc. [24, 27, 28]. In these materials, the nearly relativistic electronic velocities lead to sufficiently large magnetic fields so that the magnetic moments of orbital motion and the spin motion interact, which result in spin-orbit coupling. However, in the materials consisting of only light anions such as ZnS, CdS, etc, the magnetic field generated by orbiting electron is too weak to induce any coupling with electron spin.

SO splitting energy of all the samples is calculated from the difference in the energies of the two bandgap, E$_{g1}$ and E$_{g2}$. It is plotted against the fraction of sulfur (x) in figure 5.7 (a). The plot shows that, in addition to the well known SO splitting in ZnSe, significant SO splitting is observed even in ternary samples with large fraction of Se. Figure 5.7 (b) shows the bandgap energy vs sulfur content (x) plot. Dependence of the bandgap on composition of the alloy is non linear as predicted by Vegard's law. The second order polynomial fitting of E$_{g1}$and E$_{g2}$, both shown in the figure, results in bowing parameter of 0.98 and 0.72 eV respectively. This bowing is mainly due to the difference in bond lengths of the ZnS and ZnSe bonds. In ternary alloys, this difference alters the bond angles in order to preserve the bond lengths. This perturbs the atomic potentials, which results in non linear variation of bandgap energy even with uniform substitution of the constituent elements.

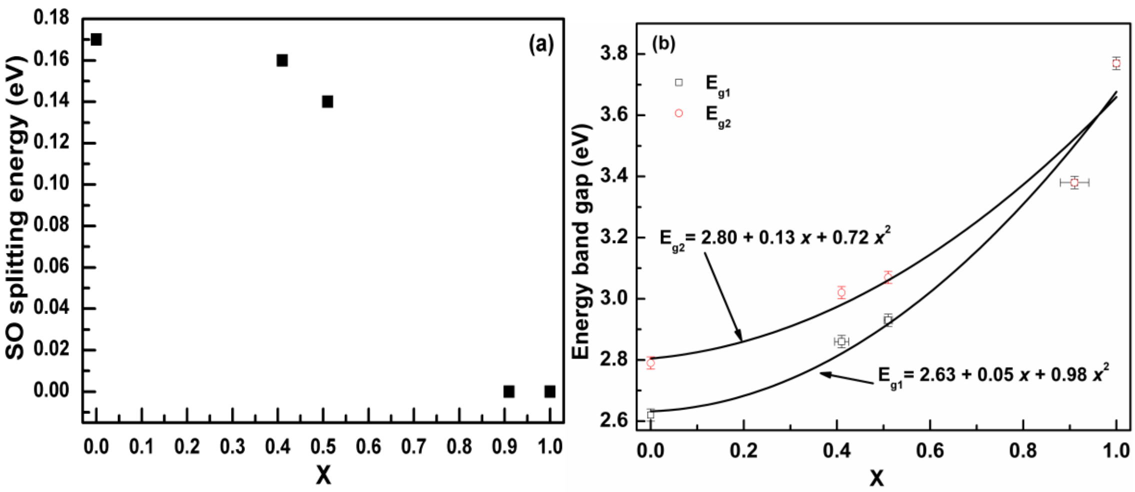

Figure 5.7: (a) Plot of SO splitting energy vs fraction of sulfur (*x*), (b) Plot of energy bandgap vs fraction of sulfur (*x*).

5.1.5 Raman scattering studies

The vibrational properties of the films are studied using Raman scattering measurements. Since, all our films have zinc blende structure with (111) orientation, scattering from both transverse optical (TO) and longitudinal optical (LO) phonons are permitted in these measurements. The room temperature Raman spectra are shown in figure 5.8. The ZnSe thin film has distinct vibrational bands corresponding to TO_{ZnSe}, LO_{ZnSe} and $2LO_{ZnSe}$ phonons. The spectra of all the ternary samples exhibit prominent Raman bands corresponding to both ZnSe and ZnS-like phonons as predicted by modified random element isodisplacement model (MREI) [11]. However, with the increase in fraction of sulfur in the film, not only that the intensity of ZnS-like phonon mode increases, we also observe increase in the intensity of disorder induced phonons (2TA and zone edge LO phonon modes for ZnS) and the scattering from the substrate. This substrate scattering largely dominates the Raman spectra of the ZnS thin film, which are relatively thin as shown in the figure. Nevertheless, weak TO_{ZnS} and asymmetric LO_{ZnS} can still be identified from the spectra as indicated in the figure.

For detailed investigation of different vibrational modes, all the Raman spectra are deconvoluted into the individual phonon modes of ZnS and ZnSe. Figures 5.9 (a) - (e) show the deconvoluted spectra. Except for the ZnS sample, the zone center (k = 0) phonons are fitted with Lorentzian peak and the disorder activated phonons with Gaussian peak. Since, the ZnS film is highly nanocrystalline, all the three phonon modes in ZnS are best fitted with Gaussian peak. In all the fittings, the cumulative fits and the raw data match very well as shown in the figures. The FWHM of all the phonon modes including the zone center phonons is comparatively much larger than the bulk values of about 7 - 8 cm^{-1} as reported for the II-VI binary compounds [29]. The LO and TO phonon modes of both ZnSe and ZnS are slightly red-shifted from the reported values (reported values are at TO_{ZnSe}= 205 cm^{-1} [23, 30, 31], LO_{ZnSe} = 250 cm^{-1} [23], TO_{ZnS} = 277 cm^{-1} [23, 32], LO_{ZnS} = 350 cm^{-1} [23, 32, 33]).

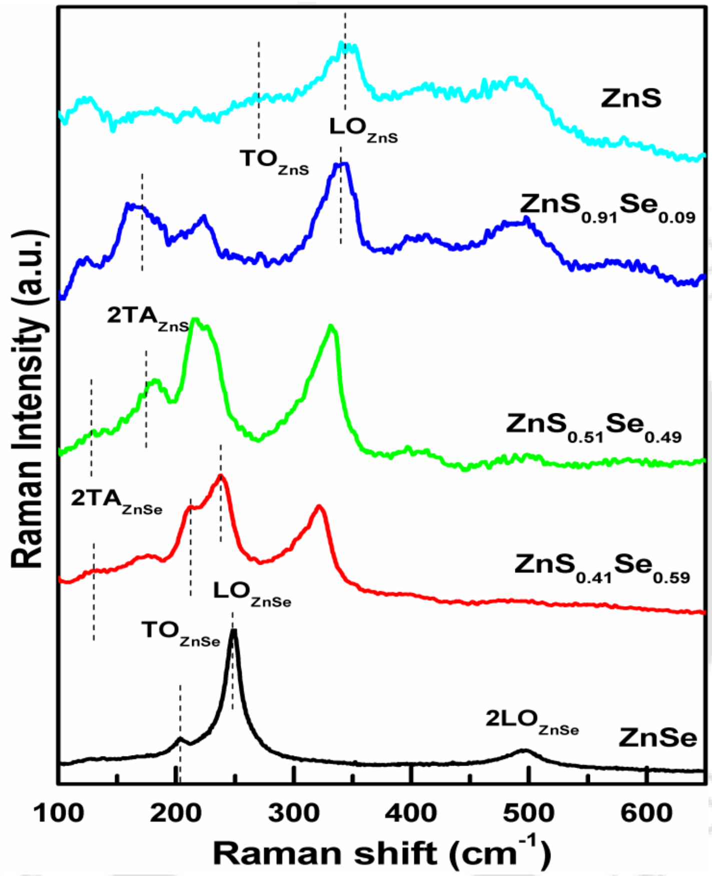

Figure 5.8: Raman spectra of ZnS_xSe_{1-x} (x = 0, 0.41, 0.51, 0.91, 1) thin films.

Strong first order zone center phonons such as TO_{ZnSe}, LO_{ZnSe} and LO_{ZnS} are observed in the deconvoluted spectra of two of the ternary alloys with large fraction of Se ($ZnS_{0.41}Se_{0.59}$ and $ZnS_{0.51}Se_{0.49}$). But the third ternary sample, i.e., $ZnS_{0.91}Se_{0.09}$ exhibits phonon mode, LO_{ZnS} and only one ZnSe-like phonon mode at 221 cm^{-1}. The LO_{ZnS} in all these ternary alloy samples have asymmetric broadening towards the lower wave number side. It is fitted with additional Lorentzian peak, which is identified as zone edge LO phonon (ZE LO_{ZnS}). Similar asymmetric broadening is also observed in zone center LO_{ZnSe} and LO_{ZnS} phonons in the binary compounds (ZnSe and ZnS). The asymmetric broadening in both of these binary samples fits well with an additional

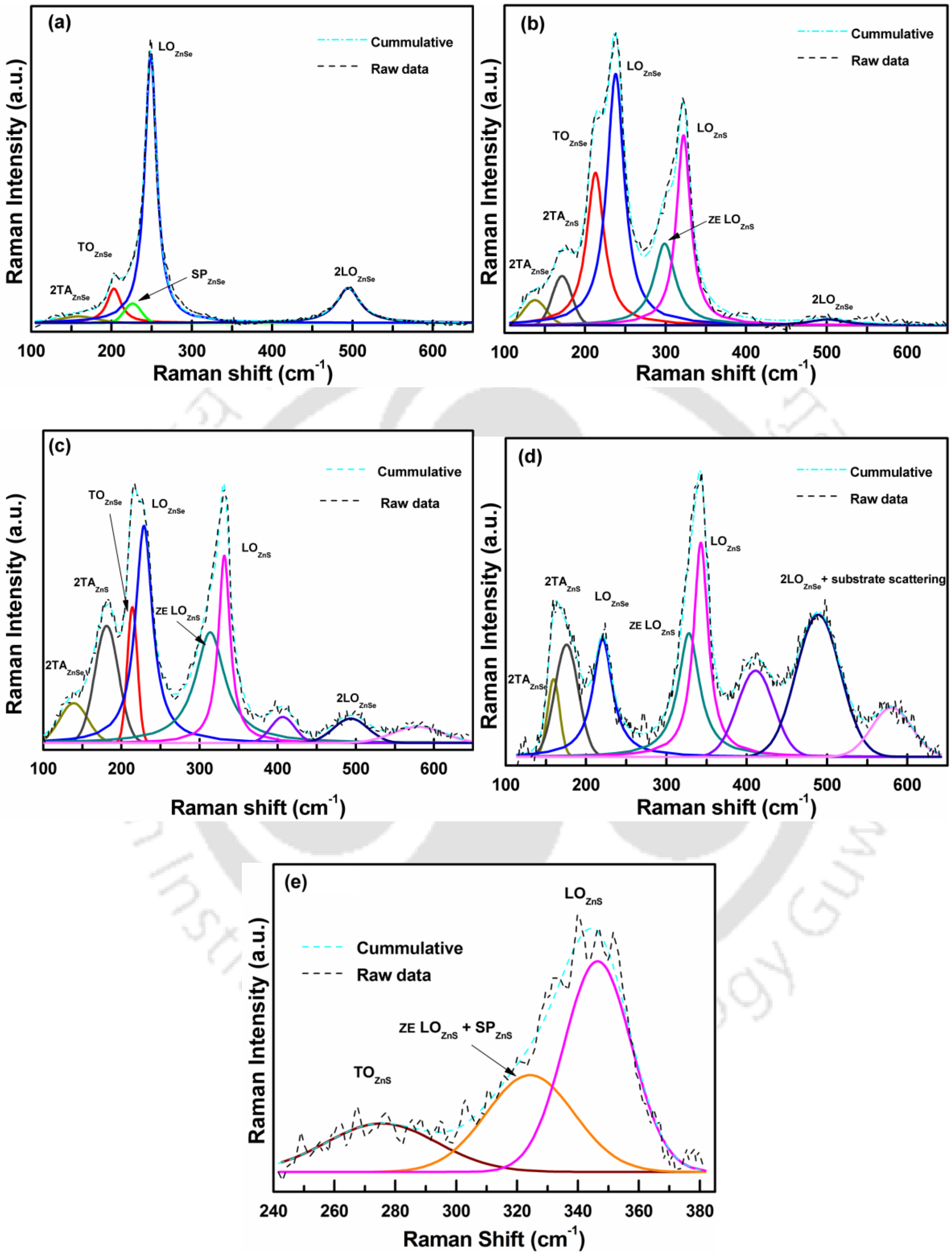

Figure 5.9: Deconvoluted Raman spectra of (a) ZnSe, (b) $ZnS_{0.41}Se_{0.59}$, (c) $ZnS_{0.51}Se_{0.49}$, (d) $ZnS_{0.91}Se_{0.09}$ and (e) ZnS thin films.

Table 5.3: Phonon modes of ZnS$_x$Se$_{1-x}$ (x = 0, 0.41, 0.51, 0.91, 1) thin films.

Phonon mode	ZnSe			ZnS$_{0.41}$Se$_{0.59}$			ZnS$_{0.51}$Se$_{0.49}$			ZnS$_{0.91}$Se$_{0.09}$			ZnS		
	Band centre	FWHM (cm^{-1})	Intensity	Band centre	FWHM (cm^{-1})	Intensity	Band centre	FWHM (cm^{-1})	Intensity	Band centre	FWHM (cm^{-1})	Intensity	Band centre	FWHM (cm^{-1})	Intensity
2TA$_{ZnSe}$	159	54	151	138	33	149	139	42	116	159	18	245			
2TA$_{ZnS}$				171	29	292	181	36	341	176	35	354			
TO$_{ZnSe}$	203	21	805	213	27	903	214	15	396						
SP$_{ZnSe}$	226	25	454												
LO$_{ZnSe}$	249	18	6317	238	26	1489	229	26	633	221	29	371			
TO$_{ZnS}$													275	43	39
ZE LO$_{ZnS}$				299	32	484	313	46	321	328	32	389	324	34	78
LO$_{ZnS}$				322	21	1125	332	18	547	343	22	674	346	26	170

Gaussian peak as shown in the deconvoluted spectra. These are identified as SP_{ZnSe} and SP_{ZnS} + ZE LO_{ZnS} as indicated in the figures. In addition to these optical phonons, disorder induced acoustic phonons such as $2TA_{ZnSe}$ (transverse acoustic mode of ZnSe) and $2TA_{ZnS}$ (transverse acoustic mode of ZnS) are also observed. The strength of $2TA_{ZnS}$ phonon increases as the sulfur content increases. The strength of $2TA_{ZnSe}$ phonon, however, appears to remain constant due to the increased scattering from the substrate at around 135 cm^{-1}. This occur because of the decrease in thickness and absorption coefficient in the samples with larger fraction of sulfur.

The plot of intensity ratio of the two LO phonons $\left[\frac{I(LO_{ZnS})}{I(LO_{ZnSe})}\right]$ against the fraction of sulfur (x) is given in figure 5.10 (a). The plot shows that the relative strength of the zone center phonons is dependent on the fraction of sulfur as has been reported for other mixed crystals exhibiting two-mode behavior [34]. The intensity ratio $\left[\frac{I(LO_{ZnS})}{I(LO_{ZnSe})}\right]$ increases from 0.76 in $ZnS_{0.41}Se_{0.59}$ to 1.82 in $ZnS_{0.91}Se_{0.09}$. This corresponds to the increasing number of Zn-S bond (decreasing number of Zn-Se bond) in the mixed crystal as more number of anion sites in the crystal are occupied by S atom.

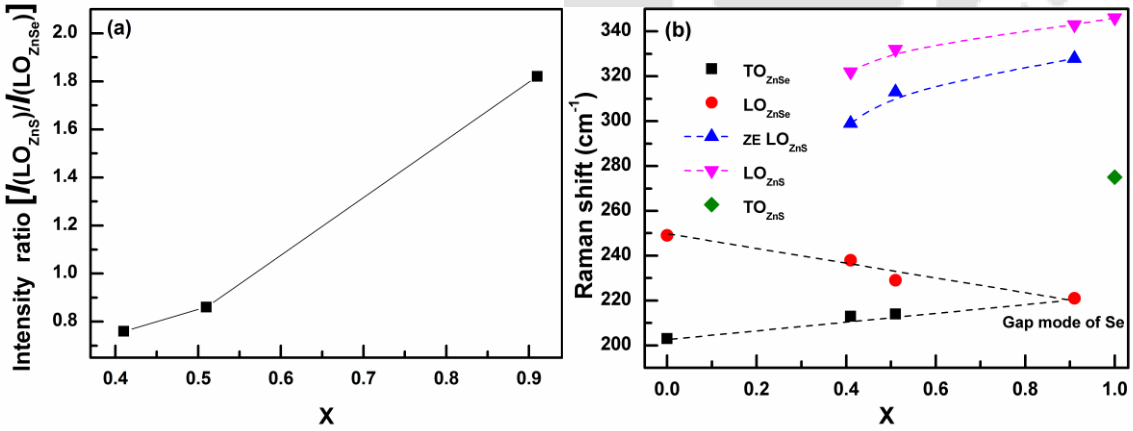

Figure 5.10: (a) Plot of intensity ratio of the two LO phonons $\left[\frac{I(LO_{ZnS})}{I(LO_{ZnSe})}\right]$ vs fraction of sulfur (x), (b) Plot of Raman shift vs fraction of sulfur (x).

Figure 5.10 (b) shows the Raman shift of the first order Raman modes plotted against the sulfur content (*x*). The TO_{ZnSe} and LO_{ZnSe} phonon mode frequencies, which are widely separated in pure ZnSe sample, gets narrower with the increase in sulfur content. In $ZnS_{0.91}Se_{0.09}$ sample, the TO_{ZnSe} and LO_{ZnSe} merge together resulting in a weak phonon at 221 cm^{-1}, which is the gap mode of Se in ZnS lattice as theoretically predicted [11, 35]. In this sample, the small fraction of Se in the ZnS lattice vibrates at a frequency lower than the optical phonons of ZnS, thereby resulting in a phonon mode at the forbidden gap.

Observation of asymmetric broadening in LO_{ZnS} phonon mode is a very interesting feature of ZnS_xSe_{1-x} ternary alloys, which, to our knowledge is not yet reported. Similar broadening in LO_{CdS} phonon modes in the Raman spectra of CdS_xSe_{1-x} thin films, however, has been reported [36, 37]. In nanocrystalline materials, the surface phonon modes could result in this asymmetric broadening, whereas in case of thin films and single crystals, the contribution from zone edge LO phonon vibrations are believed to be responsible for the observed asymmetry.

In our analysis of asymmetrically broadened LO_{ZnS}, we used the two-Lorentzian functions as proposed by both Pagliara et. al [36] and Ingale et. al [37]. We observe that the frequency of additional Lorentzian peak shifts in the same manner as the zone center phonon mode as shown in figure 5.9 (b). For each of the ternary alloys, the Raman shift of the additional Lorentzian peak is about 20 cm^{-1} below the zone center LO phonon mode and both increasing with the sulfur atomic concentration. This additional Lorentzian peak is, thus, assigned to ZE LO_{ZnS} and its origin can be understood from the dispersion curve of the binary compounds (ZnS and ZnSe) [23, 38, 39]. In the dispersion curve of ZnS [39], the LO_{ZnS} and TO_{ZnS} phonon modes are still widely separated at the zone boundaries forming distinct zone edge phonon vibrations, ZE LO_{ZnS} and ZE TO_{ZnS} respectively at frequencies which are slightly different from the respective zone center phonon modes. These phonon modes can become Raman active once we have significant disorder. The ZE LO_{ZnS} frequency being lower than the zone center LO_{ZnS} phonon for about 20 cm^{-1}, results in asymmetric broadening of LO_{ZnS} on the lower wave number side as observed in our samples. However, in the dispersion curve of ZnSe [38], the LO_{ZnSe} phonon mode frequency falls down and merges with TO_{ZnSe} phonon mode at the zone boundaries and results in a zone edge vibrational mode close to the zone center TO_{ZnSe}

phonon mode, which can not be distinguished. Thus, the zone edge phonon in ZnSe can not be distinctly observed as in the case of ZE LO_{ZnS} and if it becomes Raman active, it would contribute to the TO_{ZnSe}.

The assigned Gaussian peaks in asymmetrically broadened binary compounds (ZnSe and ZnS) can also be explained from the above discussion. Since, the asymmetric Gaussian peak in LO_{ZnS} is very large, it could be due to the contributions from both ZE LO_{ZnS} and the surface phonon (SP_{ZnS}) mode. However, since zone edge contribution does not occur in ZnSe, a weak Gaussian peak as observed in the present case could be solely due to the surface phonon (SP_{ZnSe}) mode.

5.2 Summary

ZnS_xSe_{1-x} ($x = 0, 0.41, 0.51, 0.91, 1$) ternary alloy thin films with variable structural, optical and vibrational properties are successfully prepared by employing a simple thermal evaporation route using ZnS-ZnSe composite powders as the precursor for evaporation. The uniformly mixed ZnS and ZnSe in the form of composite powder results in uniform deposition of the alloy films. All the films possess cubic zinc blende structure with a single characteristic diffraction peak corresponding to (111) plane, which shifts according to compositional variation. The lattice parameter as deduced from the XRD changes almost linearly with compositional change but with a bowing of 0.12 Å. The optical studies indicate the occurence of SO splitting in ZnS_xSe_{1-x} ternary compounds having significant amount of Se. Even though the band structure of this ternary alloy has not been well understood, we are able to show that the relative fraction of anions in the alloy not only affect the bandgap but also determines the extent of SO splitting in the valence band. The vibrational property of the ternary alloys exhibit two phonon mode behavior as predicted by modified random element iso-displacement (MREI) model. The changes in Raman shift with fraction of sulfur content follows the theoretically predicted pattern. The LO_{ZnSe} and TO_{ZnSe} phonon frequencies merge at 221 cm^{-1} in $ZnS_{0.91}Se_{0.09}$, forming the gap mode of Se in ZnS lattice. To our knowledge, we are the first to experimentally report Se gap mode in ZnS_xSe_{1-x} ternary system.

5.3 References

[1] K.T.R. Reddy, Y.V. Subbaiah, T.B.S. Reddy, D.B. Johnston, I. Forbes, R.W. Miles, Pyrolytic spray deposition of ZnS$_x$Se$_{1-x}$ layers for photovoltaic applications, Thin Solid Films, 431 (2003) 340-343.

[2] S. Armstrong, P.K. Datta, R.W. Miles, Properties of zinc sulfur selenide deposited using a close-spaced sublimation method, Thin Solid Films, 403–404 (2002) 126-129.

[3] R. Rujkorakarn, A.J. Nelson, Optical properties of ZnS$_{1-x}$Se$_x$ alloys fabricated by plasma-induced isoelectronic substitution, Journal of Applied Physics, 87 (2000) 8557-8560.

[4] A.L. Gurskii, E.V. Lutsenko, G.P. Yablonskii, V.I. Kozlovsky, A.B. Krysa, J. Söllner, M. Scholl, H. Hamadeh, M. Heuken, Photo- and cathodoluminescence of ZnSSe quantum well heterostructures grown by MOVPE, Journal of Crystal Growth, 159 (1996) 518-522.

[5] C.T. Hsu, Growth of ZnS$_x$Se$_{1-x}$ layers on Si substrates by atomic layer epitaxy, Materials Chemistry and Physics, 58 (1999) 6-11.

[6] P. Uusimaa, A. Salokatve, K. Rakennus, A. Rinta-Moykky, M. Pessa, Blue-green microcavity light emitting diode with monolithic MgZnSSe/ZnSSe Bragg reflectors, Materials Science and Engineering: B, 51 (1998) 18-21.

[7] H.C. Lee, T. Abe, M. Watanabe, Z.M. Aung, M. Adachi, T. Shirai, H. Yamada, S. Kuroda, H. Kasada, K. Ando, Efficient blue–green light-emitting diodes of ZnSSe : Te/ZnMgSSe DH structure grown by molecular-beam epitaxy, Journal of Crystal Growth, 214–215 (2000) 1096-1099.

[8] T.V. Shubina, S.V. Ivanov, A.A. Toropov, G.N. Aliev, M.G. Tkatchman, S.V. Sorokin, N.D. Il'inskaya, P.S. Kop'ev, Extremely thick ZnCdSe/ZnSSe multiple quantum-well heterostructures for optoelectronic applications, Journal of Crystal Growth, 184–185 (1998) 596-600.

[9] K.S. Wong, T. Sun, B.K.K. Fung, I.K. Sou, G.K.L. Wong, Visible to ultraviolet femtosecond autocorrelation measurements based on two-photon absorption using ZnSSe photodetector, Journal of Crystal Growth, 227–228 (2001) 717-721.

[10] Y.P.V. Subbaiah, P. Prathap, K.T.R. Reddy, R.W. Miles, J. Yi, Studies on $ZnS_{0.5}Se_{0.5}$ buffer based thin film solar cells, Thin Solid Films, 516 (2008) 7060-7064.

[11] I.F. Chang, S.S. Mitra, Application of a modified random-element-isodisplacement model to long-wavelength optic phonons of mixed crystals, Physical Review, 172 (1968) 924-933.

[12] I. Langmuir, The Vapor Pressure of Metallic Tungsten, Physical Review, 2 (1913) 329-342.

[13] A. Goswami, Thin Film Fundamentals New Age International Limited, 1996.

[14] K.T. Jacob, S. Raj, L. Rannesh, Vegard's law: a fundamental relation or an approximation?, Int J Mater Res, 98 (2007) 776-779.

[15] Y.K. Kuo, B.T. Liou, S.H. Yen, H.Y. Chu, Vegard's law deviation in lattice constant and band gap bowing parameter of zincblende InxGa1-xN, Opt Commun, 237 (2004) 363-369.

[16] S.T. Murphy, A. Chroneos, C. Jiang, U. Schwingenschlogl, R.W. Grimes, Deviations from Vegard's law in ternary III-V alloys, Physical Review B, 82 (2010) 073201.

[17] A.B.M.A. Ashrafi, Y. Segawa, Determination of Mg composition in $Mg_xZn_{1-x}O$ alloy: Validity of Vegard's law, J Vac Sci Technol B, 23 (2005) 2030-2033.

[18] G.K. Williamson, W.H. Hall, X-ray line broadening from filed Aluminium and Wolfram, Acta Metallurgica, 1 (1953) 22 - 31.

[19] R. Swanepoel, Determination of the thickness and optical constants of amorphous silicon, Journal of Physics E: Scientific Instruments, 16 (1983) 1214.

[20] M. Ashraf, S.M.J. Akhtar, A.F. Khan, Z. Ali, A. Qayyum, Effect of annealing on structural and optoelectronic properties of nanostructured ZnSe thin films, Journal of Alloys and Compounds, 509 (2011) 2414-2419.

[21] Y.P. Venkata Subbaiah, P. Prathap, M. Devika, K.T.R. Reddy, Close-spaced evaporated ZnSe films: Preparation and characterization, Physica B: Condensed Matter, 365 (2005) 240-246.

[22] A. Goudarzi, G.M. Aval, R. Sahraei, H. Ahmadpoor, Ammonia-free chemical bath deposition of nanocrystalline ZnS thin film buffer layer for solar cells, Thin Solid Films, 516 (2008) 4953-4957.

[23] S. Adachi, Handbook on Physical Properties of Semiconductors, Kluwer Academic Publishers, New York, 2004.

[24] J.R. Chelikowsky, M.L. Cohen, Nonlocal pseudopotential calculations for the electronic structure of eleven diamond and zinc-blende semiconductors, Physical Review B, 14 (1976) 556-582.

[25] B. Pejova, The higher excited electronic states and spin-orbit splitting of the valence band in three-dimensional assemblies of close-packed ZnSe and CdSe quantum dots in thin film form, J Solid State Chem, 181 (2008) 1961-1969.

[26] T. Tomohide, O. Shunji, A. Sadao, Modelling the optical constants of cubic ZnS in the 0–20 eV spectral region, Journal of Physics: Condensed Matter, 15 (2003) 3717.

[27] Y.D. Kim, M.V. Klein, S.F. Ren, Y.C. Chang, H. Luo, N. Samarth, J.K. Furdyna, Optical properties of zinc-blende CdSe and Zn$_x$Cd$_{1-x}$Se films grown on GaAs, Physical Review B, 49 (1994) 7262-7270.

[28] S. Velumani, X. Mathew, P.J. Sebastian, S.K. Narayandass, D. Mangalaraj, Structural and optical properties of hot wall deposited CdSe thin films, Solar Energy Materials and Solar Cells, 76 (2003) 347-358.

[29] Y.T. Nien, B. Zaman, J. Ouyang, I.G. Chen, C.S. Hwang, K. Yu, Raman scattering for the size of CdSe and CdS nanocrystals and comparison with other techniques, Materials Letters, 62 (2008) 4522-4524.

[30] D. Huang, C. Jin, D. Wang, X. Liu, J. Wang, X. Wang, Crystal structure and Raman scattering in Zn$_{1-x}$Mg$_x$Se alloys, Applied Physics Letters, 67 (1995) 3611-3613.

[31] M. Kozielski, M. Szybowicz, F. Firszt, S. Legowski, H. Meczynska, J. Szatkowski, W. Paszkowicz, Study of the A$_{1-x}$B$_x$C mixed crystals by Raman scattering, Cryst Res Technol, 34 (1999) 699-702.

[32] Landolt-Bornstein, Numerical Data and Functional Relationships in Science and Technology, Springer, Berlin, 1982.

[33] A. Memon, D.B. Tanner, Far-Infrared Dielectric Function of Zincblende ZnS, Physica Status Solidi (b), 128 (1985) 49-52.

[34] A. Tu, P.D. Persans, Raman scattering as a compositional probe of II-VI ternary semiconductor nanocrystals, Applied Physics Letters, 58 (1991) 1506-1508.

[35] O. Brafman, I.F. Chang, G. Lengyel, S.S. Mitra, E. Carnall, Optical phonons in ZnS_xSe_{1-x} mixed crystals, Phys Rev Lett, 19 (1967) 1120-1123.

[36] S. Pagliara, L. Sangaletti, L.E. Depero, V. Capozzi, G. Perna, Effect of disorder on the Raman scattering of CdS_xSe_{1-x} films deposited by laser ablation, Solid State Communications, 116 (2000) 115-119.

[37] A. Ingale, K.C. Rustagi, Raman spectra of semiconductor nanoparticles: Disorder-activated phonons, Physical Review B, 58 (1998) 7197-7204.

[38] B. Hennion, F. Moussa, G. Pepy, K. Kunc, Normal modes of vibrations in ZnSe, Physics Letters A, 36 (1971) 376-378.

[39] N. Vagelatos, D. Wehe, J.S. King, Phonon dispersion and phonon densities of states for ZnS and ZnTe, The Journal of Chemical Physics, 60 (1974) 3613-3618.

Chapter 6

Conclusions and Future Scope

This thesis presents the growth and studies of nanostructured II-VI binary compounds; CdSe and ZnSe and the preparation and studies of CdS_xSe_{1-x} and ZnS_xSe_{1-x} ternary alloy thin films. The investigation on the nanostructured binary compounds is focused mainly on the control of structural, morphological, optical and thermal stability with variation in reaction time in the solvothermal synthesis. In this study, samples of nanostructured CdSe and ZnSe binary compounds are prepared for 1, 3 and 5h reaction time. The investigation on the ternary alloys is focused on the study of structural, vibrational and optical properties with compositional changes. In order to obtain ternary alloy thin films of various compositions, composite powder samples with varying fraction of sulfur and selenium are synthesized using solvothermal process. The thin film samples are obtained by thermal evaporation of these powders. In this study, five thin film samples including the end binary compounds are prepared in both CdS_xSe_{1-x} and ZnS_xSe_{1-x}. These investigations are performed in order to understand the material properties due to their vast potential in number of optoelectronic applications. Our investigation and studies result in the following conclusions.

6.1 Conclusions

- CdSe nanorods and ZnSe nanocystalline powders are synthesized by solvothermal method using a mixed solvent consisting of ammonia, hydrazine hydrate and deionized water. Our results show that the structural, optical and thermal stability of the nanorods can be controlled significantly by changing the reaction time in the solvothermal reaction.
- The solvothermal reaction route used in the thesis work results in chemically pure CdSe nanorods with high thermal stability. The thermal decomposition occurs rapidly and is best described by the contracting cylinder model.

- The investigations on ZnSe nanocrystals reveal that the chemical purity improves with reaction time. Thermal stability study shows that ZnSe nanocrystals decomposed at relatively lower temperature than the CdSe nanorods. The decomposition of the ZnSe nanocrystals also occurs rapidly and is best described by the contracting sphere model.
- Absorbance and photoluminescence study on both the nanostructures show the evidence of enhanced confinement by the presence of lattice strain.
- CdS_xSe_{1-x} and ZnS_xSe_{1-x} ternary alloys are prepared by using simple thermal evaporation process. Structural and optical properties are tuned by controlling composition of the thin films.
- Optical transitions corresponding to spin orbit splitting of valence band is observed in binary and ternary alloys with large fraction of selenium. The SO splitting energy is observed to be dependent on the fraction of selenium in the alloys.
- The observed changes in dual phonon mode behavior in the alloys with compositional variation match with the theoretical prediction according to modified random element isodisplacement model (MREI).
- Gap mode vibration of a small fraction of Se in the ZnS lattice is observed in ZnS_xSe_{1-x} ternary alloy thin films as theoretically predicted.

6.2 Future Scope

Some of the future research scopes based on the present thesis work are as follows.

- In the solvothermal synthesis route as implemented in this work, investigation on the changes in nanostructure properties is performed only by varying one of the synthesis parameters. Further improvement on the nanostructure properties may be achieved by optimizing other synthesis parameters such as relative concentration of solvents, precursor salts and reaction temperature.
- In the study on decomposition kinetics of nanostructured CdSe and ZnSe binary compounds, experiment is performed only for a single heating rate (10 ^{o}C/min) for each sample due to limited availability of the TGA measurement instrument. Because of this, analysis is performed only using Coats-Redfern Method, which relies only on a single heating rate. Though, this method provides information on

the thermal parameters that accompany the decomposition of nanoparticles, experiment using different heating rates will enable the use of other methods such as Ozawa and Kissinger methods. This study will give better estimate of the decomposition kinetics and thermodynamic parameters.

- All optical studies including photoluminescence (PL) and Raman spectroscopy on nanostructured CdSe and ZnSe binary compounds are performed at room temperature. The results shown in the thesis work indicates low signal to noise ratio. This encumbers correct separation of the contribution of the surface phonons and determination of the phonon band parameters in Raman spectroscopy. If measurements are performed at low temperature, the PL and Raman spectroscopy will provide new dimensions to the investigation of these nanoparticle properties.
- Using a very simple technique for ternary alloy thin film preparation as discussed in the present thesis work, we have been able to observe gap mode vibration in ZnS_xSe_{1-x} alloy thin films with $x = 0.91$. It may also be possible to obtain both the gap and local phonon modes vibrations in CdS_xSe_{1-x} alloy films, if alloys with small fraction of Se and S are prepared.
- Electrical characterization is not performed in the present thesis work. By preparing proper electrical contact that would make ohmic contact with the nanostructured binary compounds and the ternary alloys, electrical characterization may be performed. This will be useful investigation for optoelectronic applications.
- Heterojunction devices can be made using both the synthesized nanostructures and ternary alloy thin films. These devices may be tested for various optoelectronic applications including photovoltaic cells, LEDs, etc.

LIST OF PUBLICATIONS

A. International Journals

1. *Effect of Se concentration on mixed phonon modes and Spin orbit splitting in thermally evaporated CdS_xSe_{1-x} ($0 \leq x \leq 1$) films using CdS-CdSe nano-composites*, **Lalhriatzuala** and Pratima Agarwal, Materials Chemistry and Physics **162** (2015) 813.

2. *Studies on spin orbit splitting and dual mode phonon vibrations in ZnS_xSe_{1-x} ternary alloys films with varying Se concentration*, **Lalhriatzuala** and Pratima Agarwal, Journal of Electronic Materials **44** (2015) 3341 (**Editor's choice open access article**).

3. *Thermal and structural studies of CdSe nanorods synthesized by solvothermal process*, **Lalhriatzuala** and Pratima Agarwal, Physica Status Solidi (a) **213** (2016) 1885.

4. *Growth and characterization of ZnSe nanocrystals synthesized using solvothermal process*, **Lalhriatzuala** and Pratima Agarwal (Under Preparation).

B. Published Conference Proceedings (International/ National)

1. *Effect of substrate temperature on the structural and optical properties of CdTe films prepared by thermal evaporation*, **Lalhriatzuala**, Ramakrishna Madaka, Pratima Agarwal Physics of Semiconductor Devices (Springer) 17th International Workshop on the Physics of Semiconductor Devices 2013 Part IV (2014) pp. 363 doi: 10.1007/978-3-319-03002-9_91.

2. *Structural, optical and electrical characterization of CdSe nanorods synthesized by solvothermal process*, **Lalhriatzuala**, Ramakrishna Madaka and Pratima Agarwal, Conference Paper in Energy (Hindawi) Volume 2013 (2013), article ID 257359 doi.org/10.1155/2013/257359.

3. *Preparation and characterization of ZnSe thin film for photovoltaic applications*, **Lalhriatzuala** and Pratima Agarwal, International Journal of Innovative Research & Development Vol 1. Issue 7 (Spl. Issue) pp. 104.

4. *Fabrication of two dimensional carbon nanostructures using hot wire chemical vapor deposition technique*, Mukesh Singh, Himanshu S. Jha, Asha Yadav, **Lalhriatzuala**, Dinesh Deva, Pratima Agarwal, Proc. SPIE 8549 (2012) Page No. 854926, doi: 10.1117/12.927273.

5. Nanocrystalline cubic silicon carbide thin films for the window layer of solar cells deposited by hot wire CVD Himanshu S. Jha, Mukesh Singh, Asha Yadav, **Lalhriatzuala**, Dinesh Deva, Pratima Agarwal Proc. SPIE 8549 (2012) Page No. 85493D, doi: 10.1117/12.927239.

C. Papers Presented in Conference (International/ National)

1. *Study on the growth process and transport properties of ZnSe nanocrystalline particles synthesized using solvothermal reaction,* **Lalhriatzuala** and Pratima Agarwal, Twenty-First International Symposium on Processing and Fabrication of Advanced Materials PFAM – 21, IIT Guwhati, 10 – 13 December, 2012, abstract book pp. 74.

2. *Preparation and characterization of ZnSe thin film for photovoltaic applications,* ***Lalhriatzuala*** *and Pratima Agarwal,* International Seminar and Workshop on Energy Sustainability and Development, Sibsagar College, 12 – 14 October, 2012.

3. *Structural and optical studies of ZnSe nanoparticles prepared using solvothermal process*, **Lalhriatzuala** and Pratima Agarwal, Abstract book pp. 63, Conference on Photochemistry and Luminescence – 2012, 9 – 10 March 2012, IIT Guwahati.

4. *Structural and transport studies of ZnS films prepared by doctor blade's technique*, **Lalhriatzuala**, Himanshu S. Jha, Mukesh Singh, Asha Yadav, Anjani K. Maurya and Pratima Agarwal, Abstract book pp. 93, Condeensed Matter Days 2011, Aug. 24 – 26, 2011, Guwahati University.

5. *Thermal stability and structural properties of CdSe nanorods synthesized by solvothermal process,* **Lalhriatzuala** and Pratima Agarwal, Abstract book pp. 194 ICANS26, 13 – 18 September, 2015, Aachen, Germany.

D. International/ National Conference Attended

1. Condensed Matter Days 2011, Aug. 24 – 26, 2011, Guwahati University.

2. International Seminar and Workshop on Energy Sustainability and Development, Sibsagar College, 12 – 14 October, 2012.

3. Conference on Photochemistry and Luminescence – 2012, 9 – 10th March 2012, IIT Guwahati.

4. Twenty-First International Symposium on Processing and Fabrication of Advanced Materials PFAM – 21, IIT Guwhati, 10 – 13 December, 2012.

5. 26th International Conference on Amorphous and Nanocrystalline Semiconductors (ICANS26), 13 – 18 September, 2015, Aachen, Germany.

Appendix I

DETAILS OF SOLVOTHERMAL SYNTHESIS OF BINARY SULFIDE COMPOUNDS AND SOME RESULTS

This appendix presents detail experimental steps in the synthesis of sulfide precursors used in the thermal evaporation technique employed in this thesis. It contains complete experimental steps consisting of chemical solution composition and some results on ZnS and CdS powders.

Solvothermal synthesis of ZnS powders

In this synthesis, zinc acetate [$(CH_3COO)_2$ Zn: $2H_2O$] and sodium sulfite (Na_2SO_3) were respectively used as cation and anion precursor salts. Zinc acetate (0.01 mol i.e., 2.1949 gm) was first dissolved in 10 mL of de-ionized water and then slowly mixed with 8 mL of ammonia solution (NH_3. H_2O) under constant stirring. Same molar amount of anion salt i.e., 0.01 mol of sodium sulfite (1.2604 gm) was also similarly mixed with 10 mL of hydrazine hydrate (N_2H_4. H_2O). The two solutions were poured in 110 mL capacity autoclave, which was then filled with de-ionized water up to 80% of its volume. After 10 minutes of stirring, the closed chamber was placed inside a muffle furnace at a preset temperature of 180 ^{o}C for 5 hrs. Once, the set time in the muffle furnace elapsed, the autoclave was allowed to slowly cool down to room temperature. The precipitates obtained in the autoclave was filtered off and washed several times in distilled water and ethanol. The final product was then dried at room temperature for several hours to get the powders. All chemicals used in the synthesis were purchased from Merck and were used without any further purification.

In this solvothermal reaction, the solvents such as ammonia and hydrazine hydrate are believed to perform the same function as described in the chemical reactions involved in the synthesis of CdSe and ZnSe [Chapter 2 Section 2.1.1.2 and 2.1.1.3].. Similar to hydrazine, the sulfur precursor used in this solvothermal reaction, i.e., Na_2SO_3 is also commonly used as oxygen scavenger and can react with oxygen even at mild temperatures and pressures [1]. In its reaction with oxygen, sodium sulfite produces sodium sulfate i.e., $2\ Na_2SO_3 + O_2 \rightarrow 2\ Na_2SO_4$. However, at pressure above 41 bars sulfite breaks down resulting in the formation of sulfur dioxide or hydrogen sulfide, by either of two routes [1, 2]:

$$Na_2SO_3 + H_2O \rightarrow SO_2 + 2\ NaOH$$

Appendix I

$$4Na_2SO_3 + 2\ H_2O \rightarrow H_2S + 2\ NaOH + 3\ Na_2SO_4$$

In the solvothermal reaction performed in this thesis work, the synthesis chemical reactions take place inside a sealed autoclave. The pressure inside the autoclave is autogenous and depends on the extent in which the autoclave is filled and the temperature. The pressure vs temperature dependence of water for different degrees of filling is shown in figure 1. Higher filling at higher temperature i.e., 80 % filling and at 245 ^{o}C leads to extremely high pressure that may damage the autoclave and may cause explosion [3]. Typical pressure reported in literature for the solvothermal synthesis of nanoquartz at 300 ^{o}C is between 78 - 90 bar [4]. Though the autoclave used in the synthesis does not have pressure gauge, with the amount of filling and the temperature it is likely possible that autogenous pressure inside the autoclave is sufficient to induce the sulfite break down in the presence of other solvents such as hydrazine hydrate and ammonia. Once the H_2S formation takes place, the following reactions may occur resulting in the release of S in the solution.

$$2H_2S + SO_2 \rightarrow 2H_2O + 3S$$

$$4\ Na_2SO_3 + 3\ H_2S \rightarrow 3\ H_2SO_4 + 4\ Na_2S$$

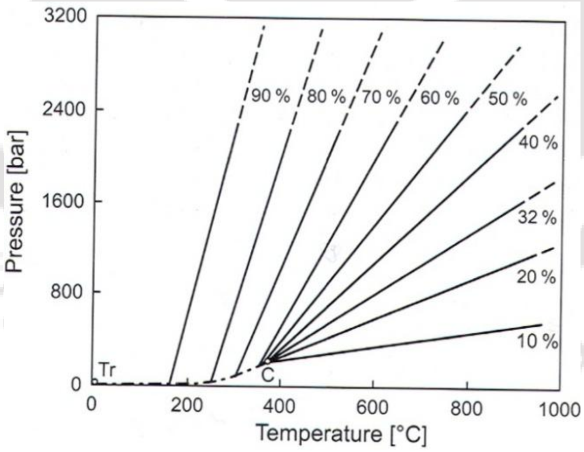

Fig. 1. Pressure inside autoclave as a function of percentage of fill with water and temperature [3, 5].

Solvothermal synthesis of CdS powders

In this synthesis, 0.01 mol (i.e., 2.6652 gm) of cadmium acetate [$(CH_3COO)_2$ Cd: $2H_2O$] was used as cation precursor salt. Sodium sulfite (0.01 mol i.e., 1.2604 gm) was again used as anion precursor salt. The experimental steps performed in the synthesis were same as ZnS nanocrystal synthesis. Here, cadmium and sulfur ions released in the reaction solution results in the formation of CdS nanocrystals.

Figure 2 (a) – (c) show the reaction chamber (autoclave) used in this thesis work and the extracted ZnS and CdS powders. About 0.6 gm of ZnS was obtained as white precipitate. CdS synthesis reaction resulted in higher yield than ZnS synthesis reaction. Yellow CdS powder of about 1.1 gm was collected.

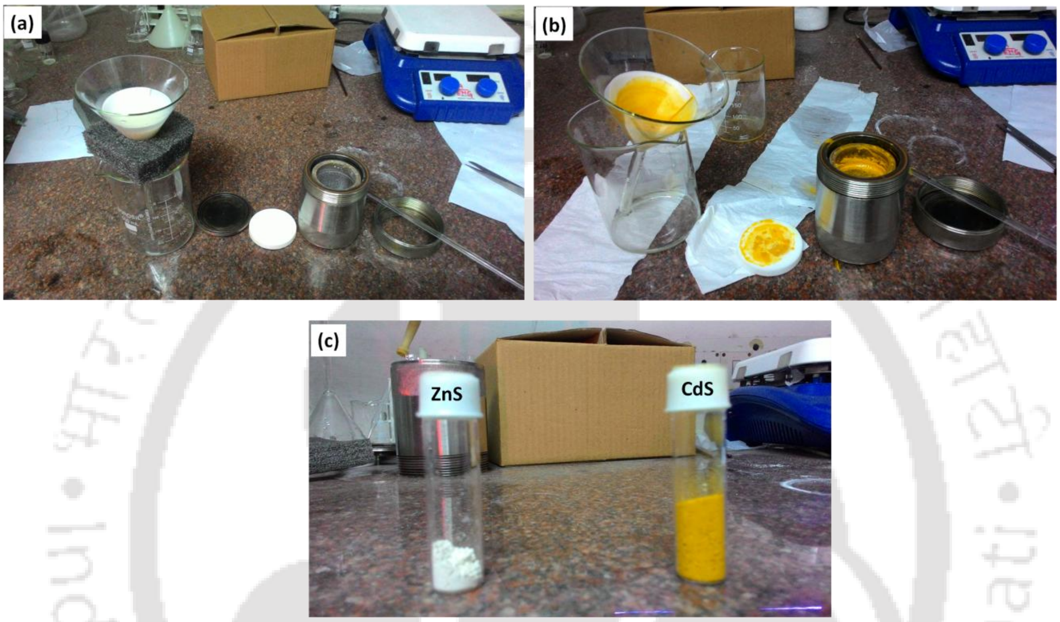

Fig. 2. (a) ZnS and (b) CdS powders being extracted from autoclave, (c) ZnS and CdS powders as synthesized using the solvothermal process.

XRD studies on CdS and ZnS powders

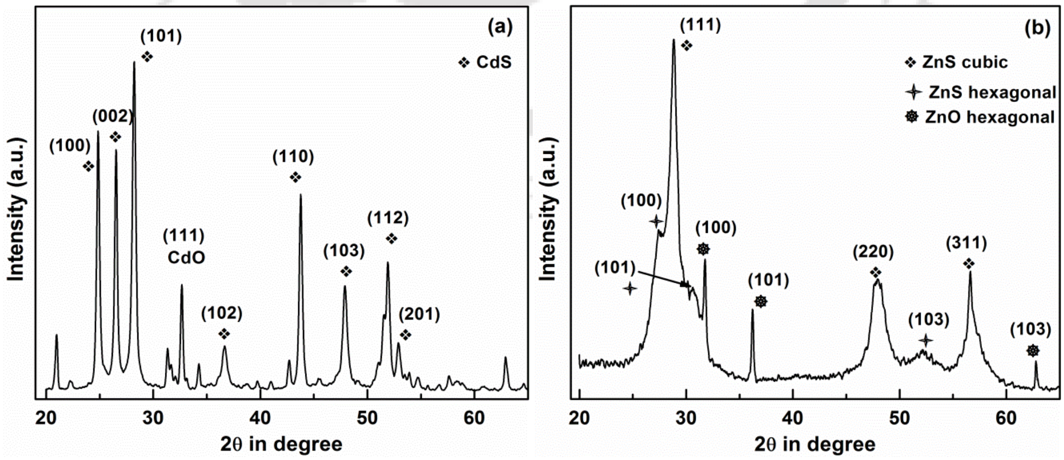

Fig. 3. XRD pattern of (a) ZnS and (b) CdS powders.

XRD measurement was performed on the synthesized CdS and ZnS powders using Rigaku TTRAX – III diffractometer with CuK$_{\alpha}$ (λ = 1.5406 Å) radiation in 2θ range of 20 – 65°. Figure 3. (a) and (b) show the XRD patterns of CdS and ZnS powders respectively. The peaks are identified by comparing with standard JCPDS data as given in table 1 and 2. The observed peaks in CdS powders correspond to wurtzite CdS. The three main peaks in XRD pattern of ZnS correspond to cubic ZnS. In both these compounds, the observed 2θ values closely match with the standard data. In addition to the peaks identified as wurtzite planes of CdS, weak impurity peaks some of which correspond to CdO are also observed in CdS sample. In ZnS powder XRD, smaller peaks are also similarly observed. These are also identified in the figure by comparing with standard JCPDS data for wurtzite phase of ZnS (PDF # 751534) and ZnO (PDF # 800075). The observed XRD peaks corresponding to CdS and ZnS crystal planes are an indication that the synthesis routes used in this work result in the formation of CdS and ZnS compounds.

Table 1. 2θ values and relative intensities of observed peaks in CdS nanocrystals.

(*hkl*) plane	Observed 2θ value	Standard JCPDS 2θ value (#772306)	Relative Intensities I_{101}/I_{hkl}	
			Observed	Standard (#772306)
100	24.87	24.84	1.39	1.57
002	26.52	26.53	1.58	2.21
101	28.23	28.22	1	1
102	36.69	36.66	6.89	3.95
110	43.80	43.74	1.78	2.35
103	47.88	47.89	3.15	2.46
112	51.90	51.89	2.53	3.25
201	52.96	52.87	6.38	7.51

Table 2. 2θ values and relative intensities of observed peaks in ZnS nanocrystals.

(*hkl*) Plane	Observed 2θ value	Standard JCPDS 2θ value (#800020)	Relative Intensities I_{111}/I_{hkl}	
			Observed	Standard (#800020)
111	28.83	28.91	1	1
220	47.99	48.11	2.85	2.01
311	56.67	57.10	2.83	3.47

Raman studies on CdS and ZnS powders

Raman scattering was performed on the synthesized CdS and ZnS powders using Horiba JY LabRam HR800 micro - Raman system in back scattering geometry. Monochromatic argon laser excitation source with 488 nm was used. Figure 4 (a) and (b) show the Raman spectra of CdS and ZnS powders respectively. The CdS Raman spectra show only one distinct phonon mode at around 304 cm^{-1}, which is the LO phonon mode vibration of the CdS wurtzite crystal as reported in literature [6, 7]. In the ZnS Raman spectra, the most prominent peak observed at around 350 cm^{-1} corresponds to the LO phonon mode vibration of ZnS zincblende crystal [8 - 10]. In addition to this phonon mode, there are weaker phonon modes corresponding to TO of ZnO [11, 12] and other residual impurities. The observed phonon modes in the Raman spectra of these two compounds support the XRD findings. These spectra show that the sulfide compounds are indeed formed in the solvothermal reaction used in this thesis work.

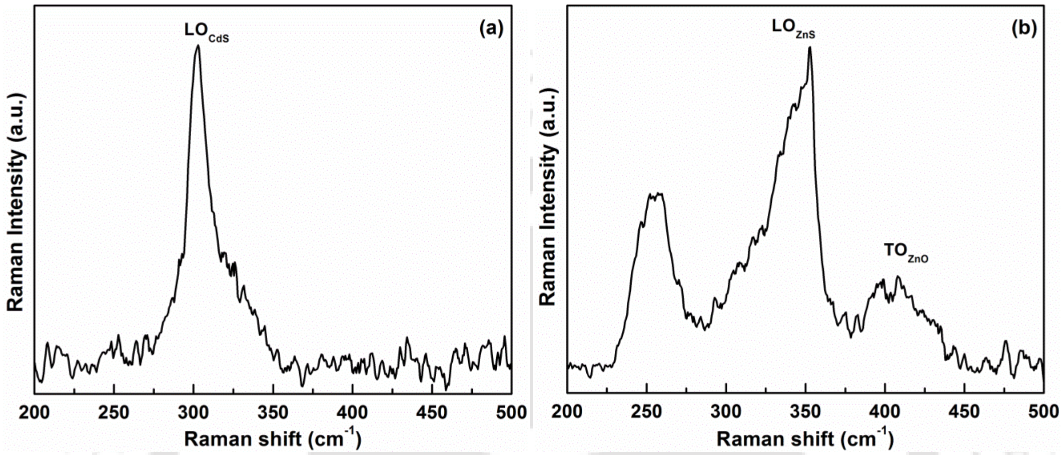

Fig. 4. Raman spectra of (a) CdS and (b) ZnS powders.

EDX studies on CdS and ZnS powders

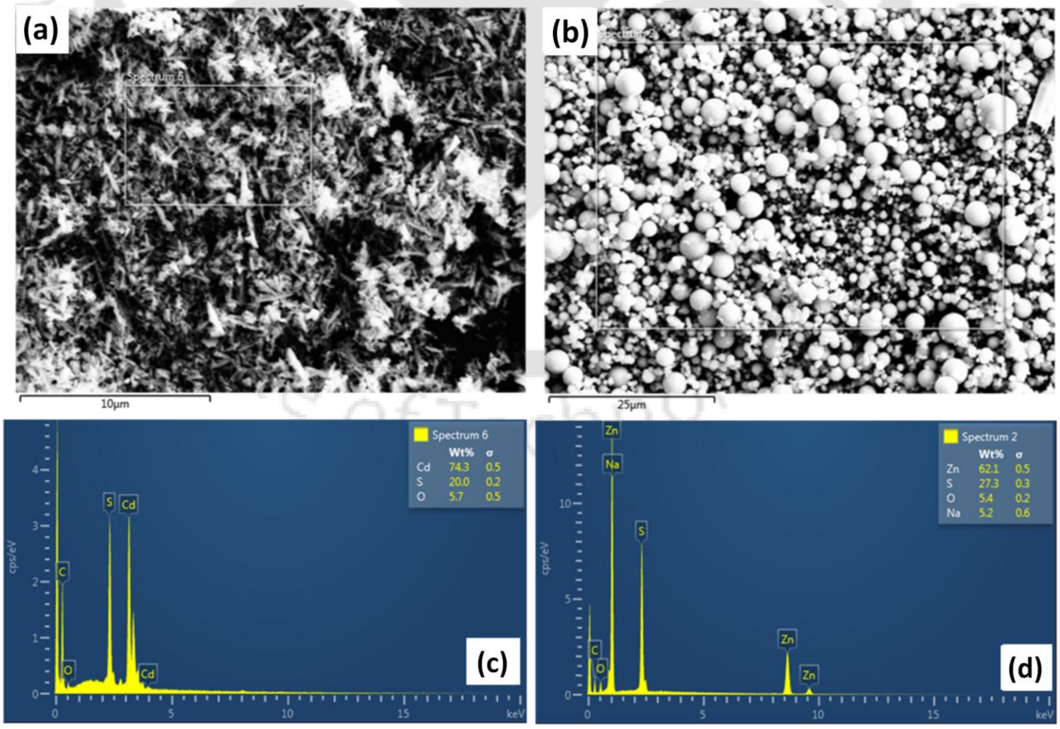

Fig. 5. FESEM images of the synthesized (a) CdS and (b) ZnS powders showing the area where EDX spectra are recorded. EDX spectra of (c) CdS and (d) ZnS powders.

Appendix I

EDX spectra on the synthesized CdS and ZnS powders were performed using Field emission scanning electron microscope, ΣIGMA ZEISS with an EDX spectrometer. Figure 5 (a) – (d) show the EDX spectra and the corresponding FESEM images where the analysis were performed. The images show that while the CdS particles possess elongated rod shaped morphology, the ZnS particles are mostly spherical in shape. The EDX spectra in both the cases show the presence of oxygen and carbon in addition to the respective elements in the compounds. The oxygen signature in the spectra is likely due to small amount of oxides formation in the synthesis. The presence of carbon is due to the carbon tape used in the analysis. The presence of sodium in small fraction of weight percent in ZnS powder sample is likely due to the residual impurities that can be removed with thorough washing of the extracted precipitates.

These measurements show that the sulfide compounds can be formed by the solvothermal chemical route as conducted in this thesis work. Even though the findings indicate the formation of residual and oxide impurities, further optimization may lead to improvement in terms of chemical purity and crystallinity. However, since these compounds are just used as precursor for thin film preparation using thermal evaporation technique, optimization study is not performed.

References

1. http://www.subsport.eu/wp-content/uploads/2012/05/alternative-to-hydrtazine-USA-2001-k.pdf
2. Buecker B., Fundamentals of Steam Generation Chemistry (PennWell Corp, Oklahoma, 2000), pp. 187.
3. http://www.uio.no/studier/emner/matnat/kjemi/KJM5100/h06/undervisningsmateriale/15KJM5100_2006_solvothermal_b.pdf
4. Sochalski-Kolbus, L. M., et al., Solvothermal Synthesis and Surface Chemistry To Control the Size and Morphology of Nanoquartz, Crystal Growth and Design, **15** (2015) 5327 – 5331.
5. G.C. Kennedy, Amer. J. Sci., **248** (1950) 540.
6. C.A. Arguello, D. L. Rousseau and S.P.S. Porto, Phys. Rev., **181**(1969) 1351.
7. B. Tell, T.C. Damen and S.P.S. Porto, Phys. Rev., **144** (1966) 771.

8. Numerical Data and Functional Relationships in Science and Technology, edited by O. Madelung, M. Schulz, and H. Weiss, Landolt – Bornstein, New Series, Group III, Vol. 17, Pt. (Springer, Berlin, 1982).
9. A. Memon and D. B. Tanner, Phys. Status Solidi (b), **127** (1985) 49.
10. M. Siakavellas, A. G. Kontos, and E. Anastassakis, J. Appl. Phys., **84** (1998) 517.
11. E.C. Heltemes and H. L. Swinney, J. Appl. Phys., **38** (1967) 2387.
12. B. H. Bairamov, A. Heinrich, G. Irmer, V. V. Toporov, and E. Ziegler, Phys. Status Solidi (b), **119** (1983) 227.

Appendix - II

SOLUTION COMPOSITION FOR THE SYNTHESIS OF CdSSe AND ZnSSe COMPOSITE POWDERS

Table 1: Solution composition for the synthesis of the CdSSe composite powders discussed in chapter 4 sections 4.1.1.

Composite powder composition in at. % Cd:S:Se	**Precursor molar ratio** Cadmium acetate: sodium sulfite: sodium selenite	**Solvent**
51.98: 0 : 48.02 (CdSe)	0.005: 0 :0.005	Ammonia – 8 mL, Hydrazine hydrate – 10 mL and deionized water to fill the autoclave up to 80% of its volume
55.05:15.38:29.55	0.01:0.005:0.005	Ammonia – 8 mL, Hydrazine hydrate – 10 mL and deionized water to fill the autoclave up to 80% of its volume
56.84:16.30:26.85	0.01: 0.006: 0.004	Ammonia – 8 mL, Hydrazine hydrate – 10 mL and deionized water to fill the autoclave up to 80% of its volume
56.65:31.34:12.01	0.01: 0.008: 0.002	Ammonia – 8 mL, Hydrazine hydrate – 10 mL and deionized water to fill the autoclave up to 80% of its volume
40.28: 38.01: 0 (CdS)	0.01: 0.01: 0	Ammonia – 8 mL, Hydrazine hydrate – 10 mL and deionized water to fill the autoclave up to 80% of its volume

Table 2: Solution composition for the synthesis of the ZnSSe composite powders discussed in chapter 5 sections 5.1.1.

Composite powder composition in at. % Zn:S:Se	**Precursor molar ratio** Zinc acetate: sodium sulfite: sodium selenite	**Solvent**
49.09: 0: 50.91 (ZnSe)	0.005: 0 : 0.005	Ammonia – 8 mL, Hydrazine hydrate – 10 mL and deionized water to fill the autoclave up to 80% of its volume
42.56:24.40:15.88	0.01: 0.007: 0.003	Ammonia – 8 mL, Hydrazine hydrate – 10 mL and deionized water to fill the autoclave up to 80% of its volume
53.00:41.28:5.72	0.01: 0.008: 0.002	Ammonia – 8 mL, Hydrazine hydrate – 10 mL and deionized water to fill the autoclave up to 80% of its volume
53.45:46.32:0.23	0.01: 0.0095: 0.0005	Ammonia – 8 mL, Hydrazine hydrate – 10 mL and deionized water to fill the autoclave up to 80% of its volume
56.24: 43.76: 0 (ZnS)	0.01: 0.01: 0	Ammonia – 8 mL, Hydrazine hydrate – 10 mL and deionized water to fill the autoclave up to 80% of its volume